

PARALLEL NAVIER STOKES SOLUTIONS OF
LOW ASPECT RATIO RECTANGULAR FLAT WINGS
IN COMPRESSIBLE FLOW

A DISSERTATION SUBMITTED TO
THE GRADUATE SCHOOL OF NATURAL AND APPLIED SCIENCES
OF
MIDDLE EAST TECHNICAL UNIVERSITY

BY

GÖKHAN DURMUŞ

IN PARTIAL FULFILLMENT OF THE REQUIREMENTS
FOR
THE DOCTOR OF PHILOSOPHY
IN
AEROSPACE ENGINEERING

SEPTEMBER 2004

Approval of the Graduate School Natural and Applied Sciences

Prof. Dr. Canan Özgen
Director

I certify that this thesis satisfies all the requirements as a thesis for the degree of Doctor of Philosophy.

Prof. Dr. Nafiz Alemdaroğlu
Head of department

This is to certify that we have read this thesis and that in our opinion it is fully adequate, in scope and quality, as a thesis for the degree of Doctor of Philosophy.

Prof. Dr. Mehmet Ş. Kavsaoglu
Co-Supervisor

Assoc.Prof. Dr. Sinan Eyi
Supervisor

Examining Committee Members (first name belongs to the chairperson of the jury and the second name belongs to supervisor)

Prof. Dr. Sinan Akmandor (METU, AE)_____

Assoc.Prof. Dr. Sinan Eyi (METU, AE)_____

Prof. Dr. Mehmet Ş. Kavsaoglu (ITU, AE)_____

Prof. Dr. Ünver Kaynak (ETU, ME)_____

Assoc. Prof. Dr.Yusuf Özyörük (METU, AE)_____

I hereby declare that all information in this document has been obtained and presented in accordance with academic rules and ethical conduct. I also declare that, as required by these rules and conduct, I have fully cited and referenced all material and results that are not original to this work.

Name, Last name : Gökhan Durmus

Signature :

ABSTRACT

PARALLEL NAVIER STOKES SOLUTIONS OF LOW ASPECT RATIO RECTANGULAR FLAT WINGS IN COMPRESSIBLE FLOW

Durmuş, Gökhan

Ph.D., Department of Aerospace Engineering

Supervisor : Assoc Prof. Dr. Sinan Eyi

Co-Supervisor: Prof. Dr. Mehmet Ş. Kavsaoğlu

September 2004, 132 pages

The objective of this thesis is to accomplish the three dimensional parallel thin-layer Navier-Stokes solutions for low aspect ratio rectangular flat wings in compressible flow. Two block parallel Navier Stokes solutions of an aspect ratio 1.0 flat plate with sharp edges are obtained at different Mach numbers and angles of attack. Reynolds numbers are of the order of $1.0E5$ - $3.0E5$. Two different grid configurations, the coarse and the fine grids, are applied in order to speed up convergence. In coarse grid configuration, 92820 total grid points are used in two blocks, whereas it is 700,000 in fine grid. The flow field is dominated by the vortices and the separated flows. Baldwin Lomax turbulence model is used over the flat plate surface. For the regions dominated by the strong side edge vortices, turbulence model is modified using a polar coordinate system whose origin is at the minimum pressure

point of the vortex. In addition, an algebraic wake-type turbulence model is used for the wake region behind the wing. The initial flow variables at the fine grid points are obtained by the interpolation based on the coarse grid results previously obtained for 40000 iterations. Iterations are continued with the fine grid about 20000-40000 more steps. Pressures of the top surface are predicted well with the exception of leading edge region, which may be due to unsuitable turbulence model and/or grid quality. The predictions of the side edge vortices and the size of the leading edge bubble are in good agreement with the experiment.

Keywords: Computational Fluid Dynamics, Navier-Stokes, Multi-Block, Vortical Flows, Flow Separation

ÖZ

KISA AÇIKLIK ORANLI, DÜZ, DİKDÖRTGEN KANATLARIN SIKIŞTIRILABİLİR AKIM ALANLARININ PARALEL NAVIER STOKES ÇÖZÜMLERİ

Durmuş, Gökhan

Doktora, Havacılık ve Uzay Mühendisliği Bölümü

Tez Yöneticisi : Doç. Dr. Sinan Eyi

Ortak Tez Yöneticisi: Prof. Dr. Mehmet Ş. Kavsaoğlu

Eylül 2004, 132 sayfa

Bu tezde kısa açıklık oranlı, düz, dikdörtgen kanatların sıkıştırılabilir akımlarda üç boyutlu paralel ince-tabaka Navier Stokes çözümleri gerçekleştirildi. Keskin kenarlı açıklık oranı 1.0 olan düz levha için iki bloklu paralel Navier Stokes çözümleri, değişik Mach sayılarında ve hücum açılarında elde edildi. Reynolds sayıları $1.0E5$ ila $3.0E5$ mertebesinde. Çözümü hızlandırmak için önce seyrek daha sonra da sık olmak üzere iki farklı ağ kullanılmıştır. Seyrek ağda her iki blokta toplam 92820 adet nokta kullanılmakta olup bu sayı sık ağda 700,000'e çıkarılmıştır. Akım alanında, girdap ve ayrılmış akımlar etkin bir şekilde yer almaktadır. Levha yüzeyi üzerinde Baldwin-Lomax türbülans modeli kullanılmıştır. Ancak, güçlü kanat ucu girdaplarının baskın olduğu bölgelerde, Baldwin-Lomax türbülans modelinin, merkezi girdabın en

düşük basınç noktası olarak belirlenen bir polar koordinat sistemi kullanılarak yeniden düzenlenmiş hali kullanılmıştır. Ayrıca, kanat arkası iz bölgelerinde cebirsel iz tipi türbülans modeli kullanılmıştır. Sık ağ çözümü için gerekli olan akım verileri seyrek ağ çözümün interpolasyonu ile edilmiştir. Sonuçların, özellikle üst yüzey basınç değerlerinin ve güçlü kanat ucu girdaplarının genelde deneyle uyum içinde olduğu görülmüştür. En belirgin uyumsuzluklar üst yüzeyde hücum kenarı civarındadır. Bunun nedeni ağ kalitesi ve/veya türbülans modelinin yetersizliği olabilir.

Anahtar Kelimeler: Sayısal Akışkanlar Dinamiği, Navier-Stokes, Çok Bloklü Çözüm. Girdap Akımları, Akım ayrılması

ACKNOWLEDGMENTS

The author wishes to express his deepest gratitude to his supervisor Prof. Dr. Mehmet Şerif Kavsaoglu for their guidance, advice, criticism, encouragements and insight throughout the research. After he moved to İstanbul Technical University, he was attendant as co-supervisor and left his supervisory job to Assoc. Prof .Dr. Sinan Eyi for the last six-month period.

The author thanks Assoc. Prof. Dr. Sinan Eyi and Prof. Dr. Ünver .Kaynak for their valuable comments and assistance over the past three years. This thesis took its shape with their enormous expertise and kind support.

The author also thanks his gratefulness to his parents and friends for their encouragement and support during this thesis study.

TABLE OF CONTENTS

PLAGIARISM	iii
ABSTRACT	iv
ÖZ	vi
ACKNOWLEDGMENTS	viii
TABLE OF CONTENTS	ix
LIST OF TABLES	xii
LIST OF FIGURES	xiii
LIST OF SYMBOLS AND ABBREVIATIONS	xix
CHAPTER	
1.INTRODUCTION	1
1.1. Motivation	1
1.2. General Features of the Separated Flows	3
1.3. General Description of the Flowfield around the Low Aspect Ratio Wings	11
1.4. Literature Review on Low Aspect Ratio Wings	16
1.5. Outline of Dissertation	19
2.NAVIER STOKES EQUATIONS	20
3.SOLUTION ALGORITHM	28
4.HYPERBOLIC GRID GENERATION WITH UPWIND DIFFERENCING	32
4.1. Governing Equations	32
4.2. Cell volume specification	38
4.3. Boundary Conditions	39
4.4. An Example	39

5.ADAPTED TURBULENCE MODELS	41
5.1. Baldwin-Lomax Turbulence Model	41
5.2. Degani-Schiff Modification	43
5.3. Vorticity Adaptation	43
5.4. Algebraic Model for Vortical Flows	44
5.5. Algebraic Wake Model	45
6.TEST CASES AND RESULTS	47
6.1. Two Dimensional Test Cases.....	47
6.1.1. Laminar Flat Plate	47
6.1.1.1. Computational Grid and Initial Conditions	48
6.1.1.2. Boundary Conditions.....	51
6.1.1.3. Computational Studies.....	52
6.1.1.4. Convergence History	52
6.1.1.5. Comparisons of the results.....	54
6.1.2. Turbulent Flat Plate.....	64
6.1.2.1. Computational Grid and Initial Conditions	64
6.1.2.2. Boundary Conditions.....	67
6.1.2.3. Computational History.....	67
6.1.2.4. Convergence History	68
6.1.2.5. Computed Results	68
6.2. Three Dimensional Flat Plate	74
6.2.1. Problem Description	74
6.2.2. Experimental Data For Comparison.....	77
6.2.3. Computational Grid.....	78
6.2.4. Boundary Conditions	81
6.2.5. Solution Procedure.....	83
6.2.6. Computational Details.....	84
6.2.7. Results and Comparison.....	85
6.2.7.1. Convergence Histories.....	85

6.2.7.2. Comparison with the Experiment	94
6.2.7.3. Computational Flow Field Visualizations.....	113
7.CONCLUSION	119
REFERENCES	121
VITA.....	131

LIST OF TABLES

Table 6.1 The grids used in the Computations.....	49
Table 6.2 Computational details	51
Table 6.3 Blasius solution	53
Table 6.4. Boundary conditions.....	67
Table 6.5 Computational details	67
Table 6.6 Computational test matrix.....	74
Table 6.7 The grids used in the computations.....	79
Table 6.8. Boundary conditions.....	82
Table 6.9 Iteration summary.....	84
Table 6.10 Computational details	85
Table 6.11 Solution summary	90

LIST OF FIGURES

Figure 1.1 Angle of attack flow regimes	2
Figure 1.2 Separation types	4
Figure 1.3 Separation bubble formation	5
Figure 1.4 Schematic of feedback loops of locked vortex shedding for blunt leading-edge plates with either blunt or streamlined trailing edges	7
Figure 1.5 Limiting streamline pattern and surfaces of separation for three types of 3-D separation.....	9
Figure 1.6. Singular points	9
Figure 1.7. Line of separation.....	11
Figure 1.8 The lifting characteristics of wings with low aspect ratios	12
Figure 1.9 Oil-flow pattern on slender, rectangular wing, aspect ratio 0.25 at $\alpha = 20^\circ$	13
Figure 1.10 Interpretation of skin-friction lines and pressures on slender, rectangular wing, aspect ratio 0.25 at $\alpha = 20^\circ$	13
Figure 1.11 Illustrative 3-d flowfield around the low-aspect ratio flat wings.....	14
Figure 1.12 Illustrative flowfield at the symmetry plane.....	15
Figure 1.13 Illustrative flowfield at the spanwise plane.....	15
Figure 4.1 Illustrative example of grid around Lann Wing	40
Figure 4.2 Zoomed view	40
Figure 5.1 Illustrative example of side wind vortex with pressure contours.....	44

Figure 6.1 The applied grid geometries.....	48
Figure 6.2 The grid configuration A	49
Figure 6.3. Grid configuration B.....	50
Figure 6.4. Grid configuration C.....	51
Figure 6.5 Convergence history, L_2 Norm of Residue.....	53
Figure 6.6 The boundary layer for grid A.....	55
Figure 6.7 Boundary layer for grid B	55
Figure 6.8 Boundary layer for grid C	56
Figure 6.9 Iterative convergence of the grid-A solution	57
Figure 6.10 Iterative convergence of the grid-B solution	57
Figure 6.11 Iterative convergence of the grid-C solution	58
Figure 6.12 Pressure coefficient comparison.....	58
Figure 6.13 Skin friction coefficient comparison.....	59
Figure 6.14 Boundary layer thickness comparison.....	61
Figure 6.15 Displacement thickness comparison.....	61
Figure 6.16 Momentum thickness comparison	62
Figure 6.17 Shape parameter comparison	62
Figure 6.18. Grid geometry	66
Figure 6.19. Grid geometry in actual dimensions.....	66
Figure 6.20. Zoomed view of the grid about $x/c=0.0$	66
Figure 6.21. Convergence history	68
Figure 6.22. Velocity profile at $x/c = 0.1$	69
Figure 6.23. Velocity profile at $x/c = 1.0$	69
Figure 6.24. Velocity profile at $x/c = 2.0$	70
Figure 6.25. Boundary layer thickness.....	71
Figure 6.27. Momentum thickness	71
Figure 6.26. Displacement thickness.....	72
Figure 6.28. Shape factor	72
Figure 6.29. Skin friction coefficient.....	73
Figure 6.30 Computational flow domain.....	75

Figure 6.31 Computational flat plate geometry.....	76
Figure 6.32 Model used for compressible oil flow tests [10].	76
Figure 6.33 Overall view of the grid blocks, Block-1 and Block-2.....	78
Figure 6.34 Symmetry plane ($y/c=0$) view of the grid around the flat plate.	80
Figure 6.35 Zoomed view of Symmetry plane ($y/c=0$) of the fine grid around the flat plate.	80
Figure 6.36 Top view of the grid at $z/c=0.0$ plane.	81
Figure 6.37 Boundary conditions.....	82
Figure 6.38 Convergence histories for the coarse and fine grid for each Case.....	86
Figure 6.39 Convergence histories for only the fine grid for each Case	87
Figure 6.40 Convergence histories in terms of Normal Force	88
Figure 6.41 Convergence histories in terms of Pitching Moment	89
Figure 6.42 Dimensional frequency variation with the angle of attack.....	92
Figure 6.43 Non-dimensional frequency variation with the angle of attack.....	92
Figure 6.44 Variation of the force-moment coefficients over one periodic cycle	93
Figure 6.45 The computed time-mean averaged and experimentally obtained surface pressures in comparison. Mach=0.54, $\alpha=7.5^\circ$. 95	
Figure 6.46 The computed time-mean averaged and experimentally obtained surface pressures in comparison. Mach=0.55, $\alpha=13.5^\circ$	95
Figure 6.47 The computed time-mean averaged and experimentally obtained surface pressures in comparison. Mach=0.87, $\alpha=7.5^\circ$. 96	

Figure 6.48 The computed time-mean averaged and experimentally obtained surface pressures in comparison. Mach=0.85, $\alpha=13.5^\circ$	96
Figure 6.49 Comparison of computational and experimental [36] surface pressures along y strips. Case: P1 Mach=0.54, $\alpha=7.5^\circ$..	97
Figure 6.50 Comparison of computational and experimental [36] surface pressures along x strips. Case: P1 Mach=0.54, $\alpha=7.5^\circ$..	98
Figure 6.51 Comparison of computational and experimental [36]surface pressures along y strips. Case: P2 Mach=0.55, $\alpha=13.5^\circ$	99
Figure 6.52 Comparison of computational and experimental [36] surface pressures along x strips. Case: P2 Mach=0.55, $\alpha=13.5^\circ$	100
Figure 6.53 Comparison of computational and experimental [36] surface pressures along y strips. Case: P3 Mach=0.87, $\alpha=7.5^\circ$	101
Figure 6.54 Comparison of computational and experimental [36] surface pressures along x strips. Case: P3 Mach=0.87, $\alpha=7.5^\circ$	102
Figure 6.55 Comparison of computational and experimental [36] surface pressures along y strips. Case: P4 Mach=0.85, $\alpha=13.5^\circ$	103
Figure 6.56 Comparison of computational and experimental [36] surface pressures along x strips. Case: P4 Mach=0.85, $\alpha=13.5^\circ$	104
Figure 6.57 Experimentally obtained top surface streamlines $\alpha=5^\circ$, Mach ≈ 0.1 , Re=2.0*10 ⁵ [39]. The flow is from bottom to top....	106
Figure 6.58 Experimentally obtained top surface streamlines $\alpha=15^\circ$, Mach ≈ 0.1 , Re=2.0*10 ⁵ [39]. The flow is from bottom to top....	106
Figure 6.59 Computationally obtained top surface streamlines (time-mean averaged). Case: S1 $\alpha=5^\circ$, Mach = 0.42.....	107

Figure 6.60 Computationally obtained top surface streamlines (time-mean averaged). Case: S2 $\alpha=15^\circ$, Mach = 0.42.....	107
Figure 6.61 Comparison of computational (time-mean averaged) and experimental [39] top surface streamlines. Case S1 $\alpha=5^\circ$, Mach = 0.42.....	108
Figure 6.62 Comparison of computational (time-mean averaged) and experimental [39] top surface streamlines. Case S2 $\alpha=15^\circ$, Mach = 0.42.....	108
Figure 6.63 Definition of topology of the surface streamlines pattern (time-mean averaged), Case S1 $\alpha=5^\circ$, Mach = 0.42.....	109
Figure 6.64 Definitions of topology of the surface streamlines pattern (time-mean averaged), Case S2 $\alpha=15^\circ$, Mach = 0.42. .	109
Figure 6.65 Comparison of computational and experimental [39] pitching-moment coefficients, Mach = 0.42, Re = $2.0 \cdot 10^5$. Computational data from Case's: S1 and S2.	110
Figure 6.66 Comparison of computational and experimental [39] pitching-moment coefficients, Mach = 0.54-0.55, Re = $2.0 \cdot 10^5$. Computational data from Case's: P1 and P2.....	111
Figure 6.67 Comparison of computational and experimental [39] pitching-moment coefficients, Mach = 0.85-0.87, Re = $2.0 \cdot 10^5$. Computational data from Case's: P3 and P4.	111
Figure 6.68 Comparison of computational and experimental [39] normal force coefficients, Mach = 0.42, Re = $2.0 \cdot 10^5$. Computational data from Case's: S1 and S2.	112
Figure 6.69 Comparison of computational and experimental [39] normal force coefficients, Mach = 0.54-0.55, Re = $2.0 \cdot 10^5$. Computational data from Case's: P1 and P2.....	112
Figure 6.70 Comparison of computational and experimental [39] normal force coefficients, Mach = 0.85-0.87, Re = $2.0 \cdot 10^5$. Computational data from Case's: P3 and P4.....	113

Figure 6.71 Flow timeline of Case S2 $\alpha=15^\circ$, Mach = 0.42.....	116
Figure 6.72 Three-dimensional flow structure of Case S2; $\alpha=15^\circ$, Mach = 0.42.....	117
Figure 6.73 Primary and secondary vortices at the span wise plane, x/c=0.5.	118
Figure 6.74 Primary and secondary bubbles at the symmetry plane, y/c=0.0	118

LIST OF SYMBOLS AND ABBREVIATIONS

Roman Symbols

A, B, C	coefficient matrices
\bar{a}	time averaged variable a
\hat{c}	transformed flux c
c_f	the skin friction coefficient
C_N	normal force coefficient
C_M	pitching moment coefficient
d	solution vector
dt	code time step for one iteration
dt	dimensional time step for one iteration (s)
$Det()$	determinant of a matrix
e	total energy per unit volume
e, f, g	right hand side vector
E, F, G	inviscid fluxes
E_v, F_v, G_v	viscous fluxes
f	non-dimensional frequency
f	dimensional frequency (1/s)
H	shape factor
J	Jacobian
$JMAX$	maximum grid indices in ξ direction
I	identity matrix
i, j, k	grid indices related to ξ , η and ζ directions respectively
$KMAX$	maximum grid indices in η direction
k_T	turbulent conductivity

$LMAX$	maximum grid indices in ζ direction
M_{∞}	freestream Mach number
p	pressure
Pr	Prandtl number
q	dependent variables vector
q_x, q_y, q_z	heat conduction terms
r	position vector
R	Universal Gas Constant
Re	Reynolds number
Re_x	Reynolds number based on distance
s_1	initial grid spacing
T	non-dimensional period
T	dimensional period (s)
u, v, w	fluid velocities in the x, y and z coordinate directions
U, V, W	contravariant velocity components
u_{\max}	the value at the first maximum in the u profile
\vec{v}	vector v
V	cell volume or inverse Jacobian
w	denotes the "wall" quantities
x, y, z	cartesian coordinates of physical plane
$x/c, y/c, z/c$	coordinates non-dimensionalized by the chord length
y_m	the distance from the plate to the first maximum in u

Greek Symbols

α	angle of attack
α_{sv}	the angle of attack where symmetric vortices are formed
α_{AV}	the angle of attack where asymmetric vortices are formed
α_{UV}	the angle of attack where an unsteady vortex wake is formed

γ	ratio of specific heats
δ	boundary layer thickness
δ^*	displacement thickness
Δx_j	the normal distance to the location of μ'_t
Δx_{\max}	the length of the block in streamwise direction
Δz	distance increment in z direction
Δ, δ, ∇	forward, central and backward operators respectively
$\Delta \nabla$	laplacian operator
Δc	chord length
Δs	marching distance
ΔA	grid point surface area
ε	ratio of successive spacing
$\varepsilon_{i\xi}, \varepsilon_{i\eta}$	implicit smoothing parameters
$\varepsilon_i, \varepsilon_e$	implicit and explicit smoothing factors
θ	momentum thickness,
λ, β	eigenvalues
μ_t	the eddy viscosity
μ_{t_v}	the maximum eddy-viscosity
μ_{t_j}	the eddy-viscosity at the same j-station as μ'_t
μ'_t	eddy-viscosity in that wake region
ξ, η, ζ	computational domain coordinates
ρ	fluid density
τ_{xx}, \dots	the shear stresses
$\vec{\omega}$	vorticity vector
$\vec{\omega}_R$	reduced vorticity vector
$ \omega_v $	the local vorticity

Abbreviations

ADI	Alternating Direction Implicit
CFD	Computational Fluid Dynamics
CFL	Courant-Friedrich-Lewy Number
CPU	Central Processing Unit
LU	Lower-Upper Diagonal
MPI	Message Passing Interface
MB	Megabytes
N-S	Navier-Stokes
N, S	abbreviations for node and saddle points respectively
RAM	Random Access Memory

CHAPTER 1

INTRODUCTION

1.1. Motivation

Aircrafts or missiles fly and maneuver at a variety of incidence angles, depending on their purpose and flight requirements. When attempting to model the flowfield around, special difficulties are met depending on the flow regimes. A fairly good representation of the flow regimes is shown in Figure 1.1 where α_{sv} is the angle of attack where symmetric vortices are formed, α_{av} is the angle of attack where asymmetric vortices are formed, and α_{uv} is the angle of attack where an unsteady vortex wake is formed [1-5].

Various interesting features of the flow have been distinguished by the researchers in high angle of attack aerodynamics [2,3] including;

- Vortex asymmetry begins when the angle of attack, α_{av} is about twice the nose angle;
- Separation is very sensitive to nose geometric asymmetries;
- Increased nose sharpness increases asymmetry; and
- The results are difficult to reproduce experimentally [1].

For a geometry with sharp edges such as a flat delta wing with sharp edges or a flat rectangular wing with sharp edges, the line of separation is fixed at the sharp edge and the flow-field asymmetries are much less.

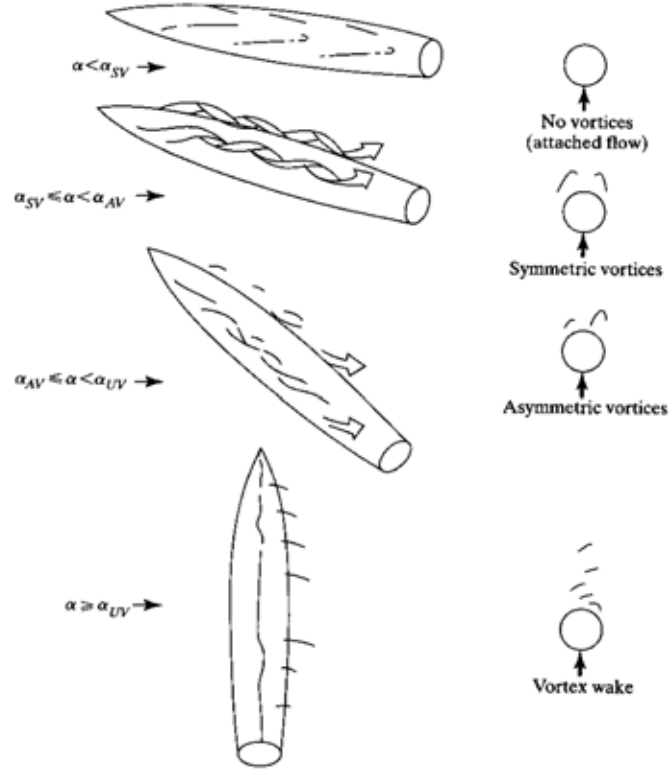


Figure 1.1 Angle of attack flow regimes [1-5].

Separated and complex turbulent flows have extensively been studied by experiments and numerical simulations to yield distributions of statistical flow properties such as time-mean velocities, pressure, Reynolds stresses, correlations, and spatio-temporal structure of large-scale vortices. Kiya, M. [6] states the following remarks; “These are experimental results, which are useful in the design of flow apparatus, but to have experimental results is not equivalent to understand the flow. The advance of numerical simulations and experiments aided by high technology such as lasers and computers is just to make it rapid and economical to obtain the experimental results. A flow is understood when a physical or mathematical model that can predict essential properties of the flow is constructed. In this sense, we have not yet understood separated flows. This is because unsteadiness due to the motion of large-

scale vortices and their three-dimensionality are characteristic of separated flows”.

The main goal on this work is to test the validity of the Navier-Stokes code on the prediction of separated flows, in particular, the ones around the low aspect ratio wings.

1.2. General Features of the Separated Flows

Separated flows can be classified into two categories; the flow without reattachment and the flow with reattachment [6]. The flow without reattachment occurs around cylindrical bluff bodies such as circular cylinders and normal plates and it is characterized by the interaction between vortices, which is shed from the separation points. However, the flow over a backward-facing step, blunt plates or blunt circular cylinders are the typical examples of the flow with reattachment, which is characterized by the interaction between vortices and the solid surface and a separation bubble formation [6].

Separation can be described as the entire process in which a flow detaches from a solid surface, resulting in a breakdown of the boundary layer while undergoing a sudden thickening and causing an increased interaction between the viscous-inviscid layers [7].

Alving & Fernholz [8] make a distinction between separation caused by sharp gradients in the surface geometry, denoted geometry-induced separation, and separation from smooth surfaces caused by adverse pressure gradients -“adverse-pressure-gradient-induced separation” – and discuss in general terms differences between these two cases as seen on Figure 1.2.



Figure 1.2 Separation types

In terms of the leading edge bluntness, the sharp leading edge produces less complex flow with respect to the blunt leading edge [9]. At high Reynolds number, flow past a blunt body typically leads to the formation of a turbulent separation bubble near the sharp corner as well as the emergence of a reattaching flow further downstream [10,13]. The separation bubble is characterized by rolled-up vortices in the shear layer and their interaction with the surface [10-12,14]. The presence of a separated flow, together with a reattaching flow, gives rise to unsteadiness, pressure fluctuations and vibrations of the structure through which the fluid is flowing [15].

The pressure plateaus seen in Figure 1.3 indicate that the speed of the fluid particles in separated flow regions is very slow. This observation led to the common term “dead-air region” or “dead-water region”. Although the static pressure remains almost constant further downstream, the pressure recovers quickly as the aft portion of the time-averaged separation bubble is approached. This corresponds to an intense convection effect inside the bubble.

Separation bubble flow can also be classified as being laminar, transitional or turbulent according to the separation and reattachment status of the boundary layer [16]. In a laminar separation bubble, the boundary layer is laminar at both separation and reattachment points, while in the transitional bubble the boundary layer is still laminar at separation but turbulent at reattachment. If the boundary layer is

turbulent at both separation and reattachment locations, the separation bubble is called turbulent.

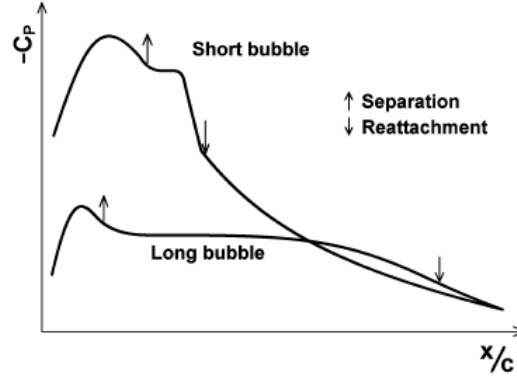


Figure 1.3 Separation bubble formation

Due to the unstable structure of the bubble, turbulent boundary layer may be developed at lower Reynolds numbers, resulting in higher drag. Separation bubbles have gained much attention due to its computational character.

The forward&backward facing step geometries have been extensively studied in much experimental and numerical work on separated flows serve as cornerstone test cases. One reason for this is the fact that the point of separation is fixed in space and time and that separation occurs for all Reynolds numbers [16].

In the case of sharp leading edge bodies, the boundary layer separates from the edge, being shed downstream as a separated shear layer and as we increase the angle of attack, a fully separated flow develops and the wing behaves as a bluff body [6]. Kiya, M. [6,17] states that “spanwise vortices are formed by rolling up the shear layer through the Kelvin-Helmholtz instability to form rectilinear vortex tubes whose

axis is aligned with the edge. The Spanwise vortices merge to become larger and larger with increasing longitudinal distance from the edge. At the same time the spanwise vortices deform in the spanwise direction, being rapidly three-dimensionalized developing turbulence. Large-scale vortices impinge on the surface of the body at a certain longitudinal distance from the edge, being shed downstream. This position of impingement is near the time-mean reattachment position of the shear layer, which is defined as the longitudinal position at which the time-mean streamline starting from the edge reattaches on the surface. The pressure fluctuation generated by the impingement of the vortices propagates upstream to be accepted at the sharp leading edge to generate vorticity fluctuation, which enhances the rolling-up of the shear layer. The resulting large-scale vortices subsequently impinge on the surface. In this sense, the leading edge separation bubble is a self-excited flow maintained by the feedback loop. The feedback mechanism is a working hypothesis, having not been confirmed by experiments or numerical simulations". A description of the different feedback processes for blunt bodies [18] is shown in Figure 1.4.

The number of merging of spanwise vortices up to the impingement position, the length scale of the impinging vortices, and the frequency of their shedding F_v are related to the height of the separated shear layer from the surface [19]. In other words, it is related with the surface pressure just downstream of the edge; the lower the surface pressure, the higher is the curvature or height [6].

The Kelvin-Helmholtz instability and the Shedding-type or Impinging-type of instability [6,19,20] are the two types of instability within the separation bubble.

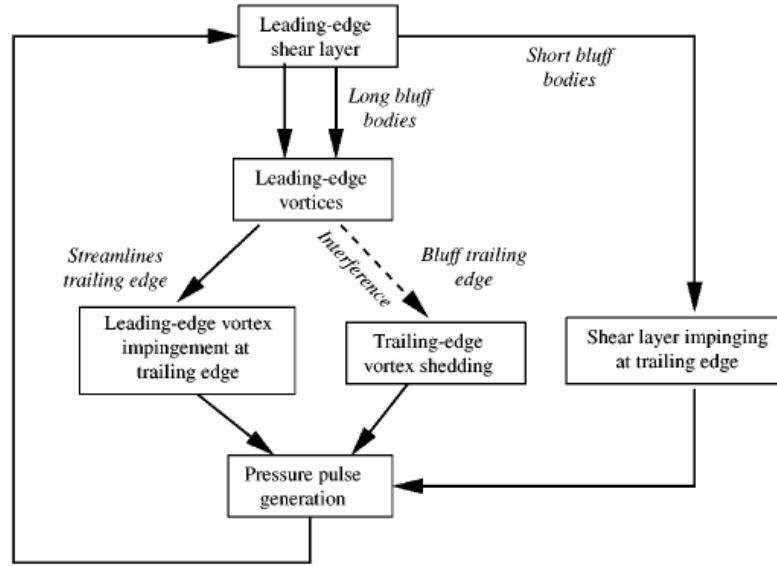


Figure 1.4 Schematic of feedback loops of locked vortex shedding for blunt leading-edge plates with either blunt or streamlined trailing edges [18].

The fundamental frequency of the Kelvin-Helmholtz instability scales to the momentum thickness of the shear layer at the separation edge and the velocity, thus being a function of Reynolds number. On the other hand, the fundamental frequency of the shedding-type instability also called *vortex-shedding frequency* is practically constant at sufficiently high Reynolds numbers. Sigurdson [19] argues that the shedding-type instability is the primary mode of instability in the separation bubble.

Low-frequency modulation is also observed in nominally two-dimensional and axisymmetric separated-and-reattaching flows: backward-facing step flows; leading-edge separation bubbles of blunt plates and blunt circular cylinders. The modulation in these flows is sometimes referred to as flapping because it is accompanied by a transverse oscillation of the separated shear layer. The flapping motion is an intrinsic property of the separation bubbles, not being due to extraneous effects from end effects [6]. The experimental studies (e.g., Cherry et al. [10]; Kiya and Sasaki [11]; Djilali and Gartshore [21]; Saathoff and Melbourne [22]) around a bluff rectangular plates at high

Reynolds numbers report a characteristic low frequency flapping of the separated shear layer as well as pseudo periodic vortex shedding from the separation bubble [23].

Three-dimensional separations can also be classified in three groups with respect to their topology and kinematics shown in Figure 1.5. In Yates and Chapman [24], Horseshoe and Werle type separations are defined as global separations (or closed separations). It is stated clearly in reference [23] that “the predominant structures over the separation bubble are clearly identified as hairpin (horseshoe) vortices in the reattachment region. The legs of the horseshoe vortices are inclined with respect to the streamwise direction. A typical vortex grows in every direction as it is advected downstream of the reattachment region. Due to the interaction between the vortical motion of the large-scale structure and the wall, it also tends to lift away from the wall. This in turn, brings the top end of the horseshoe vortex into contact with the outer (higher velocity) region, resulting in further stretching and inclination of the vortex along the flow direction. Eventually, the central portion breaks down, and only the two inclined legs remain. This phenomenon takes place in the recovery region. The unsteady motion from the shedding of these large-scale vortices causes oscillations and meandering of the instantaneous reattachment (zero-shear stress) line”.

A typical oscillation consists of two distinct phases: (i) gradual growth of large-scale structures in the separated shear layer, accompanied by a progressive growth of the separation bubble, (ii) shedding of a large-scale structure followed by a collapse of the bubble and abrupt shortening of the reattachment length [23].

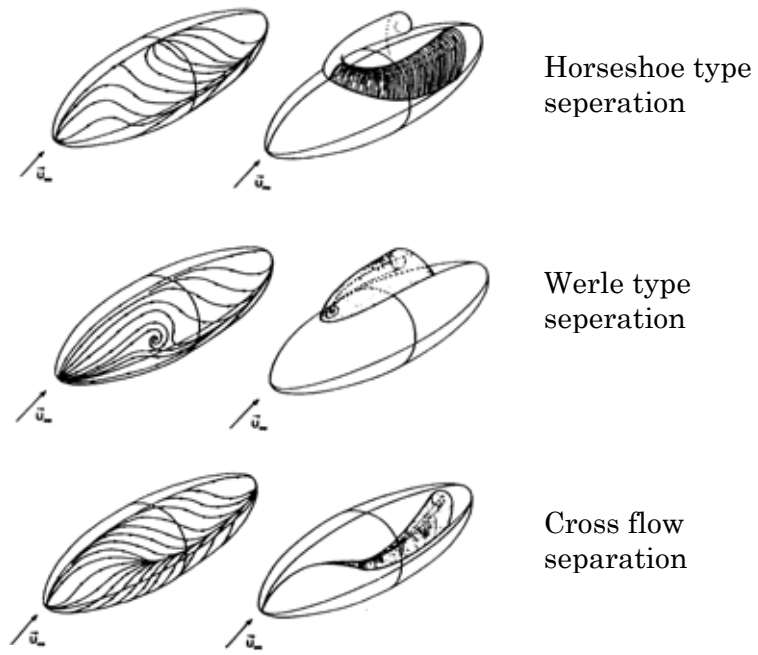


Figure 1.5 Limiting streamline pattern and surfaces of separation for three types of 3-D separation. Taken from Yates and Chapman [24].

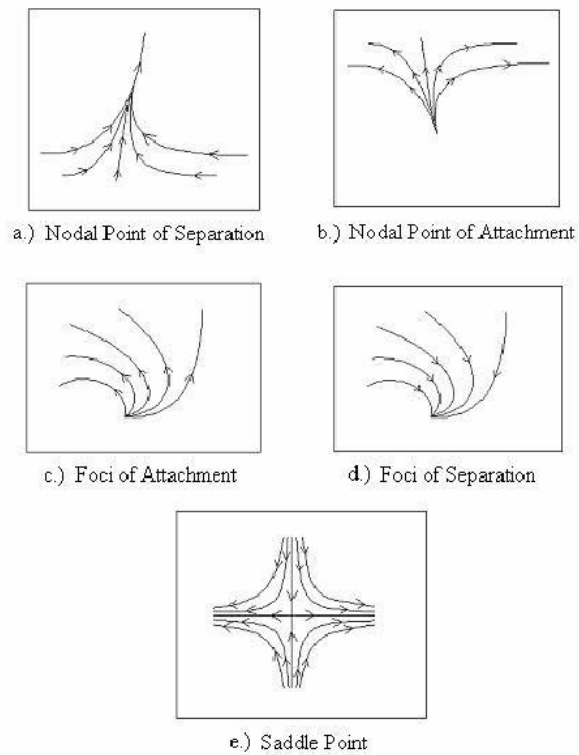


Figure 1.6. Singular points

The structure of 3-D separation can be described by means of the analysis of skin friction lines shown in Figure 1.6. According to Tobak, M. and Peake, D.J [26], when the skin friction lines converge to, or diverge from a point, the point is called node (nodal point of separation or attachment, respectively). Nodal points can have one line to which all skin friction lines are tangent to, or none. Foci differ from nodal points in that an infinite number of streamlines spiral around the node. If the streamlines spiral away from the node, as seen in Figure 1.6.c, the node is defined as a foci of attachment. Streamlines, which spiral into the node, seen in Figure 1.6.d, are defined as foci of separation. Nodal points of separation and attachment can be viewed as sinks and sources of skin friction, respectively. A saddle point may be defined as a singular point in which only two particular lines intersect at the singular point, each of which is in the direction towards or away from the singular point. All other streamlines miss the singular point and follow the directions of the adjacent lines that pass through the singular point as seen in Figure 1.6.e. Both types of points can be featured in the 3-D flow, but the number of nodes must be equal to the number of saddles plus two [27].

Skin friction lines diverging from nodal points cannot cross, due to the presence of a saddle point between them. One of the lines through the saddle is a separation line as seen on Figure 1.7. Skin friction lines converging to, or diverging from, a line define an attachment or separation lines, respectively. These lines are also called limiting streamlines. Limiting streamlines from a separation line must leave the surface, as shown by Lighthill [27], while streamlines converging to an attachment line land on the surface.

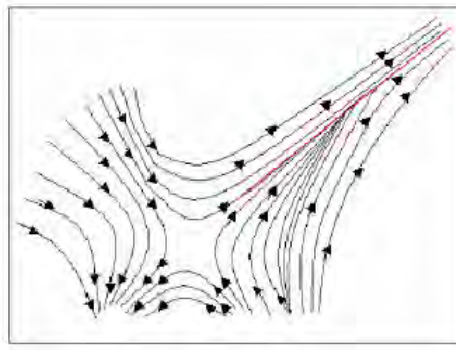


Figure 1.7. Line of separation

Nodal points of separation and attachment are other interesting features: they become edges of vortex cores. In some cases, there is also a distinction between primary and secondary lines of separation. Most researchers agree that the convergence of streamlines on either side of a particular line is a necessary condition for separation however; it should not be used solely to define it as this may occur in other situations as well.

1.3. General Description of the Flowfield around the Low Aspect Ratio Wings

The flowfield around the low aspect ratio wings are mainly characterized by the separations at the leading edge and at the side edges of the wing. The separation at the leading edge leads to separation bubble whereas the separation at the side edges results in tip vortices. There is a strong interference between separation bubble and side vortices at high incidences. This makes the flowfield around these wings quite complicated [28].

At even lower aspect ratios, the wing is subject to strong vortex flows and C_L increases at a faster rate than that predicted with a linear theory [29]. This is due to the presence of the strong tip vortices that separate closer to the leading edge, according to a mechanism similar to

the delta wing. Figure 1.8 shows a qualitative example of how strong an influence the leading edge vortex can have on the lifting characteristics of a short wing.

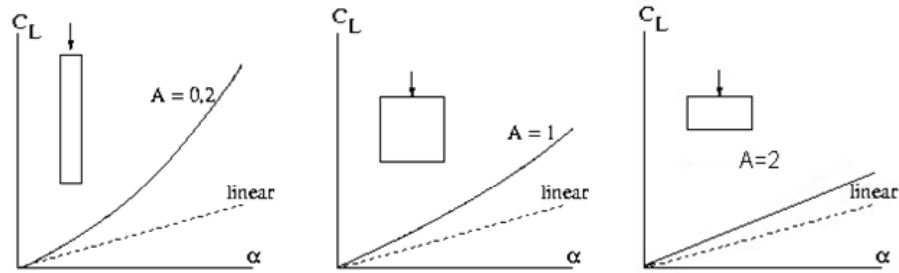


Figure 1.8 The lifting characteristics of wings with low aspect ratios [29].

In Figure 1.9, the oil-flow patterns taken by Wickens [28] are shown on the leeward surface of a low-aspect-ratio rectangular wing at an angle of attack of 20° [30]. Figure 1.10 is a deduction from Figure 1.9 of the corresponding pattern of skin-friction lines. It confirms that the primary separation consists of the dividing surface running into the spiral node nearest the edge of the wing [30]. The saddle point of separation on the wing centerline shows favorable pressure gradients *from leeward to windward* and *from the wing centerline outboard toward the tip of the wing*.

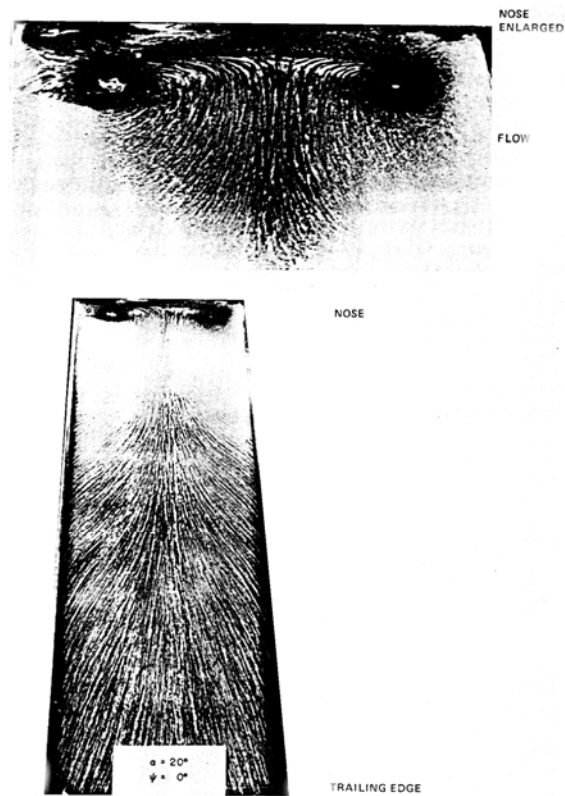


Figure 1.9 Oil-flow pattern on slender, rectangular wing, aspect ratio 0.25 at $\alpha = 20^\circ$ [28]

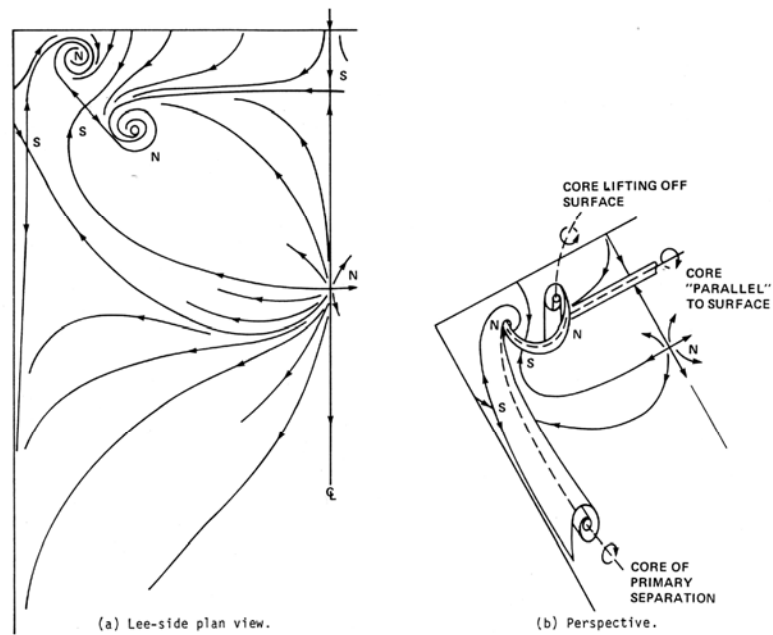


Figure 1.10 Interpretation of skin-friction lines and pressures on slender, rectangular wing, aspect ratio 0.25 at $\alpha = 20^\circ$ [28].

The low aspect ratio rectangular flat wings especially with sharp leading and side edge generally have the flowfield shown in Figure 1.11. Flow separates at the sharp leading edge and forms the leading edge bubble. There are two side, or tip vortices called as spanwise vortices. In the side edges, there exist also secondary vortices and reversed flows also shown in Figure 1.12. Moreover, a secondary bubble underneath the primary bubble is formed as illustrated in Figure 1.13. The rolling up vortices or hairshoe vortices within the separation bubble and the spanwise vortices interact with each other causing a more complex flowfield, which has unsteady, oscillating structure.

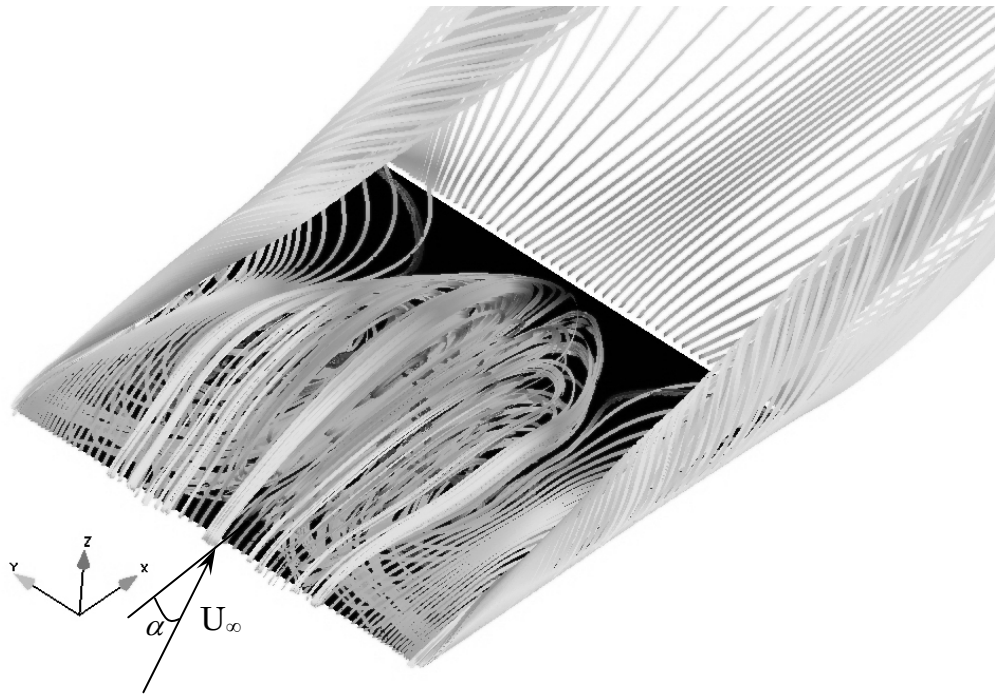


Figure 1.11 Illustrative 3-d flowfield around the low-aspect ratio flat wings.

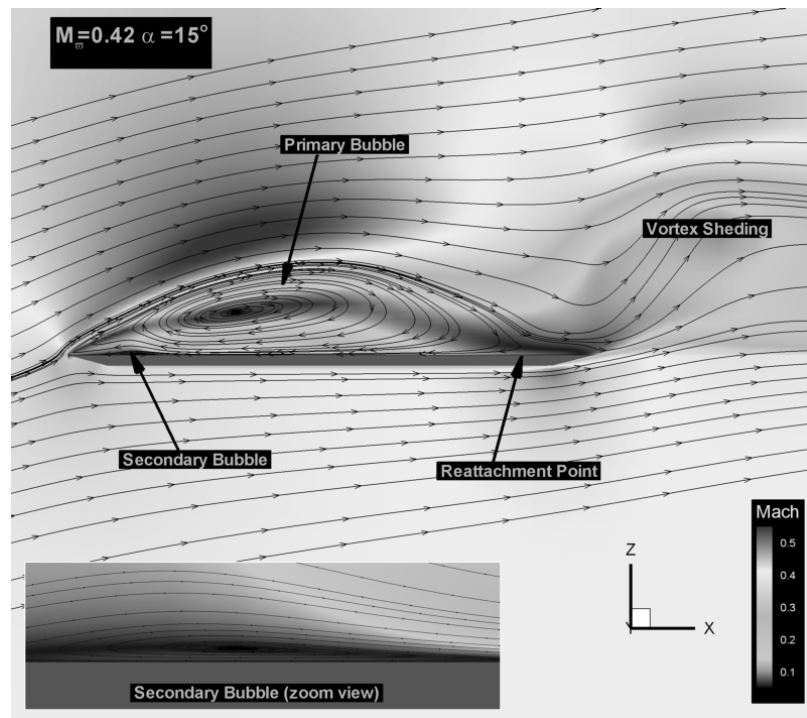


Figure 1.12 Illustrative flowfield at the symmetry plane.

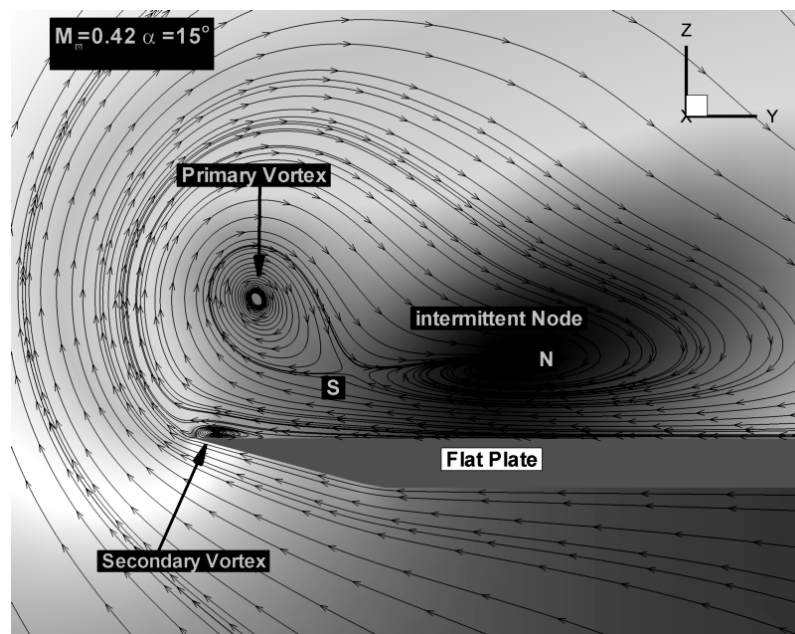


Figure 1.13 Illustrative flowfield at the spanwise plane.

1.4. Literature Review on Low Aspect Ratio Wings

In the past twenty years, great advances in technology have led to significant advances in fluid mechanics. Various publications by AGARD [28,32-35] provide a large selection of research results in this field. Low aspect ratio rectangular flat wings, however were studied much less when compared to the Delta wings of the similar nature. Stahl [36] summarized some of the early research works. Winter [37] obtained pressure distributions on the suction side and force and moment measurements of various low aspect ratio rectangular flat wings at incompressible speeds. At von Karman Institute, similar experiments [38,39] were performed in a transonic wind tunnel for higher speeds.

Simpson [25,41,42] has periodically reviewed the topic of separated flow over the years providing a history of the understanding of turbulent flow separation [40]. A detailed investigation into the literature of the separated and reattaching flow is found by Cherry et al. [10]. A comprehensive review of the global instability was associated with these sorts of flows by Rockwell [43].

Extraction of large-scale vortical structure from turbulent separated and reattaching flows have been studied by numerous studies using conditional averaging techniques [10,12,44]. A strong negative correlation was captured caused by the low-frequency flapping motion of the vortex shedding used a surface pressure sensor to deduce the structure of large-scale vortices [12]. Kiya and Sasaki [12] was identified a saw-tooth like movement of the separation bubble and hairpin vortices in their conditional average. The existence of a large-scale vortex was also indicated by revealing that the location of maximum vorticity coincides with that of maximum turbulence intensity [12,46]. The characteristic frequencies and intermittent nature of the pseudo periodic vortex

shedding from the separated shear layer and the reattachment region, as well as the shear layer flapping were captured in the large-eddy simulation of separated flow over a bluff rectangular plate [23].

Analyses of the leading-edge separation have been performed by many experiments and computations [47,48]. Recent experiment at NASA Langley Research Center investigated effects of leading-edge bluntness and Reynolds-number difference [49,50]. Numerical simulation around delta wing with sharp and blunt leading edges has been performed to investigate the leading edge bluntness and Reynolds-number effects suggested by the experiment [9].

The flow around rectangular plates in the absence of any external forcing has been studied previously both experimentally and numerically [20]. A series of simulations of flows around blunt rectangular plates have been under taken to test the hypothesis that the trailing edge shedding plays an important role in the mechanism leading to self sustained oscillations [6]. The same mechanism may in fact be the feedback loop generated by the impinging leading edge vortices in the absence of trailing edge vortex shedding [43].

The mean flow characteristics and large-scale unsteadiness aspects of turbulent flow around a bluff rectangular plate have been the subject of a number of experimental studies at high Reynolds numbers [10,11,21]. All studies report a characteristic low frequency flapping of the separated shear layer as well as pseudo periodic vortex shedding from the separation bubble [23].

An adequate representation of the mean flow characteristics within the separation bubble have been provided by Reynolds-averaged Navier-Stokes (RANS) Solution of the high Reynolds number turbulent flow [20].

Impinging shear layer instability was initially classified by Nakamura & Nakashima [20] and Nakamura et al. [52]. Later studies [53-57] preferred the description impinging leading edge vortex

instability because it better describes the process wherein leading-edge vortices are shed, convected downstream and then interact with the trailing edges.

The instability waves in the diverging shear flow over square and circular plates were studied in a water tank using flow visualization techniques at angles of attack between 6° and 18° and it was found that small-large scale instability waves were generated in the shear layer over a flat plate at incidence [58].

Alving & Fernholz [59] distinguish between “strong” and “mild” separation bubbles based on the height of the shear layer upstream of separation relative to the height of the separation bubble. A separation bubble is referred to as a “strong” bubble when the height of the shear layer preceding separation is of the same size or smaller than the height of the bubble, whereas, conversely, in a “mild” separation bubble the height of the bubble is considerable smaller than the pre-separated shear layer.

A variety of influences on high angle of attack flow predictions have been discussed, including: governing equation complexity, turbulence modeling, transition modeling, algorithm symmetry, grid generation and density, and numerical dissipation [1]. Non-linear inviscid methods which account for the leading edge vortices and their interactions with the wing surfaces have been developed and modeled the behavior of high Reynolds number , turbulence flow over sharp- edged wings extremely well [60].

Computational procedures allowing aerodynamicists to investigate flows using complex three-dimensional computational fluid dynamics (CFD) to extract the flow topology are now widely available [61]. Delery [62] states that Legendre [63] pioneered flow topology research by proposing that wall streamlines be considered as trajectories having properties consistent with those of a continuous vector field, the principal

being that through any nonsingular point there must pass one and only one trajectory. Different combinations of nodal/saddle points and how they work together have received much attention by Tobak and Peake [26] and Chapman [64]. Since then, much research has been done on fluid flow topology, ranging from Chapman [64] and Wang [65] who classified flow topology for separation on three-dimensional bodies to Cipolla and Rockwell [66] who investigated the instantaneous crossflow topology using particle image velocimetry. Hunt et al. [67] have shown that the notions of singular points and the rules that they obey can be extended to apply to the flow above the surface on planes of symmetry and on crossflow planes. The classification of three-dimensional singular points for flow topology has enabled aerodynamicists to successfully investigate, predict, and fix the separation phenomena alleviating adverse aerodynamic characteristics associated with separation.

1.5. Outline of Dissertation

After introducing the scope of our dissertation, Navier-Stokes equations are presented in detail in Chapter 1. The following chapter focuses on the solution algorithm used. In Chapter 4, the development of hyperbolic grid generation code with upwind differencing is discussed. The turbulence models adapted in the solution are examined in Chapter 5. The Test Cases and Results, which is the section where the most of the work are performed, are presented in Chapter 6. In this chapter, test cases are examined in two main sections. First, two-dimensional test cases are studied within two sub sections; “Laminar Flat Plate” and “Turbulent Flat Plate”. Then, three-dimensional test case; “Three Dimensional Flat Plate”, which is the main goal of the thesis, is presented. Results of each test case are discussed in the corresponding section. In the last chapter, the conclusion and the future work are presented.

CHAPTER 2

NAVIER STOKES EQUATIONS

The governing equations are the Navier-Stokes (N-S) equations. The Reynolds-averaged N-S equations are derived by averaging the viscous conservation laws over a time interval T . The time interval T is chosen large enough with respect to the time scale of the turbulent fluctuations, but has to remain small with respect to the time scales of other time- dependent effects. We consider the Reynolds Averaged N-S equations as the basic model, expressing the conservation laws for mass, momentum and energy written in conservation form

$$\frac{\partial}{\partial t} \begin{pmatrix} \rho \\ \rho \vec{V} \\ \rho e \end{pmatrix} + \vec{\nabla} \cdot \begin{pmatrix} \rho \vec{V} \\ \rho \vec{V} \otimes \vec{V} + p \vec{I} - \vec{\tau} \\ \rho \vec{V} H - \vec{\sigma} \cdot \vec{V} - k \vec{\nabla} T \end{pmatrix} = \begin{pmatrix} 0 \\ \rho \vec{f}_e \\ W_f + q_H \end{pmatrix} \quad (2.1)$$

, or in condensed form

$$\frac{\partial U}{\partial t} + \vec{\nabla} \cdot \vec{F} = Q \quad (2.2)$$

The time dependent N-S equations are hyperbolic-parabolic in space -time while the stationary N-S equations are of mixed type in space that is elliptic-parabolic for subsonic flows and hyperbolic-parabolic for supersonic flows. The physical interpretation of these properties are of great importance for the choice of a numerical scheme, since a hyperbolic system is dominated by wave propagation (or convection) effects, an elliptic system describes diffusion phenomena, while a parabolic system is associated with damped propagation effects. For high Reynolds number flows, the system of conservation equation is convection dominated in

most of the flow region. The N-S equations are often written in vector form as in Equation (2.2). For convenience, the equations are cast in Cartesian coordinate form.

$$\frac{\partial q}{\partial t} + \frac{\partial E}{\partial x} + \frac{\partial F}{\partial y} + \frac{\partial G}{\partial z} + H = \frac{1}{Re} \left(\frac{\partial E_v}{\partial x} + \frac{\partial F_v}{\partial y} + \frac{\partial G_v}{\partial z} \right) \quad (2.3)$$

These five equations are statements of the conservation of mass and energy and conservation of momentum in the x, y and z directions. This form of the equations assumes that the fluid may be compressible and that heat generation and body forces (except for those, which might be included in the source term, H) can be ignored. This vector equation states that the time rate of change in the dependent variables q is equal to the spatial change in the inviscid fluxes, E, F and G, and viscous fluxes, E_v , F_v and G_v . A source term, H, is included to account for the centrifugal and Coriolis force terms, which appear if the coordinate frame is rotating. In the present study, the source term was not taken into account. The presence of the Reynolds number, $Re = \bar{\rho} \bar{u} \bar{L} / \bar{\mu}$, implies that the governing equations have been non-dimensionalized; with $\bar{\rho}$ and \bar{u} often chosen as the freestream density and velocity, \bar{L} chosen as the reference length of the body and $\bar{\mu}$ evaluated at the freestream static temperature. The vector of dependent variables, the inviscid and viscous flux terms are shown below.

$$q = \begin{bmatrix} \rho \\ \rho u \\ \rho v \\ \rho w \\ e \end{bmatrix} \quad E = \begin{bmatrix} \rho u \\ \rho u^2 + p \\ \rho u v \\ \rho u w \\ (e + p)u \end{bmatrix} \quad F = \begin{bmatrix} \rho v \\ \rho u v \\ \rho v^2 + p \\ \rho v w \\ (e + p)v \end{bmatrix}$$

$$\begin{aligned}
G &= \begin{bmatrix} \rho w \\ \rho u w \\ \rho v w \\ \rho w^2 + p \\ (e + p)w \end{bmatrix} & E_v &= \begin{bmatrix} 0 \\ \tau_{xx} \\ \tau_{xy} \\ \tau_{xz} \\ u\tau_{xx} + v\tau_{xy} + w\tau_{xz} - q_x \end{bmatrix} \\
F_v &= \begin{bmatrix} 0 \\ \tau_{yx} \\ \tau_{yy} \\ \tau_{yz} \\ u\tau_{yx} + v\tau_{yy} + w\tau_{yz} - q_y \end{bmatrix} & G_v &= \begin{bmatrix} 0 \\ \tau_{zx} \\ \tau_{zy} \\ \tau_{zz} \\ u\tau_{zx} + v\tau_{zy} + w\tau_{zz} - q_z \end{bmatrix}
\end{aligned}$$

Here ρ is the fluid density; u , v and w are the fluid velocities in the x , y and z coordinate directions, and e is the total energy per unit volume. The viscous flux terms are functions of the local fluid velocities, the shear stresses, τ_{xx} , and heat conduction terms q_x , q_y and q_z .

The pressure, p , which appears in the inviscid flux terms, is related to the dependent variables through an appropriate equation of state. The local pressure is expressed in terms of the dependent variables by applying the ideal gas law.

$$p = (\gamma - 1) \left[e - \frac{1}{2} \rho (u^2 + v^2 + w^2) \right] \quad (2.4)$$

The stresses are related to the velocity gradient of the fluid, assuming a Newtonian fluid for which the viscous stress is proportional to the rate of shearing strain (i.e. angular deformation rate). For turbulent flow, a Reynolds-averaged form of the equations is used where the dependent variables represent the mean flow contribution. The Boussinesq assumption is applied, permitting the apparent turbulent stresses to be related to the product of the mean flow strain rate and an apparent turbulent viscosity. Therefore, the shear and normal stress tensors have the following form;

$$\begin{aligned}\sigma_{ij} &= -p\delta_{ij} + (\mu + \mu_T) \left[\left(\frac{\partial u_i}{\partial x_j} + \frac{\partial u_j}{\partial x_i} \right) - \frac{2}{3} \delta_{ij} \frac{\partial u_k}{\partial x_k} \right] \\ \tau_{ij} &= (\mu + \mu_T) \left[\left(\frac{\partial u_i}{\partial x_j} + \frac{\partial u_j}{\partial x_i} \right) - \frac{2}{3} \delta_{ij} \frac{\partial u_k}{\partial x_k} \right]\end{aligned}\tag{2.5}$$

The heat conduction terms, when Reynolds-averaging and the Boussinesq assumption are applied, are proportional to the local mean flow temperature gradient;

$$q_i = \frac{-1}{(\gamma - 1)PrM_\infty^2} (k + k_T) \frac{\partial T}{\partial x_i}\tag{2.6}$$

Here, γ represents the ratio of specific heats, Pr is the Prandtl number and M_∞ is the freestream Mach number.

To determine the effective turbulent conductivity, k_T , Reynolds analogy is applied and the turbulent conductivity is related to the turbulent viscosity as follows;

$$k_T = \frac{Pr}{Pr_T} \mu_T\tag{2.7}$$

Here, and in the equation above, the conductivity and viscosity are non-dimensionalized by their representative (laminar) values evaluated at the freestream static temperature.

In many CFD applications, it is desirable to solve the governing equations in a domain, which has surfaces that conform to the body rather than in a Cartesian coordinate domain. A transformation is applied to the original set of equations to obtain a "generalized geometry" form of the governing equations. This allows the irregular shaped physical domain to be transformed into a rectangular shaped computational domain that allows the numeric to be simplified somewhat. This transformation also simplifies the applications of the boundary conditions and may include various options on grid point

clustering and orthogonality, both being extremely important for the solution of the Navier-Stokes equations. Obviously, grid point clustering near the surface for viscous flows is required in order to resolve the flow gradient. The transformed equations are shown below,

$$\frac{\partial \hat{q}}{\partial \tau} + \frac{\partial \hat{E}}{\partial \xi} + \frac{\partial \hat{F}}{\partial \eta} + \frac{\partial \hat{G}}{\partial \zeta} = \frac{1}{\text{Re}} \left(\frac{\partial \hat{E}_v}{\partial \xi} + \frac{\partial \hat{F}_v}{\partial \eta} + \frac{\partial \hat{G}_v}{\partial \zeta} \right) \quad (2.8)$$

Typically, the physical domain is oriented in such a way that the coordinate directions in the computational domain; $[\xi, \eta, \zeta]$ may correspond to directions relative to the body. In the applications discussed here, ξ corresponds to the direction along the body, η corresponds to the circumferential direction and ζ corresponds to the outward direction from the body surface. Also, τ represents time. Note that the source term, H , is not included to the Equation(2.8).

The transformed fluxes are functions of the original Cartesian flux terms and have a similar form. After rearranging, the vector of dependent variables and inviscid and viscous flux terms take the following form,

$$\begin{aligned} \hat{q} = \frac{1}{J} \begin{bmatrix} \rho \\ \rho u \\ \rho v \\ \rho w \\ e \end{bmatrix} \quad \hat{E} = \frac{1}{J} \begin{bmatrix} \rho U \\ \rho u U + \xi_x p \\ \rho v U + \xi_y p \\ \rho w U + \xi_z p \\ (e + p)U - \xi_t p \end{bmatrix} \quad \hat{F} = \frac{1}{J} \begin{bmatrix} \rho V \\ \rho u V + \eta_x p \\ \rho v V + \eta_y p \\ \rho w V + \eta_z p \\ (e + p)V - \eta_t p \end{bmatrix} \\ \hat{G} = \frac{1}{J} \begin{bmatrix} \rho W \\ \rho u W + \zeta_x p \\ \rho v W + \zeta_y p \\ \rho w W + \zeta_z p \\ (e + p)W - \zeta_t p \end{bmatrix} \quad \hat{E}_v = \frac{1}{J} \begin{bmatrix} 0 \\ \xi_x \tau_{xx} + \xi_y \tau_{xy} + \xi_z \tau_{xz} \\ \xi_x \tau_{xy} + \xi_y \tau_{yy} + \xi_z \tau_{zy} \\ \xi_x \tau_{xz} + \xi_y \tau_{yz} + \xi_z \tau_{zz} \\ \xi_x A + \xi_y B + \xi_z C \end{bmatrix} \end{aligned}$$

$$\hat{F}_v = \frac{1}{J} \begin{bmatrix} 0 \\ \eta_x \tau_{xx} + \eta_y \tau_{xy} + \eta_z \tau_{xz} \\ \eta_x \tau_{xy} + \eta_y \tau_{yy} + \eta_z \tau_{zy} \\ \eta_x \tau_{xz} + \eta_y \tau_{yz} + \eta_z \tau_{zz} \\ \eta_x A + \eta_y B + \eta_z C \end{bmatrix} \quad \hat{G}_v = \frac{1}{J} \begin{bmatrix} 0 \\ \zeta_x \tau_{xx} + \zeta_y \tau_{xy} + \zeta_z \tau_{xz} \\ \zeta_x \tau_{xy} + \zeta_y \tau_{yy} + \zeta_z \tau_{zy} \\ \zeta_x \tau_{xz} + \zeta_y \tau_{yz} + \zeta_z \tau_{zz} \\ \zeta_x A + \zeta_y B + \zeta_z C \end{bmatrix} \quad (2.9)$$

where

$$\begin{aligned} A &= u \tau_{xx} + v \tau_{xy} + w \tau_{xz} - q_x \\ B &= u \tau_{yx} + v \tau_{yy} + w \tau_{yz} - q_y \\ C &= u \tau_{zx} + v \tau_{zy} + w \tau_{zz} - q_z \end{aligned}$$

The velocities in the ξ , η and ζ coordinates represent the contravariant velocity components.

$$\begin{aligned} U &= \xi_t + \xi_x u + \xi_y v + \xi_z w \\ V &= \eta_t + \eta_x u + \eta_y v + \eta_z w \\ W &= \zeta_t + \zeta_x u + \zeta_y v + \zeta_z w \end{aligned} \quad (2.10)$$

The Cartesian velocity components (U , V , W) are retained as the dependent variables and are non-dimensionalized with respect to a_∞ (the freestream speed of sound). In addition to the original Cartesian variables, additional terms ($J, \xi_x, \eta_y, \zeta_z, \dots$) appear in the equations. These terms referred to as the metric terms, result from the transformation and contain the purely geometric information that relates the physical space to the computational space. The metric terms are defined as

$$\begin{aligned} \xi_x &= J(y_\eta z_\zeta - y_\zeta z_\eta) & \eta_x &= J(z_\xi y_\zeta - y_\xi z_\zeta) & \zeta_x &= J(y_\xi z_\eta - z_\xi y_\eta) \\ \xi_y &= J(z_\eta x_\zeta - x_\eta z_\zeta) & \eta_y &= J(x_\xi z_\zeta - x_\zeta z_\xi) & \zeta_y &= J(z_\xi x_\eta - x_\xi z_\eta) \\ \xi_z &= J(x_\eta y_\zeta - y_\eta x_\zeta) & \eta_z &= J(y_\xi x_\zeta - x_\xi y_\zeta) & \zeta_z &= J(x_\xi y_\eta - y_\xi x_\eta) \end{aligned} \quad (2.11)$$

and

$$J^{-1} = \frac{\partial(x, y, z)}{\partial(\xi, \eta, \zeta)} = x_{\xi}y_{\eta}z_{\zeta} + x_{\zeta}y_{\xi}z_{\eta} + x_{\eta}y_{\zeta}z_{\xi} - x_{\xi}y_{\zeta}z_{\eta} - x_{\eta}y_{\xi}z_{\zeta} - x_{\zeta}y_{\eta}z_{\xi} \quad (2.12)$$

The metrics are evaluated using second-order, central difference formulas for interior points and three-point, one-sided formulas at the boundaries. Further simplification of the governing equations shown above is often desirable and physically justified. In many applications, the viscous effects are limited to the boundary layers near the body surfaces or along shear layers that are normal to a single grid direction. In such cases, it may be desirable to include only the most dominant viscous terms in similar fashion as the boundary layer equations. Indeed, from a computational perspective, for viscous effects to be properly modeled, the relevant viscous terms must be included in the governing equations and the flow field gradients must be resolved with sufficient accuracy on the computational mesh. For these reasons, a simplified form of the governing equations is applied in general. This set of equations is often referred to as the "Thin Layer" N-S equations. In a fashion similar to the boundary layer length scale analysis, only viscous terms, which involve derivatives along a single coordinate direction (typically normal to the body surface), are retained and the other viscous terms are dropped. At this point only a single vector of terms remains.

$$\frac{\partial \hat{q}}{\partial \tau} + \frac{\partial \hat{E}}{\partial \xi} + \frac{\partial \hat{F}}{\partial \eta} + \frac{\partial \hat{G}}{\partial \zeta} = \frac{1}{\text{Re}} \frac{\partial \hat{S}}{\partial \zeta} \quad (2.13)$$

where

$$\hat{S} = J^{-1} \begin{bmatrix} 0 \\ \mu A u_{\zeta} + \left(\frac{\mu}{3}\right) C \zeta_x \\ \mu A v_{\zeta} + \left(\frac{\mu}{3}\right) C \zeta_y \\ \mu A w_{\zeta} + \left(\frac{\mu}{3}\right) C \zeta_z \\ \left\{ A \left[0.5 \mu (V^2)_{\zeta} + \kappa Pr^{-1} (\gamma - 1)^{-1} (a^2)_{\zeta} \right] + \left(\frac{\mu}{3}\right) BC \right\} \end{bmatrix} \quad (2.14)$$

$$\begin{aligned}
A &= \zeta_x^2 + \zeta_y^2 + \zeta_z^2 & \mathbf{V}^2 &= u^2 + v^2 + w^2 \\
\text{with } B &= \zeta_x u + \zeta_y v + \zeta_z w & \kappa &= \frac{1}{\gamma R M_\infty^2} \\
C &= \zeta_x u_\zeta + \zeta_y v_\zeta + \zeta_z w_\zeta
\end{aligned}$$

With this form of equations, the cross-derivatives in the viscous terms have been eliminated. The equations are now in a form, which is amenable to solution by direct implicit numerical techniques such as the Beam and Warming algorithm.

CHAPTER 3

SOLUTION ALGORITHM

The numerical scheme used for the solution of the Thin Layer N-S equations is generally based on a fully implicit, approximately factored, finite difference algorithm in delta form [82]. Implicit methods with the delta form are widely used for solving steady state problems since the steady state solutions are indifferent to the left-hand side operators.

The solution of the three-dimensional equations is implemented by an approximate factorization that allows the system of equations to be solved in three coupled one-dimensional steps. The most commonly used method is the Beam and Warming one [83]. The LU-ADI factorization [84] is one of those schemes that simplify inversion works for the left-hand side operators of the Beam and Warming's. Each ADI operator is decomposed to the product of the lower and upper bi-diagonal matrices by using the flux vector splitting technique [84].

To maintain the stability, the diagonally dominant LU factorization is adopted. The explicit part is left to be the same as the Beam and Warming's where central differencing is used. .

As indicated in Equation (2.13) , this solution technique involves solving the time-dependent N-S equations. The procedure is started by assuming a uniform, free-stream solution for all grid points in the computational domain. The calculation then marches in time until a steady state solution is obtained subject to the imposed boundary conditions.

Beam and Warming method applied to Equation (2.13) leads to the following approximate factorization form,

$$\begin{aligned}
& \left(I + h\delta_\xi \hat{A}^n - \epsilon_i J^{-1} \nabla_\xi \Delta_\xi J \right) \times \left(I + h\delta_\eta \hat{B}^n - \epsilon_i J^{-1} \nabla_\eta \Delta_\eta J \right) \times \\
& \left(I + h\delta_\zeta \hat{C}^n - h\text{Re}^{-1} \delta_\zeta \hat{M}^n - \epsilon_i J^{-1} \nabla_\zeta \Delta_\zeta J \right) \times \left(\hat{Q}^{n+1} - \hat{Q}^n \right) \\
& = -h \left(\delta_\xi \hat{E}^n + \delta_\eta \hat{F}^n + \delta_\zeta \hat{G}^n - \text{Re}^{-1} \delta_\zeta \hat{S}^n \right) - \epsilon_e J^{-1} \left[(\nabla_\xi \Delta_\xi)^2 + (\nabla_\eta \Delta_\eta)^2 + (\nabla_\zeta \Delta_\zeta)^2 \right] J Q^n
\end{aligned} \tag{3.1}$$

where $h = \Delta t$, δ is the central finite difference operator, and Δ and ∇ are forward and backward difference operators, respectively.

For the convective terms in the right hand side, fourth order differencing is used. Maintenance of the freestream is achieved by subtracting the freestream fluxes from the governing equations.

For the ξ direction, the Beam and Warming's ADI operator can be written in the diagonal form as follows,

$$I + h\delta_\xi \hat{A} + J^{-1} \epsilon_i \delta_\xi^2 J = T_\xi \left[I + h\delta_\xi \hat{D}_A + J^{-1} \epsilon_i \delta_\xi^2 J \right] T_\xi^{-1} \tag{3.2}$$

where

$$\hat{A} = T_\xi \hat{D}_A T_\xi^{-1} \quad .$$

The flux vector splitting technique is used to decompose the central differencing to two one sided differencing.

$$\hat{A} = T_\xi \left[I + \nabla_\xi D_A^+ + \Delta_\xi D_A^- \right] T_\xi^{-1} \tag{3.3}$$

with

$$D_A^\pm = \frac{h}{2} \left(\hat{D}_A \pm \left| \hat{D}_A \right| \right) \pm \bar{J}^{-1} \epsilon_i J \tag{3.4}$$

where \bar{J}^{-1} is taken to be the Jacobian at the central point corresponding to Equation (3.2). Equation (3.3) can be rewritten as,

$$\hat{A} = T_\xi \left[L_A + M_A + N_A \right] T_\xi^{-1} \tag{3.5}$$

where for three point upwinding,

$$L_A = -\frac{8}{6}D_{A_{j-1}}^+ + \frac{1}{6}D_{A_{j-2}}^+,$$

$$M_A = I + \frac{7}{6}(D_{A_j}^+ - D_{A_j}^-),$$

$$N_A = \frac{8}{6}D_{A_{j+1}}^- - \frac{1}{6}D_{A_{j+2}}^-,$$

The diagonally dominant factorization used here can be described as,

$$L_A + M_A + N_A = (L_A + M_A)M_A^{-1}(M_A + N_A) + O(h^2) \quad (3.6)$$

since $M_A = O(1)$ and $L_A, N_A = O(h)$.

Thus, the LU factorization for an ADI operator can be obtained as

$$I + h \delta_\zeta \hat{A} + J^{-1} \in_i \delta_\zeta^2 J = T_\zeta (L_A + M_A) M_A^{-1} (M_A + N_A) T_\zeta^{-1} \quad (3.7)$$

By this, the block tri-diagonal system is decomposed to the product of the lower and upper scalar bi-diagonal ones, $L_A + M_A$ and $M_A^{-1}(M_A + N_A)$.

In order to maintain the stability of the thin layer viscous terms, the splitted Jacobian matrices \hat{C}^\pm are modified as follows,

$$\hat{C}_v^\pm = T_\zeta \left(\hat{D}_C^\pm \pm \nu \ I \right) T_\zeta^{-1} \quad (3.8)$$

where

$$\nu = 2\mu r_\zeta^2 / Re \rho \Delta \zeta \quad (3.9)$$

At the end, the Beam and Warming Scheme can be described as follows by using the similar procedure for the other operators,

$$T_\zeta \times (L_A + M_A) \times M_A^{-1} \times (M_A + N_A) \times (T_\zeta^{-1} T_\eta) \times (L_B + M_B) \times M_B^{-1} \times (M_B + N_B) \times \\ (T_\eta^{-1} T_\zeta) \times (L_C + M_C) \times M_C^{-1} \times (M_C + N_C) \times T_\zeta^{-1} \times \Delta \hat{U}^n = RHS$$

of (3.1).

As far as accuracy is concerned, the basic algorithm is first order accurate in time and second order accurate in space. Convergence, stability and smoothness of the solution depend on the implicit and explicit smoothing factors, ϵ_i and ϵ_e and Courant-Friedrich-Lewy (CFL) number. Physically, the CFL number indicates the relation between one spatial step-size Δx movement in one time step Δt . Numerically, CFL number is defined as:

$$CFL = \frac{\Delta t \cdot \sigma_{\max}}{\min(\Delta \xi, \Delta \eta, \Delta \zeta)} \quad (3.10)$$

Here σ_{\max} is the maximum eigenvalue. Starting from the definition of speed of sound, σ_{\max} is defined as follows

$$\sigma_{\max} = \max(\sigma_A, \sigma_B, \sigma_C) \quad (3.11)$$

where

$$c^2 = \frac{\gamma p}{\rho} = \gamma(\gamma - 1) \left(\frac{e}{\rho} - \frac{u^2 + v^2 + w^2}{2} \right) \quad \text{and}$$

$$\begin{aligned} \sigma_A &= U + c \sqrt{\xi_x^2 + \xi_y^2 + \xi_z^2} \\ \sigma_B &= V + c \sqrt{\eta_x^2 + \eta_y^2 + \eta_z^2} \\ \sigma_C &= W + c \sqrt{\zeta_x^2 + \zeta_y^2 + \zeta_z^2} \end{aligned}$$

U , V and W were defined in Equation (2.10).

In order to simulate turbulence effects, the viscous coefficient is computed as the sum of laminar viscosity and turbulence viscosity. The turbulent eddy viscosity is then calculated by using the two-layer algebraic turbulence model proposed by Baldwin and Lomax.

CHAPTER 4

HYPERBOLIC GRID GENERATION WITH UPWIND DIFFERENCING

Hyperbolic grid generation provides efficiency, orthogonality and superior control of the grid spacing. A conventional hyperbolic grid generation method employs a central difference scheme and second- and fourth-order dissipation terms are explicitly added for preventing oscillation. These dissipation terms include user-specified constants. Therefore, the decision of the constants strongly depends on the user's experience. When the added dissipation is large, the grid-orthogonality will be spoiled. On the contrary, when the dissipation is small the grid smoothness will not be achieved and in the worst case, grid-line crossing will occur.

An upwind difference scheme can be applied to the hyperbolic grid generation since the system of the hyperbolic partial differential equations has real distinct eigenvalues. Tai et al. [70] has applied the Roe's flux-difference scheme to the hyperbolic grid generation, and demonstrates excellent results employing first-order accurate upwind scheme. The upwind scheme does not require the user-specified parameters in general.

4.1. Governing Equations

The goal is to create a volume or surface grid by propagating grid points from a given surface grid along a specified trajectory. The grid point propagation is constrained by the equations defining the direction of propagation (orthogonality) and the grid point spacing in the marching

direction. These constraint equations are found to be hyperbolic, making a marching solution possible

A three dimensional grid point is defined as $\vec{r} \equiv [x, y, z]^T$. The computational coordinate system is defined using the three coordinates ξ , η and ζ . The computational indices corresponding to the computational coordinates are i, j and k respectively.

Generalized coordinates $\xi(x, y, z)$, $\eta(x, y, z)$, $\zeta(x, y, z)$ are sought where the body surface is chosen to coincide with $\zeta(x, y, z) = 0$ and surface distributions of $\xi = \text{constant}$ and $\eta = \text{constant}$ are user specified [68].

The governing equations are derived from orthogonality relations between ξ and ζ , between η and ζ , and a cell volume constraint. Actually, the constraint equations specify that the grid lines are to propagate from the initial grid along a given trajectory and that the grid cell size is to grow accordingly to a given function.

Hence, the mathematical development is based on three constraints to allow a marching solution in the ζ direction for the three unknowns x, y and z . The first two constraint imposes orthogonality of grid lines at the surface as well as the interior domain. The third constraint specifies the finite Jacobian, J [69].

The grid line trajectory in the marching direction is defined by two angle (orthogonality) constraints:

$$\vec{r}_\xi \cdot \vec{r}_\zeta = 0 \quad (4.1)$$

and

$$\vec{r}_\eta \cdot \vec{r}_\zeta = 0 \quad (4.2)$$

The third constraint is actually a specification of cell volume according to

$$\vec{r}_\xi \cdot (\vec{r}_\eta \times \vec{r}_\zeta) = J^{-1} = V \quad (4.3)$$

Alternatively, in an expanded form, we can get the following system of equations

$$\begin{aligned}
\vec{r}_\xi \cdot \vec{r}_\zeta &= x_\xi x_\zeta + y_\xi y_\zeta + z_\xi z_\zeta = 0 \\
\vec{r}_\eta \cdot \vec{r}_\zeta &= x_\eta x_\zeta + y_\eta y_\zeta + z_\eta z_\zeta = 0 \\
\vec{r}_\xi \cdot (\vec{r}_\eta \times \vec{r}_\zeta) &= x_\xi y_\eta z_\zeta + x_\eta y_\zeta z_\xi + x_\zeta y_\xi z_\eta - (x_\xi y_\zeta z_\eta + x_\eta y_\xi z_\zeta + x_\zeta y_\eta z_\xi) = V
\end{aligned} \tag{4.4}$$

Since the constraint equations form a system of nonlinear partial differential equations, the system must be linearized about a known state \vec{r}_0 in order to facilitate their numerical solution [69].

We define

$$\begin{aligned}
x &= x_0 + \Delta x \\
y &= y_0 + \Delta y \\
z &= z_0 + \Delta z
\end{aligned} \tag{4.5}$$

, or

$$\vec{r} = \vec{r}_0 + \Delta \vec{r} \tag{4.6}$$

After some manipulations, we get the linearized system in conventional form,

$$A_0 \vec{r}_\xi + B_0 \vec{r}_\eta + C_0 \vec{r}_\zeta = \vec{f} \tag{4.7}$$

and the coefficient matrices in the above equation.

$$\begin{aligned}
A_0 &= \begin{bmatrix} x_\zeta & y_\zeta & z_\zeta \\ 0 & 0 & 0 \\ (y_\eta z_\zeta - y_\zeta z_\eta) & (x_\zeta z_\eta - x_\eta z_\zeta) & (x_\eta y_\zeta - x_\zeta y_\eta) \end{bmatrix}_0 \\
B_0 &= \begin{bmatrix} 0 & 0 & 0 \\ x_\zeta & y_\zeta & z_\zeta \\ (y_\zeta z_\xi - y_\xi z_\zeta) & (x_\xi z_\zeta - x_\zeta z_\xi) & (x_\zeta y_\xi - x_\xi y_\zeta) \end{bmatrix}_0 \\
C_0 &= \begin{bmatrix} x_\xi & y_\xi & z_\xi \\ x_\eta & y_\eta & z_\eta \\ (y_\xi z_\eta - y_\eta z_\xi) & (x_\eta z_\xi - x_\xi z_\eta) & (x_\xi y_\eta - x_\eta y_\xi) \end{bmatrix}_0 \\
\vec{f} &= \begin{bmatrix} 0 \\ 0 \\ V + 2V_0 \end{bmatrix}
\end{aligned} \tag{4.8}$$

Roe's upwind scheme will be used to solve the conventional form of the hyperbolic equations. By isolating the r_ζ term, we can write the Equation (4.7) (Notice that C_0^{-1} exists unless $\text{Det}(C_0) \rightarrow 0$) as

$$\begin{aligned}
D\vec{r}_\zeta + E\vec{r}_\eta + \vec{r}_\zeta &= C_0^{-1}\vec{f} \\
\text{where } D &= C_0^{-1}A_0 \quad \text{and} \quad E = C_0^{-1}B_0
\end{aligned} \tag{4.9}$$

The above equation is in non-conservative form. After writing this equation in conservative form and obtaining the fluxes using Roe's upwind scheme, it is discretized [69] as,

$$\begin{aligned}
&\frac{1}{2}(D - \lambda_{i+\frac{1}{2}}I)r_{i+1} + \frac{1}{2}(\lambda_{i+\frac{1}{2}} + \lambda_{i-\frac{1}{2}})r_i - \frac{1}{2}(D + \lambda_{i-\frac{1}{2}}I)r_{i-1} + \\
&\frac{1}{2}(E - \beta_{j+\frac{1}{2}}I)r_{j+1} + \frac{1}{2}(\beta_{j+\frac{1}{2}} + \beta_{j-\frac{1}{2}})r_j - \frac{1}{2}(E + \beta_{j-\frac{1}{2}}I)r_{j-1} + r_\zeta = C_0^{-1}f
\end{aligned} \tag{4.10}$$

where

$$\begin{aligned}
\lambda &= \sqrt{-(d_{11}d_{22} - d_{12}d_{21} + d_{11}d_{33} - d_{13}d_{31} + d_{22}d_{33} - d_{23}d_{32})} \\
\beta &= \sqrt{-(e_{11}e_{22} - e_{12}e_{21} + e_{11}e_{33} - e_{13}e_{31} + e_{22}e_{33} - e_{23}e_{32})}
\end{aligned}$$

λ and β are the eigenvalues of the matrixes D and E respectively [70]. Further manipulations results in

$$\begin{aligned} \nabla_{\zeta} \vec{r} + D\delta_{\xi} \nabla_{\zeta} \vec{r} + E\delta_{\eta} \nabla_{\zeta} \vec{r} - \frac{1}{2} \varepsilon_{\eta} (\Delta \nabla)_{\eta} \nabla_{\zeta} \vec{r} - \frac{1}{2} \varepsilon_{\xi} (\Delta \nabla)_{\xi} \nabla_{\zeta} \vec{r} = C_0^{-1} \vec{g} \quad , \text{or} \\ \left[I + D\delta_{\xi} + E\delta_{\eta} - \frac{1}{2} \varepsilon_{\eta} (\Delta \nabla)_{\eta} - \frac{1}{2} \varepsilon_{\xi} (\Delta \nabla)_{\xi} \right] \nabla_{\zeta} \vec{r} = C_0^{-1} \vec{g} \end{aligned} \quad (4.11)$$

This multi dimensional finite difference equation can be further simplified by the Approximate Factorization in order to get a numerical solution obtained by a series of finite difference equations, which can be represented as block tridiagonal formulations [2].

$$\left[I + D\delta_{\xi} - \frac{1}{2} \varepsilon_{\xi} (\Delta \nabla)_{\xi} \right] \left[I + E\delta_{\eta} - \frac{1}{2} \varepsilon_{\eta} (\Delta \nabla)_{\eta} \right] \nabla_{\zeta} \vec{r} = C_0^{-1} \vec{g} \quad (4.12)$$

Then the above equation can be formulated by three steps resulting in an intermediate solution, \vec{T}_{k+1} and the position vector, \vec{r}_{k+1} and can be solved by any block tridiagonal solver [68]. Reference state (0) used in computation of the next marching step ($k+1$) is obtained from the previous marching location (k). Replacing $\nabla_{\zeta} \vec{r}$ with the vector \vec{d}_{k+1} , we can get the following relations.

First step;

$$\left[E\delta_{\eta} + I \right] \vec{T}_{k+1} = C_k^{-1} \vec{g}_{k+1} \quad \eta \quad \text{sweep} \quad (4.13)$$

Second step;

$$\left[D\delta_{\xi} + I \right] \vec{d}_{k+1} = \vec{T}_{k+1} \quad \xi \quad \text{sweep} \quad (4.14)$$

Third step;

$$\vec{r}_{k+1} = \vec{r}_k + \vec{d}_{k+1} \quad (4.15)$$

In order to see the internal structure of the system we can write the above equations in an expanded form for each step.

For the η sweep algorithm at any (i,j,k) location we can write the Equation (4.13) as

$$\boxed{-\frac{1}{2}E_{i,j,k} \underline{\underline{\vec{T}_{i,j-1,k+1}}} + I \underline{\underline{\vec{T}_{i,j,k+1}}} + \frac{1}{2}E_{i,j,k} \underline{\underline{\vec{T}_{i,j+1,k+1}}} = C^{-1}_{i,j,k} \vec{g}_{i,j,k+1}} \quad (4.16)$$

Note that the unknown vector $\underline{\underline{\vec{T}_{k+1}}}$ is underlined.

For the ξ sweep algorithm, at any (i,j,k) location we can write the Equation (4.14) as

$$\boxed{-\frac{1}{2}D_{i,j,k} \underline{\underline{\vec{d}_{i,j-1,k+1}}} + I \underline{\underline{\vec{d}_{i,j,k+1}}} + \frac{1}{2}D_{i,j,k} \underline{\underline{\vec{d}_{i,j+1,k+1}}} = T_{i,j,k+1}} \quad (4.17)$$

Note that the unknown vector $\underline{\underline{\vec{d}_{k+1}}}$ is underlined

The coefficient matrices A, B and C contain derivatives in ξ , η and ζ . The derivatives in ξ and η are obtained by central differencing while the derivatives in ζ are obtained from the system of Equation (4.4) as a linear combination of ξ - and η -derivatives as follows,

$$\begin{pmatrix} x_\zeta \\ y_\zeta \\ z_\zeta \end{pmatrix} = \frac{V}{Det(C)} \begin{pmatrix} y_\xi z_\eta - y_\eta z_\xi \\ z_\xi x_\eta - z_\eta x_\xi \\ x_\xi y_\eta - x_\eta y_\xi \end{pmatrix} \quad (4.18)$$

In addition, for an arbitrary variable ϕ , central differences and backward differences are defined as

for central differences

$$\delta_\zeta \vec{\phi}_{i,j} = \frac{1}{2}(\vec{\phi}_{i+1,j} - \vec{\phi}_{i-1,j})$$

$$\delta_\eta \vec{\phi}_{i,j} = \frac{1}{2}(\vec{\phi}_{i,j+1} - \vec{\phi}_{i,j-1})$$

for backward differences

$$\nabla_\zeta \vec{\phi}_{i,j} = (\vec{\phi}_{i,j} - \vec{\phi}_{i,j-1})$$

The implicit dissipation terms are described as

$$\begin{aligned}
\frac{1}{2} \varepsilon_\eta (\Delta \nabla)_\eta \vec{\phi}_{i,j} &= \beta_{j+\frac{1}{2}} \vec{\phi}_{i,j+1} - (\beta_{j+\frac{1}{2}} + \beta_{j-\frac{1}{2}}) \vec{\phi}_{i,j} + \beta_{j-\frac{1}{2}} \vec{\phi}_{i,j-1} \\
\frac{1}{2} \varepsilon_\xi (\Delta \nabla)_\xi \vec{\phi}_{i,j} &= \lambda_{i+\frac{1}{2}} \vec{\phi}_{i+1,j} - (\lambda_{i+\frac{1}{2}} + \lambda_{i-\frac{1}{2}}) \vec{\phi}_{i,j} + \lambda_{i-\frac{1}{2}} \vec{\phi}_{i-1,j}
\end{aligned} \tag{4.19}$$

where

$$\begin{aligned}
\beta_{j\pm\frac{1}{2}} &= \sqrt{\beta_j \beta_{j\pm 1}} \\
\lambda_{i\pm\frac{1}{2}} &= \sqrt{\lambda_i \lambda_{i\pm 1}}
\end{aligned}$$

4.2. Cell volume specification

In this method, the cell volumes from one grid point to the next grid point for each level is prescribed simultaneously. One simple and popular way to specify the cell volumes suggested in reference [69] is

$$\Delta V_{i,j,k} = \Delta A_{i,j,k} \Delta s_{i,j,k} \tag{4.20}$$

where

$\Delta A_{i,j,k}$: the grid point surface area

$\Delta s_{i,j,k}$: the marching spacing

The marching distance, $\Delta s_{i,j,k}$ can be expressed as a function, which matches the required criteria for the generated grid. For different purposes, different functions can be used to specify the Δs . In general, it is obtained from the exponential function.

$$\Delta s_{i,j,k} = s_1 (1 + \varepsilon)^{k-1} \tag{4.21}$$

The values of s_1 (initial grid spacing in the marching direction and ε (the ratio of successive spacing in the marching direction) are the required parameters.

4.3. Boundary Conditions

In general five types of implicit boundary conditions can be incorporated in the three-dimensional code at the ξ and η boundaries [2]. As explained, the grids on the initial surface are defined in $i=1$ to i_{\max} and $j=1$ to j_{\max} , where i_{\max} and j_{\max} are the maximum indices for i and j .

Floating Edge Type of Boundary Condition that is used in the code does not allow for the specification of any boundary information such as edge shape or grid point distribution. Much as in the case of a constant Cartesian plane, an entire ξ and η boundaries can be floated using the simple hyperbolic equation $\vec{r}_{\xi\zeta} = 0$ or $\vec{r}_{\eta\zeta} = 0$ to update a boundary plane. This is essentially a zeroth order extrapolation of Δr from the adjacent interior value.

4.4. An Example

As an illustrative example, the grid around Lann Wing [71] is shown in Figure 4.1. Notice that Since floating type of boundary condition is used, the boundaries splay outward.

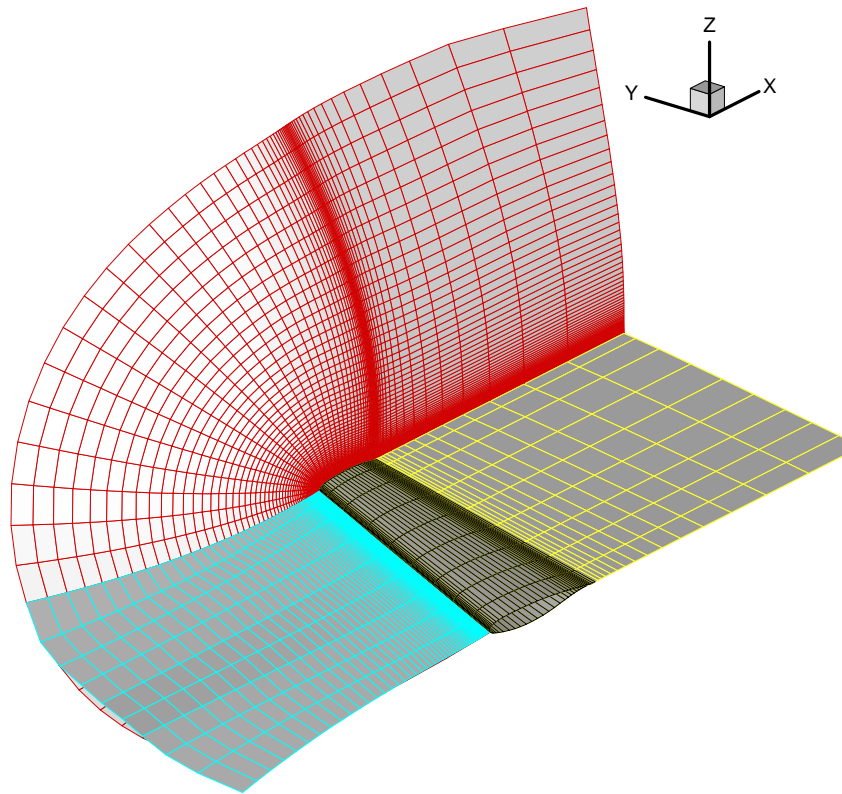


Figure 4.1 Illustrative example of grid around Lann Wing [71]

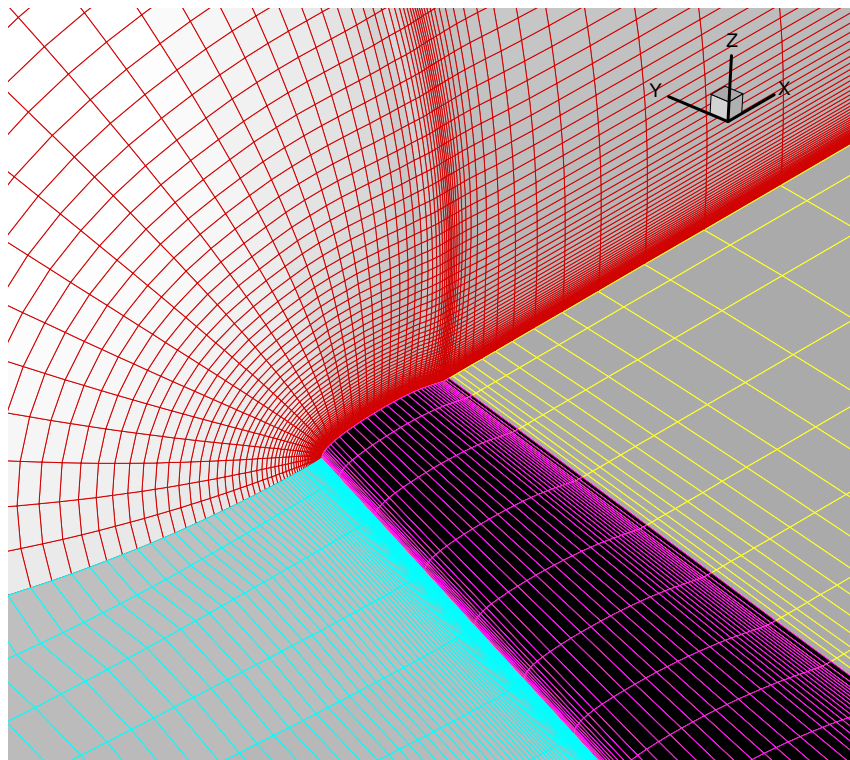


Figure 4.2 Zoomed view

CHAPTER 5

ADAPTED TURBULENCE MODELS

5.1. Baldwin-Lomax Turbulence Model

The Baldwin and Lomax turbulence model [72] is an algebraic eddy viscosity, zero equation model. The model is based on the mixing length hypothesis. The model has been widely used and tested, and remains a very popular turbulence model. Several advantages of the model are its simplicity in coding and the fact that it does not require the boundary layer edge thickness or edge velocity as an input parameter. The Baldwin and Lomax model works best in wall-bounded flows with favorable pressure gradients.

The calculation of eddy viscosity is not always straightforward and can lead to errors in the turbulence model if not computed correctly. As the flow physics become more complicated, as well as the geometry of the model being tested, the performance of this turbulence model greatly decreases.

The formulation is straightforward. It uses a two-layer algebraic equation to calculate the eddy viscosity term, μ_t given by

$$\mu_t = \begin{cases} (\mu_t)_{\text{inner}} & y \leq y_{\text{crossover}} \\ (\mu_t)_{\text{outer}} & y > y_{\text{crossover}} \end{cases} \quad (5.1)$$

where y is the normal distance from the wall and $y_{\text{crossover}}$ is the location along the constant index line where $(\mu_t)_{\text{inner}}$ exceeds $(\mu_t)_{\text{outer}}$, marching away from the wall.

For the inner region, μ_t is calculated as follows

$$\boxed{\mu_{t,inner} = \rho k^2 y^2 F_D^2 |\bar{\Omega}|} \quad (5.2)$$

where

$$|\bar{\Omega}| = |\bar{\nabla} \times \bar{V}|$$

$$F_D(y) = \left[1 - \exp\left(-y^+ / 26\right) \right]$$

$$y^+ = \frac{\sqrt{\rho_w \tau_w}}{\mu_w}$$

where subscript “w” denotes the “wall” quantities.

For the outer region, μ_t is calculated as follows.

$$\mu_{t,outer} = KC_{cp} \rho F_{wake} F_{kleb} \quad (5.3)$$

where

$$F_{wake} = \min \left[y_{\max} F_{\max}; C_{wk} y_{\max} u_{diff}^2 / F_{\max} \right]$$

$$F_{kleb} = \left[1 + 5.5 \left(\frac{C_{kleb} y}{y_{\max}} \right)^6 \right]^{-1}$$

$$u_{diff} = V_{\max} - V_{\min} \quad \text{where } V = (u^2 + v^2 + w^2)^{1/2}$$

$$K = 0.0168$$

$$C_{wk} = 0.25$$

$$C_{kleb} = 0.3$$

Exponential term and V_{\min} is set to zero except in wakes. The value F_{\max} is the maximum of the function $F(y)$ defined as

$$F(y) = y |\bar{\Omega}| F_D \quad (5.4)$$

and y_{\max} is the value where $F(y_{\max}) = F_{\max}$

5.2. Degani-Schiff Modification

For the flows around bodies, which experience cross flow separations, maximum value of $F(y)$ may be over predicted. This modification attempts to select the first occurrence of F_{max} in a search from the wall outwards [73] , since the function $F(y)$ exhibits more than one peak in such a flows. For example in the case of separated flows, the code must be forced to select the F_{max} in the boundary layer otherwise it may choose a length scale corresponding to the distance up to the rolling-up vortices, which can be larger. The symptoms of this type of occurrence may be stated as follows,

- Increase in the outer value of μ_t is too much,
- Details of the flow are distorted or washed out,
- Primary vortices are smaller,
- Primary separation is located closer to leeward symmetry plane,
- Secondary separation and vortices do not appear.

The code simply search and assigned the value of F_{max} until the following relation is satisfied

$$F < 0.9F_{\max} \quad (5.5)$$

5.3. Vorticity Adaptation

Often the vorticity from secondary sources is intermixed with the wall bounded flow, which causes the turbulence model to predict the value of "F" maximum incorrectly. This situation occurs with corner flows, flows with near wall vortices and with globally swirling flows. The Baldwin and Lomax model has been modified to calculate the "F" function based on directionally correct vorticity vectors that are vorticity vectors that are parallel to the local wall and perpendicular to the local velocity vector. This use of a reduced vorticity vector has been shown to produce dramatically improved prediction accuracy in some applications and has

not been known to reduce accuracy in any application [74]. Reduced vorticity is determined by the Equation (5.6).

$$\bar{\omega}_R = \frac{|\bar{\omega} \times \bar{V}|}{|\bar{V}|} \quad (5.6)$$

5.4. Algebraic Model for Vortical Flows

The turbulent viscosity values generated by the Baldwin-Lomax model are extremely sensitive to the vorticity profile above the wall. The new algorithm was added in order to compute the correct eddy viscosity in the vortex region, e.g. the side wind vortex. It determines the F_{max} based on the vortex core as illustrated in Figure 5.1.

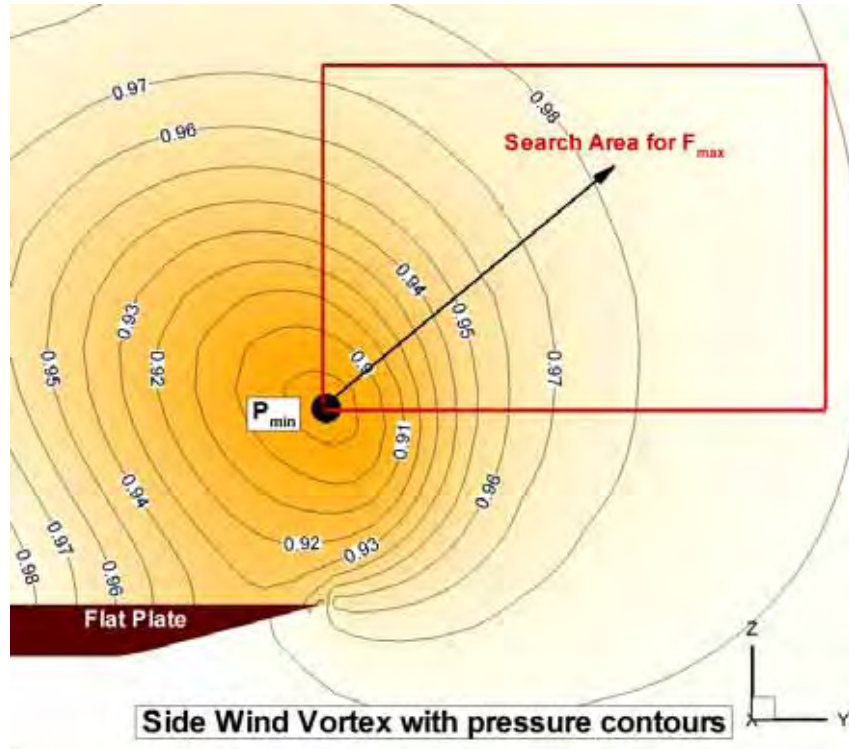


Figure 5.1 Illustrative example of side wind vortex with pressure contours

The code first seeks the minimum pressure point, which is actually the core of the vortex. Then it assigns this point as the starting point and search for F_{max} through the search area index by index.

5.5. Algebraic Wake Model

In order to use the simple algebraic models on block-structured grids, the problem arises how to calculate the turbulent stresses in those blocks that do not have a boundary layer- type flow, so that the model was corrected to catch up the wake region. A typical example is the wake of blunt bodies, because the algebraic models cannot calculate the characteristic length and the velocity scale normal to the wall. Therefore, empirical distribution laws were introduced to describe the turbulence transport into these blocks [75]. Because the production of turbulent energy in local equilibrium flows correlates with vorticity, this was taken as a weighted function to distribute eddy-viscosity in that area, according to

$$\mu_t' = \mu_{t_v} \left(\frac{|\omega|}{|\omega_v|} \right)^\alpha \quad (5.7)$$

with μ_{t_v} the maximum eddy-viscosity along the upstream block face and $|\omega_v|$ the local vorticity at that point. The exponent α is determined by numerical experiments, as $\alpha=0.2$ [75].

In addition, the eddy-viscosity is also smoothed by an exponential damping factor in order to ensure steadiness on the block faces.

$$\mu_t = \mu_t' - (\mu_t' - \mu_{t_j}) \exp\left(-\frac{\Delta x_j}{\Delta x_{\max}}\right) \quad (5.8)$$

where

μ_{tj} ; the eddy-viscosity on the upstream block face at the same j-station as μ_t'

Δx_j ; the normal distance to the location of μ_t'

Δx_{\max} ; the length of the block in streamwise direction

CHAPTER 6

TEST CASES AND RESULTS

In this chapter, test cases will be covered in two main sections, namely two dimensional test cases and three dimensional test cases respectively. Results of each test case are presented in the corresponding section.

6.1. Two Dimensional Test Cases

Two dimensional test cases are chosen to validate the Navier-Stokes solver and to investigate the essential grid parameters for the solution of three dimensional test cases.

6.1.1. Laminar Flat Plate

A grid convergence study of the PML3D code, for the solution of laminar flow over a flat plate at zero incidence angle, is performed. Comparisons are made between the computational results and the analytical solution, which is the well known “The classical Blasius similarity solution”, that provides data for comparison. Various textbooks discuss this solution [77],[81]. The Reynolds number based on the free stream velocity at distance from the plate leading edge, ranged from zero to 2×10^6 . The Reynolds number, Re_L is equal to 1×10^6 at $x/L=1.0$. Three different grids are produced and the effects of the grid on the accuracy of the solution are observed. Number of iterations needed for a steady converged solution is also investigated. For the numerical solution, The Mach number of the flow is selected as Mach 0.4. On the other hand is

known that the Blasius solution is based on incompressible flow assumption. When comparing the numerical and analytical results, it is assumed that compressibility effects are negligible for a boundary layer flow at Mach=0.4. A laminar boundary layer develops on the plate and thickens along the plate. The leading edge of flat plate is located at coordinates $(x/c=0, y/c=0)$.

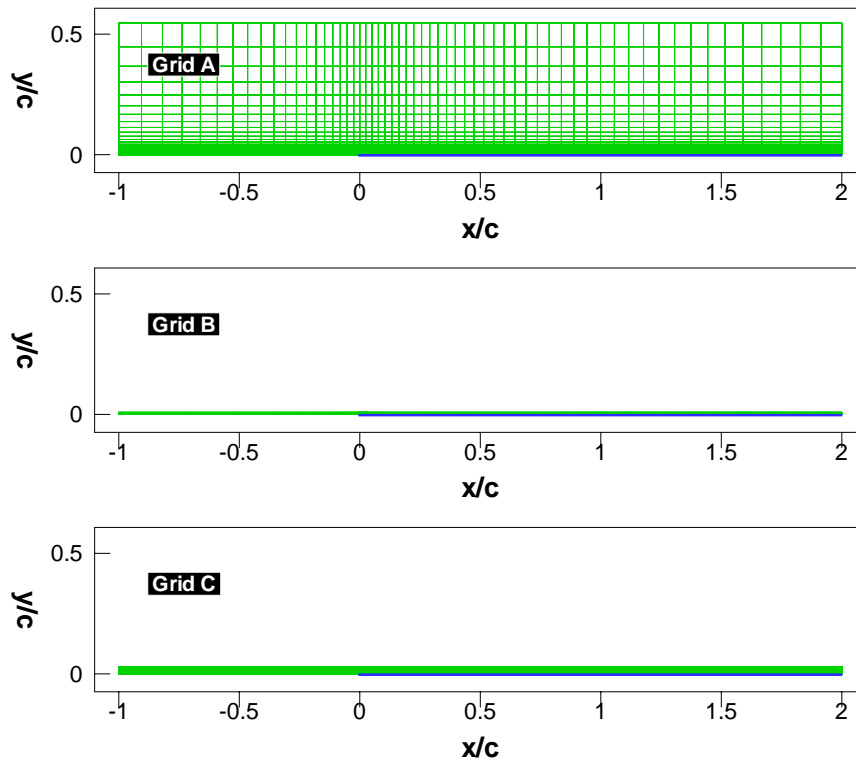


Figure 6.1 The applied grid geometries

6.1.1.1. Computational Grid and Initial Conditions

Single-block, two-dimensional, structured grids are generated for the flow domain. There different grid configurations are used. The grid geometries with actual dimensions (x/y aspect ratio = 1.0) are shown in Figure 6.1 The grid parameters are shown in Table 6.1

Table 6.1 The grids used in the Computations

Grid	Initial Grid Spacing	Density	Maximum Marching Distance
A	6.25 E-5	60 x 80	0.545
B	1.0 E-5	160 x 60	0.008
C	1.0 E-5	160 x 130	0.03

In the grid configuration A, total of 4800 points were used as shown in Figure 6.2. In the streamwise direction, 39 grid points were used along the flat plate with the leading edge stretching. In the normal direction, two different distribution were used; first 40 points were distributed uniformly between plate surface and $y/c = 0.0025$ and then stretched by tangent hyperbolic method. Initial grid spacing was set to $\Delta y/c = 6.25 \times 10^{-5}$.

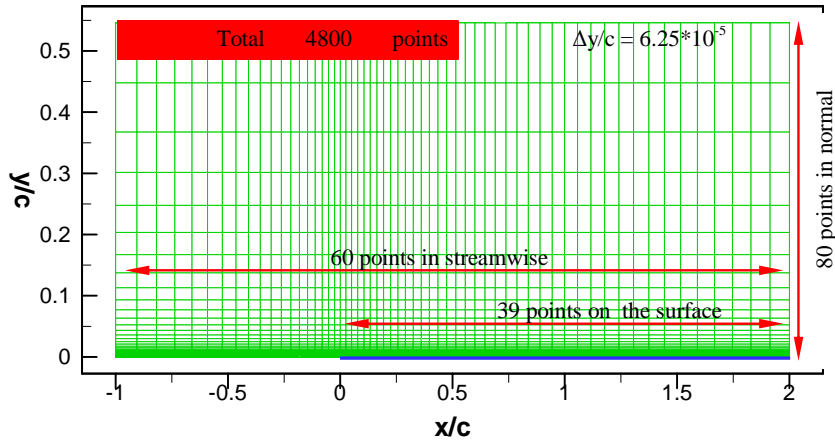


Figure 6.2 The grid configuration A

In the grid configuration B, total of 9600 points were used as shown in Figure 6.3. In the streamwise direction, 139 grid points were used along the flat plate with leading edge stretching. In the normal

direction, two different distribution were used again; first 40 points were distributed by tangent hyperbolic stretching between plate surface and $y/c = 0.0025$ and then stretched uniformly. Initial grid spacing was preselected as $\Delta y/c = 1.0 \cdot 10^{-5}$.

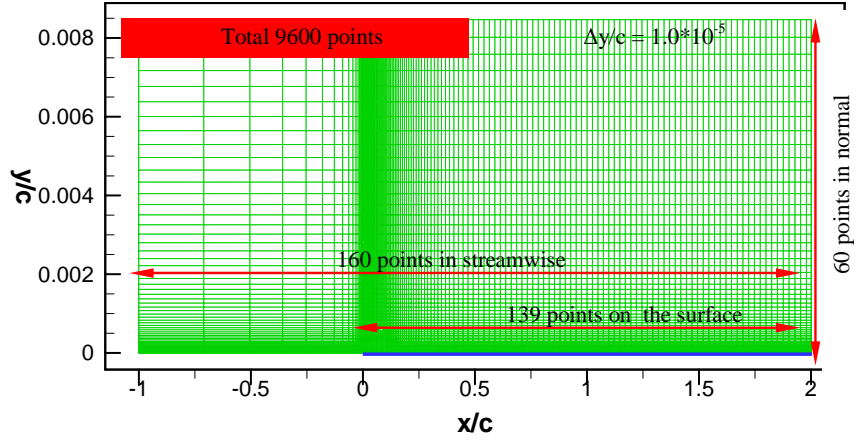


Figure 6.3. Grid configuration B

In the grid configuration C, total of 20800 points were used as shown in Figure 6.4. In the streamwise direction, 139 grid points were used again along the flat plate with leading edge stretching. In the normal direction, first 65 points were distributed by tangent hyperbolic stretching between plate surface and $y/c = 0.0025$ and then stretched in the same manner. Initial grid spacing was preselected as $\Delta y/c = 1.0 \cdot 10^{-5}$.

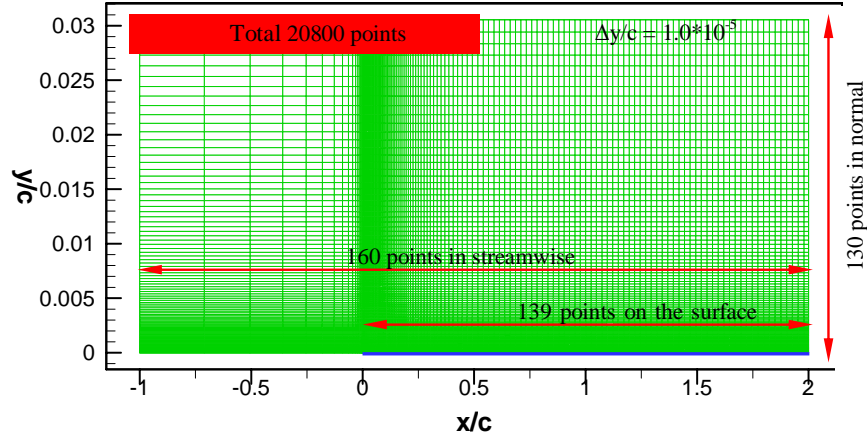


Figure 6.4. Grid configuration C

6.1.1.2. Boundary Conditions

At the flat plate surface, the no-slip condition applies. The inflow boundary of the computational domain is a subsonic inflow boundary and is placed upstream of the leading edge at $x/c = -1$ so as to capture the leading edge flow. The outflow boundary is placed at the end of the plate at $x/c = 2.0$. The farfield flow beyond the boundary layer should remain fairly uniform at freestream conditions. The farfield boundary is placed according to the applied grid configuration.

Table 6.2 Computational details

Grid	CPU time (minute)	Memory Requirement (Mb)	Number of Points	Number of Iterations
<i>A</i>	91	7388	4800	40000
<i>B</i>	190	9416	9600	40000
<i>C</i>	1380	16000	20800	100000

6.1.1.3. Computational Studies

The computation starts from the freestream solution and marches in time using local time-stepping until the L2 residual has leveled off. A constant CFL number of 30 is used. The steady-state flow was computed for each grid.

For the grid configurations A and B, 40000 iteration steps were required for a steady-state solution. However, the case belonging to the grid configuration C converged fully at 100000 iterations. Computations are performed on P4 1500 MHz single processor workstation. The computational details are given in Table 6.2.

6.1.1.4. Convergence History

In Figure 6.5, the convergence history for all cases is shown in terms of L2 Residual. For the first two cases, although the solution was converged after the 40000 iteration steps, L2 norm continues to drop. . From that figure, it can be seen that, after 70000 iterations, the solution with Grid A has converged 18 orders of magnitude, the solution with Grid B has converged 6.5 orders of magnitude, and the solution with the Grid C after 100000 iterations has converged 4.5 orders of magnitude. In normal conditions, three orders of magnitude convergence is accepted to be sufficient for a converged solution.

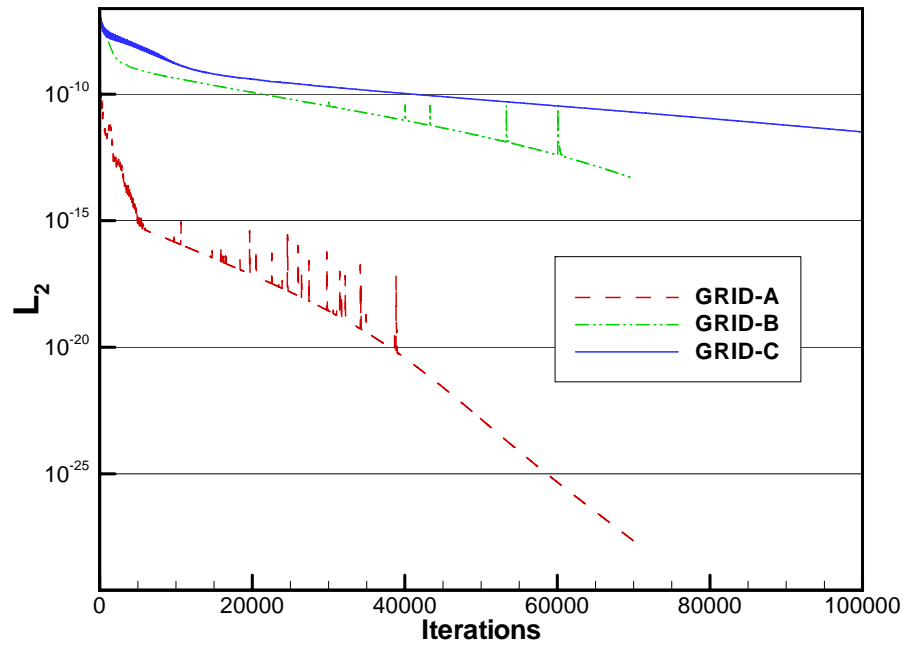


Figure 6.5 Convergence history, L_2 Norm of Residue

Table 6.3 Blasius solution [77].

Skin Friction Coefficient	$c_f = \frac{0.664}{Re_x^{1/2}}$
Boundary Layer Thickness	$\frac{\delta}{x} = \frac{5}{Re_x^{1/2}}$
Displacement Thickness	$\frac{\delta^*}{x} = \frac{1.721}{Re_x^{1/2}}$
Momentum Thickness	$\frac{\theta}{x} = \frac{0.664}{Re_x^{1/2}}$
Shape Parameter	$H = \frac{\delta^*}{\theta} = 2.59$

6.1.1.5. Comparisons of the results

The computed flow properties such as pressure coefficient, skin friction coefficient, boundary layer thickness, momentum thickness, shape factor etc. are compared to the analytic results of Blasius [77] shown in Table 6.3 to establish the validity of the computed results.

The difference in the flow domain especially the boundary layer explicitly shows the validity and the accuracy of the applied grids. These are shown in Figure 6.6, Figure 6.7 and Figure 6.8 for each case with an exaggerated view such that the dependency between the axes is temporarily removed. Notice that the number of points that were placed on the flat plate surface in the normal direction at various locations lying on the boundary layer. For the Grid A and B, picture seems to be the same but the results shows that the number of points in the streamwise direction has an important role about the accuracy of the problem. Moreover, they have too small number of points for the first quarter of the flat plate. Hence, the Grid C seems to be capable of capturing the flow properties through the boundary layer.

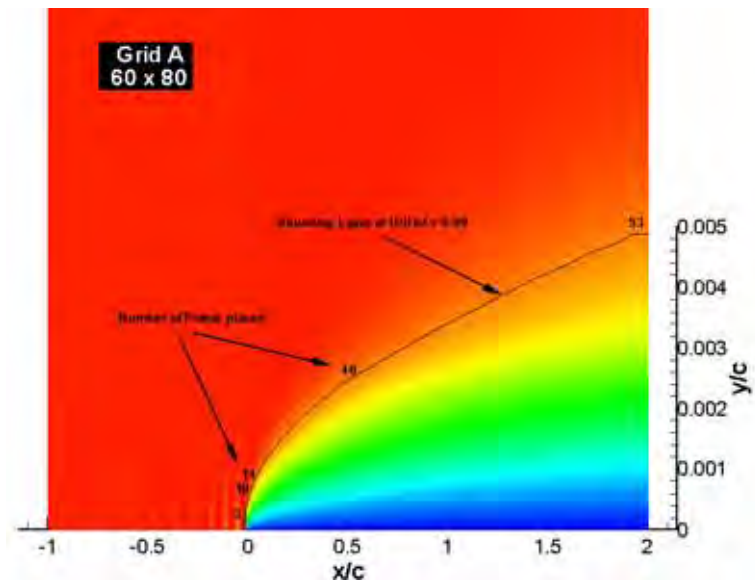


Figure 6.6 The boundary layer for grid A

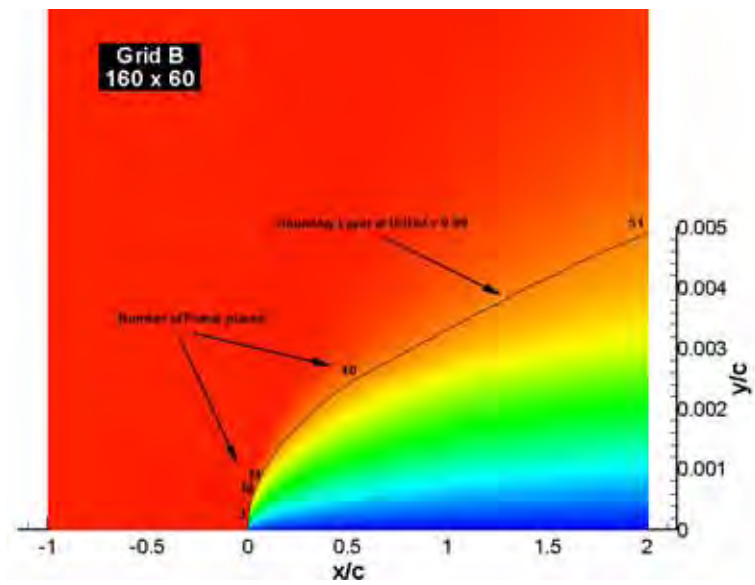


Figure 6.7 Boundary layer for grid B

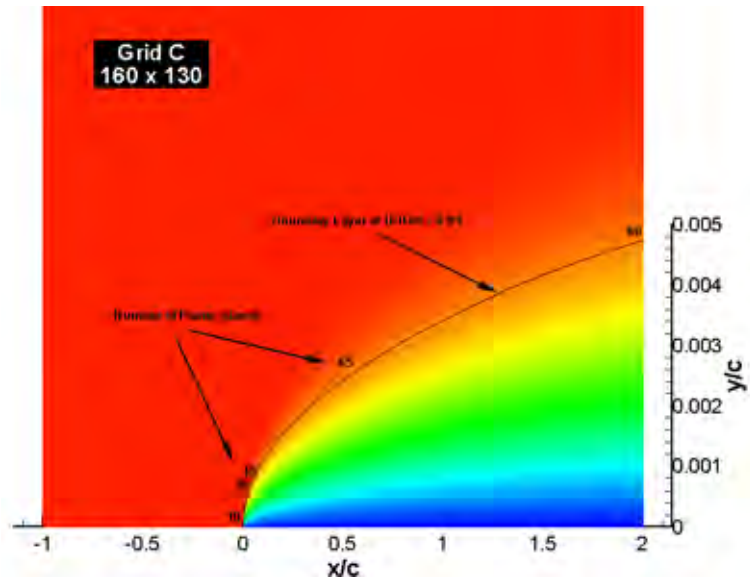


Figure 6.8 Boundary layer for grid C

The following figures show the comparison of the computational and analytic results of the selected variables. The computational results are taken from the fully converged solutions of each case.

Figure 6.9, Figure 6.10 and Figure 6.11 shows the iterative convergence of the parameter C_f for each grid respectively. The results in these figures have belonging to the conditions at 70000 iterations for A and B type Grids and 100000 iterations for C type Grids.

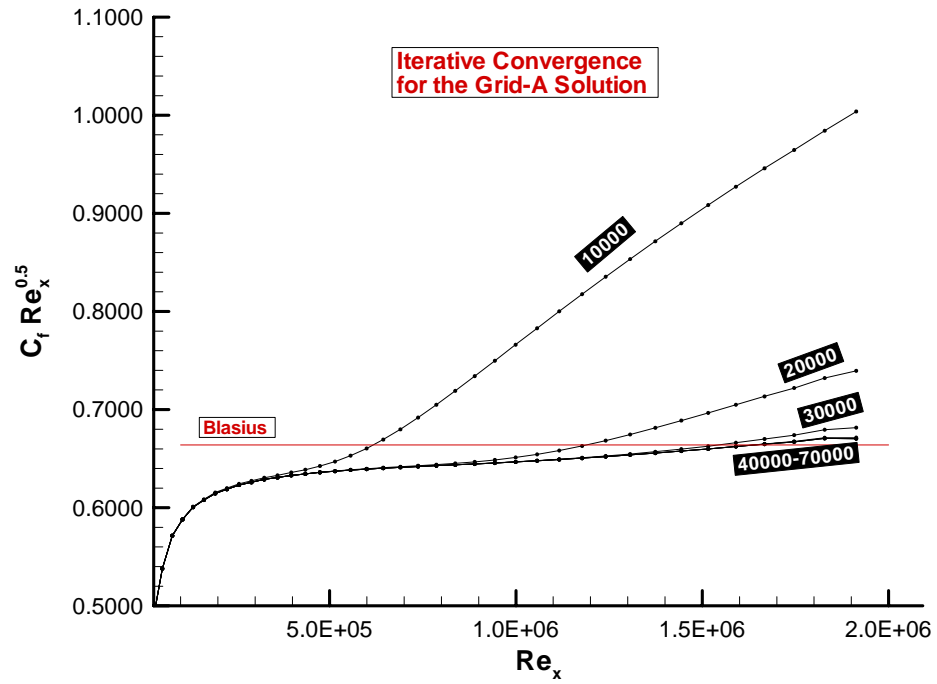


Figure 6.9 Iterative convergence of the grid-A solution

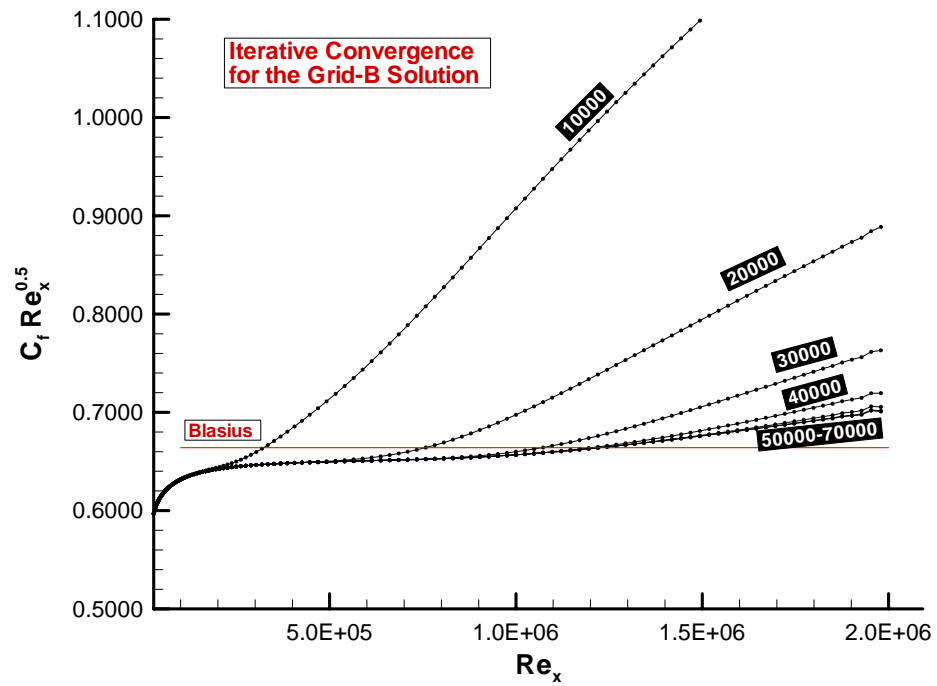


Figure 6.10 Iterative convergence of the grid-B solution

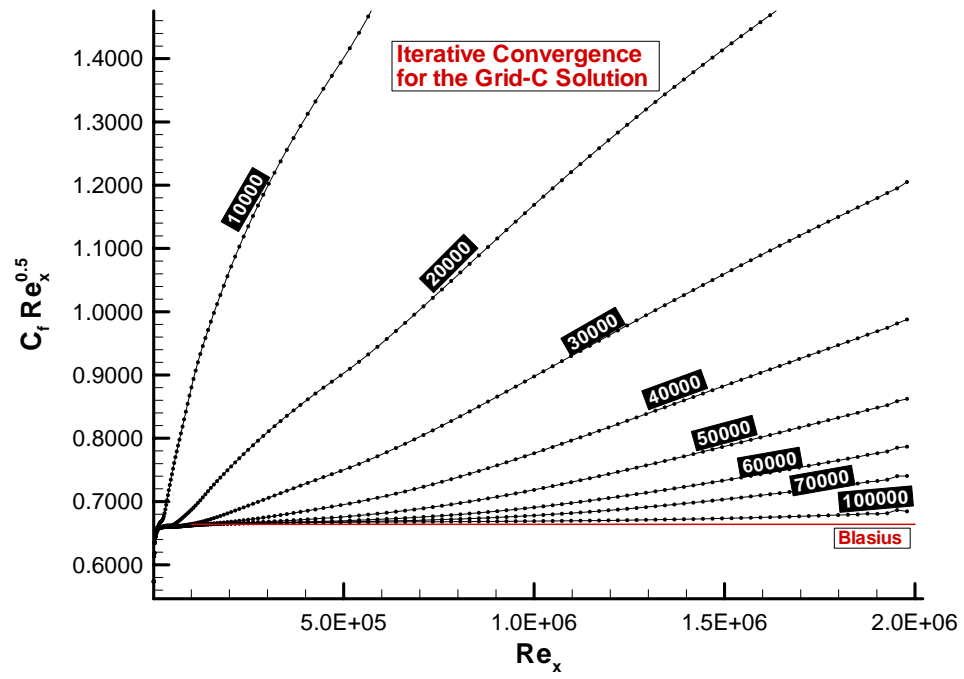


Figure 6.11 Iterative convergence of the grid-C solution

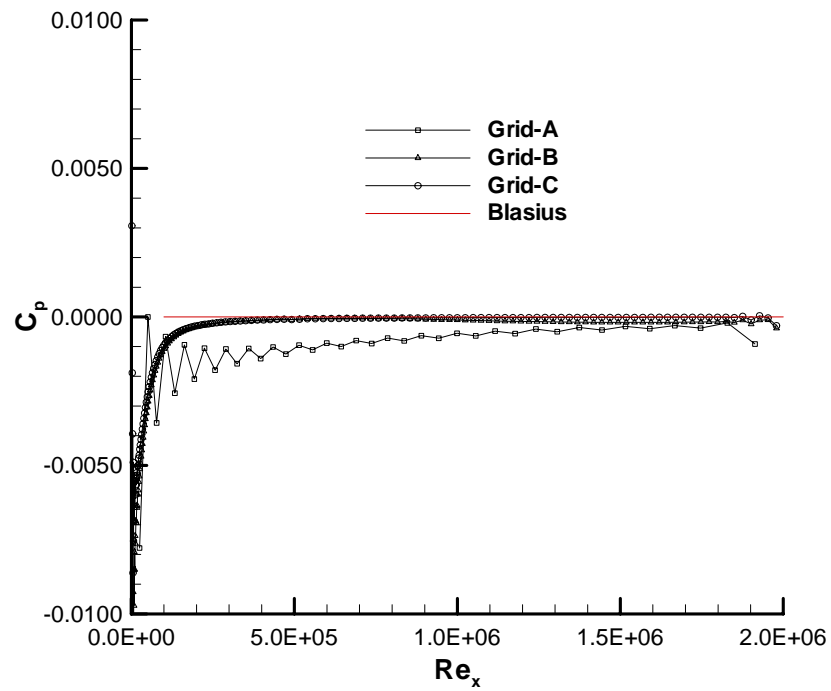


Figure 6.12 Pressure coefficient comparison

Figure 6.12 shows the variation of the pressure coefficient on the flat plate. As already known, the Blasius solution assumes that C_p is zero at the leading edge of the flat plate. In reality, however, the pressure becomes negative near the leading edge because the leading edge is the stagnation point and afterwards, the flow is inclined and speeds up in downstream region by the effect of the boundary layer displacement thickness. Hence, Navier stokes solution of the boundary layer preserves the actual sate of the flow. As seen on that figure, A- type Grid gives inappropriate results due to the rough density of grid in the streamwise direction in comparison with the others.

In Figure 6.13 , the skin friction coefficient, which is the one of the most important flow parameters from the engineering point of view, is displayed. It is seen that the Grid C is the most proper grid configuration, which has more grid density near the surface.

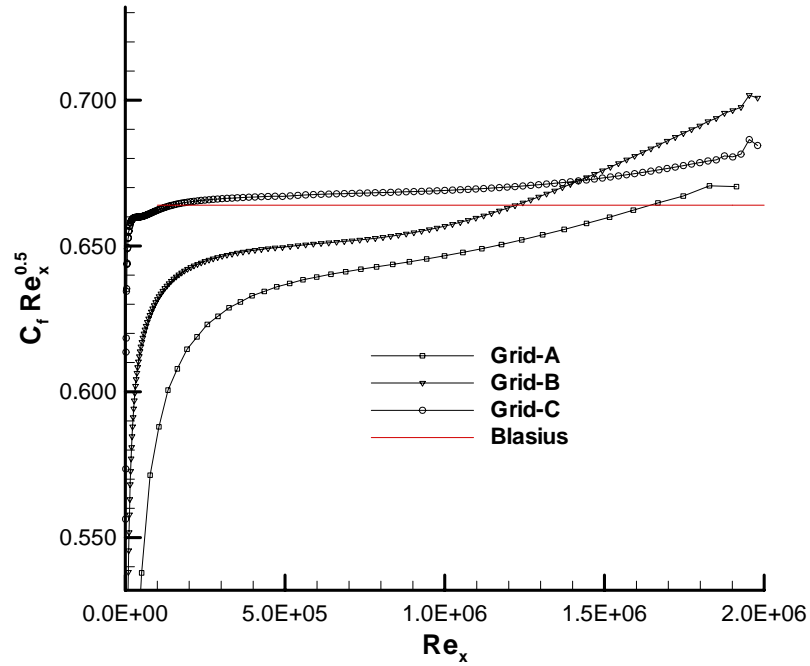


Figure 6.13 Skin friction coefficient comparison

Results of the boundary layer thickness parameters are shown in Figure 6.14, Figure 6.15, and Figure 6.16. The computed boundary layer thickness δ is defined as the distance from the plate where $u = 0.99 \times u_{\max}$, where u_{\max} is the value at the first maximum in the u profile. The momentum and displacement thicknesses were computed from the standard 2-D planar definitions.

$$\delta^* = \int_0^{y_m} \left(1 - \frac{u}{u_\infty}\right) dy \quad (6.1)$$

$$\theta = \int_0^{y_m} \frac{\rho u}{\rho_\infty u_\infty} \left(1 - \frac{u}{u_\infty}\right) dy \quad (6.2)$$

where y_m is the distance from the plate to the first maximum in u . Simpson's rule was used for the numerical integration. The shape factor is simply defined as $H = \delta^* / \theta$.

In order to detect the thickness parameters correctly, the grid density must be sufficient in either directions, streamwise and normal, especially in the boundary layer region. Coarse grids around the boundary layer edge may lead to weak prediction of boundary layer thickness. The grid C, which has more grid points in both direction, correctly detects the parameters involved. The boundary layer shape parameter, H , is presented in Figure 6.17.

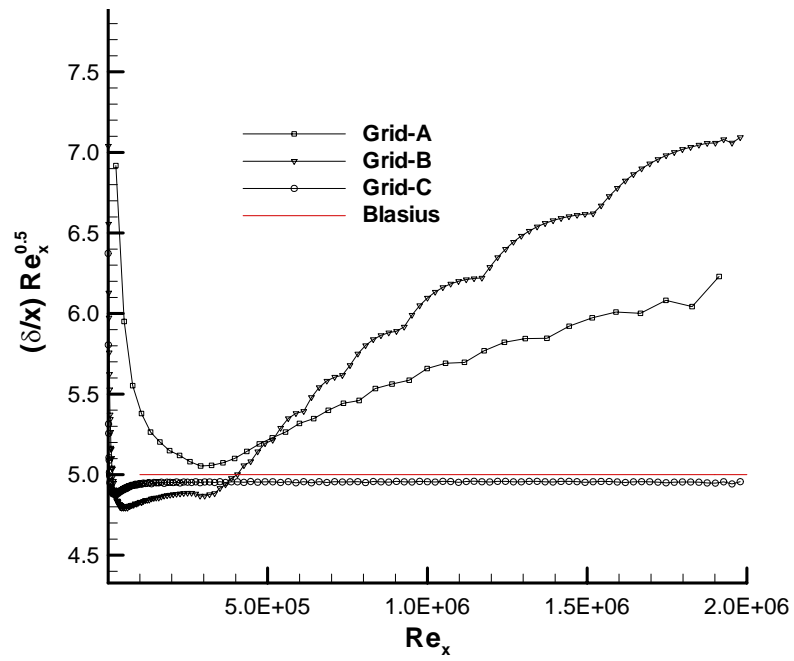


Figure 6.14 Boundary layer thickness comparison

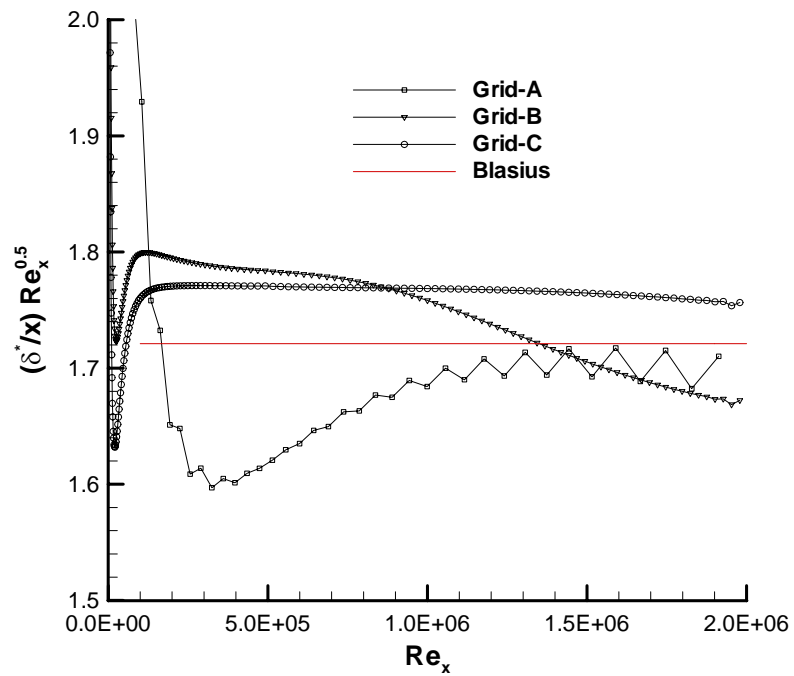


Figure 6.15 Displacement thickness comparison

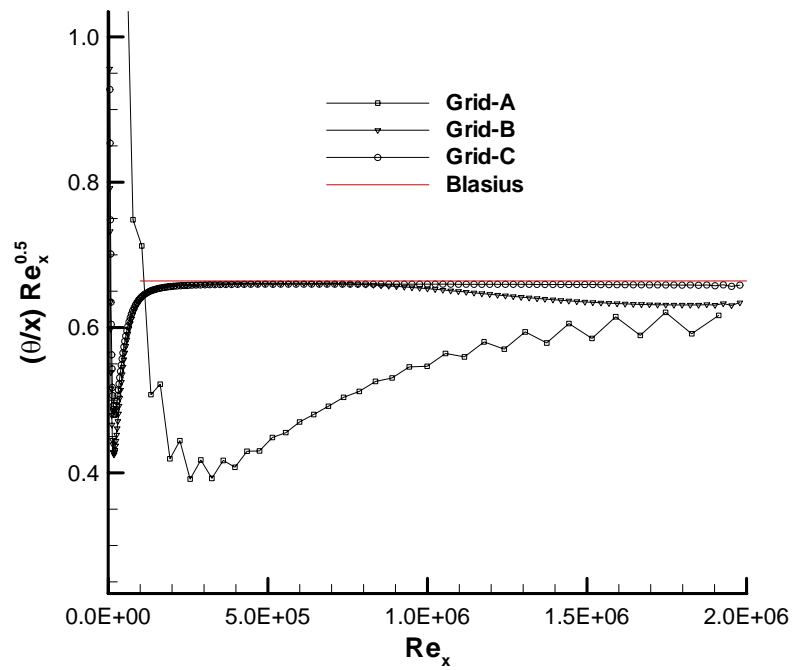


Figure 6.16 Momentum thickness comparison

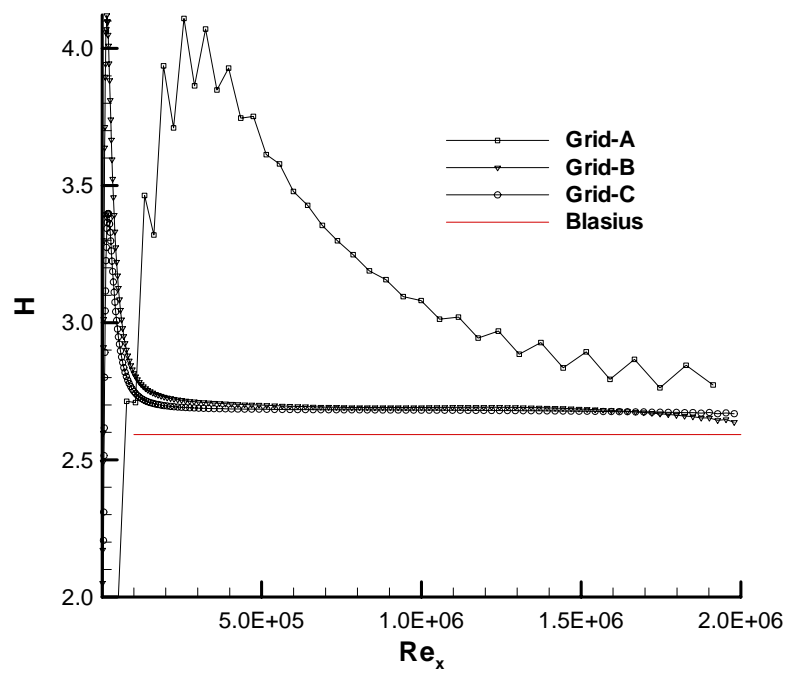


Figure 6.17 Shape parameter comparison

In this study, the grid effects were investigated on the Navier-Stokes solution of the boundary layer. It was seen that the solution was effected by the following parameters; the grid density of the boundary layer in the normal direction to the flow, the minimum grid spacing and the grid density in the streamwise direction. By using less dense grid in the solution, it is seen that L2 residual is decreasing steeply but converging to the less accurate results. On the other hand, in the case of using more dense grid in appropriate regions, L2 residual is decreasing slowly but converging to the more accurate results. In addition, it is understood that the flow solver, which is specifically coded for compressible flows, converges slowly for low speed viscous flows but can give accurate results when a proper grid is used.

6.1.2. Turbulent Flat Plate

Turbulent flow over a flat plate at zero incidence was investigated. Compressibility effects are neglected during study so that the results are compared with the incompressible experimental data. The Reynolds number, Re_L is equal to 1×10^7 . The Reynolds number based on the free stream velocity at distance from the plate leading edge, ranged from zero to 2×10^7 .

6.1.2.1. Computational Grid and Initial Conditions

The computational mesh was generated by using hyperbolic grid generation code [76]. Grid points in the streamwise direction were packed near the leading edge with a total number of points 160 and 140 of them are distributed along the flat plate.

At the normal direction, 96 points were used with 71 points in the boundary layer. The boundary layer thickness was estimated as follows [77].

$$\delta = \frac{0.38x}{Re_x^{1/5}} \quad (6.3)$$

Marching distance was arranged as to follow the boundary layer thickness along the flat plate using a Roberts's transformation [78]. With this transformation, for a line of length D, points are packed near the beginning of the line.

The distance between solid wall and the first grid point was prescribed as follows. At least one grid point was placed where y^+ was equal to 1.0. Pre-studies showed that for a mesh that follows the boundary layer, the right place of y^+ analysis was the trailing edge of the plate, or the exit plane. If at least one grid point was placed where y^+ was equal to 1.0 at that region, then it was guaranteed that there is more grid point at the leading edge region where y^+ was equal to 1.0.

y^+ analysis is conducted by using the following equation,

$$y^+ = \left(\frac{y}{c}\right) \sqrt{\frac{c_f}{2}} Re_L \quad (6.4)$$

where c_f is the skin friction coefficient and Re_L is the Reynolds number.

The value of c_f was estimated through the Schoenherr formula [77] as follows:

$$\frac{1}{\sqrt{c_f}} = 4.15 \log(Re_x c_f) + 1.7 \quad (6.5)$$

For our case, Re_x was 2×10^7 at exit section of the plate. Then according to the above formula, c_f was found to be 0.002264. By Equation (6.5), the minimum value of y/c was then found to be 2.972×10^{-6} . For the outer region expect from boundary layer, the points were stretched geometrically until the upper computational boundary was at approximately, $y_{\%} = 7\delta$. As a result, the value of y^+ at the first grid point was estimated as ranging from about 0.2 near the leading edge of the plate, to about 1.0 at the exit plane.

The resulting grid, scaled to fit is shown in Figure 6.18. The edge of the boundary layer, as predicted by equation 2, is shown as a thick/black line. Figure 6.19 shows the grid with no scaling. In addition, zoomed view at the beginning of the boundary layer slope is shown in Figure 6.20.

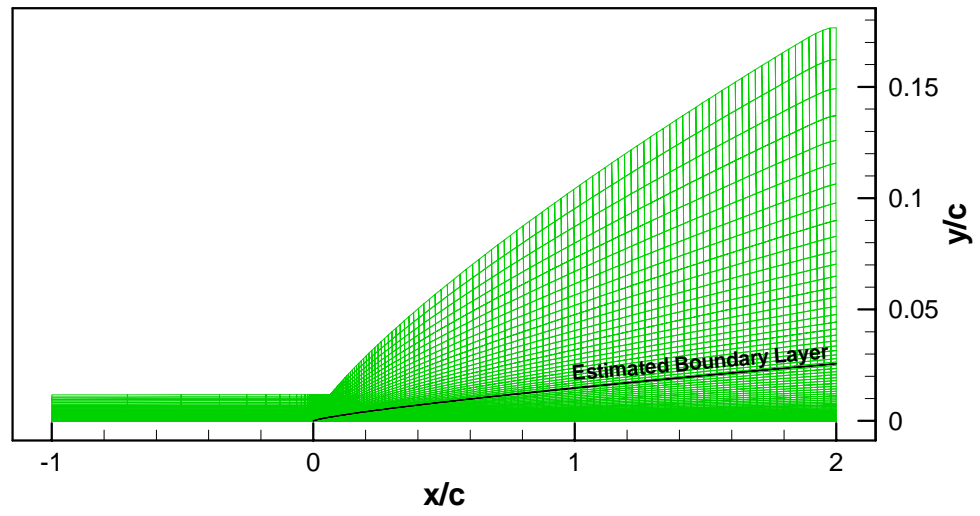


Figure 6.18. Grid geometry

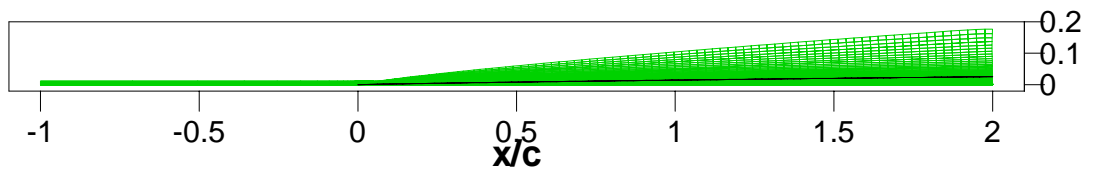


Figure 6.19. Grid geometry in actual dimensions

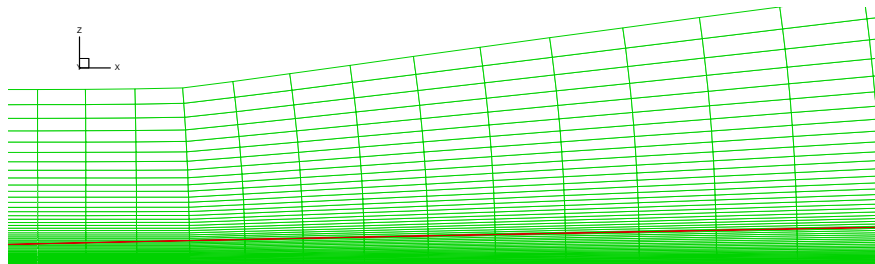


Figure 6.20. Zoomed view of the grid about $x/c=0.0$

6.1.2.2. Boundary Conditions

Five boundary segments were used: (1) the upstream inflow boundary; (2) the downstream outflow boundary; (3) the symmetry plane on the lower boundary upstream of the plate; (4) the flat plate itself; and (5) the upper free stream boundary. The boundary conditions used are summarized in the following table.

Table 6.4. Boundary conditions

Boundary	j	k	condition
Upstream Inflow	1	2-95	<i>Fixed conditions</i>
Downstream Outflow	160	2-95	<i>Extrapolation</i>
Symmetry Plane	1-19	1	<i>Symmetry</i>
Flat Plate	20-160	1	<i>No-slip</i>
Upper Free Stream	1-160	96	<i>Extrapolation</i>

6.1.2.3. Computational History

The computation starts from the freestream solution and marches in time using local time-stepping until the L_2 residual has leveled off. A constant CFL number 20 is used. Computations are performed on P4 2.66 GHz single processor workstation. The computational details are given in Table 6.5.

Table 6.5 Computational details

CPU time (minute/10000 iterations)	Memory Requirement (MB)	Number of points	Number of iterations
82	16300	160x96	125000

6.1.2.4. Convergence History

The convergence history of the L_2 Norm of the residual is shown in Figure 6.21.

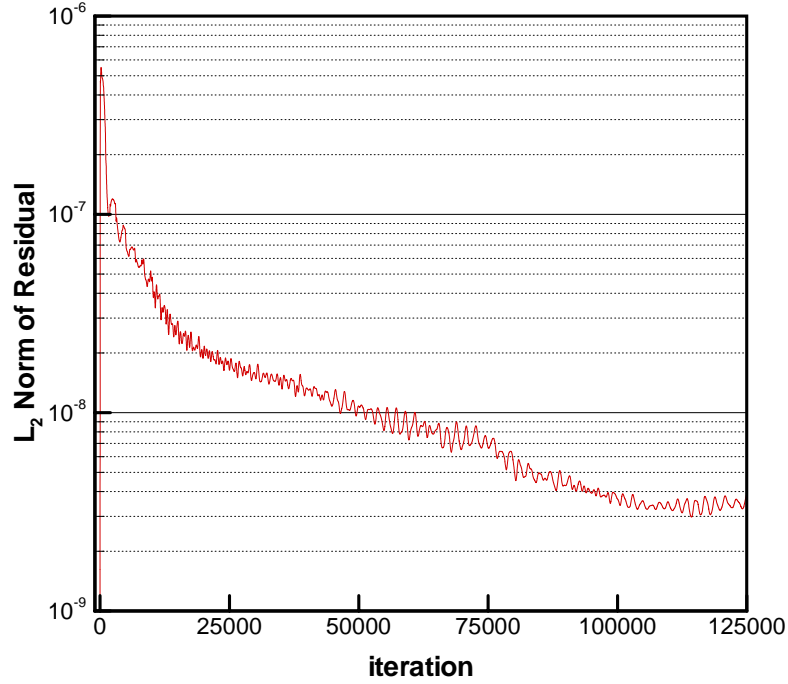


Figure 6.21. Convergence history

6.1.2.5. Computed Results

i. Velocity profiles

The computed velocity profiles are compared with the experimental data of Wieghardt [78] in Figure 6.22, Figure 6.23 and Figure 6.24. The computational results are shown at stations, $x/c=0.1, 1.0, 2.0$ which correspond to $Re_x=0.1 \times 10^7, 1.0 \times 10^7, 2.0 \times 10^7$ respectively. The experimental data shown in figures are at the experimental stations closest to these computational locations. Actual locations of the experimental data in those figures are $Re_x=0.106 \times 10^7, 1.027 \times 10^7$.

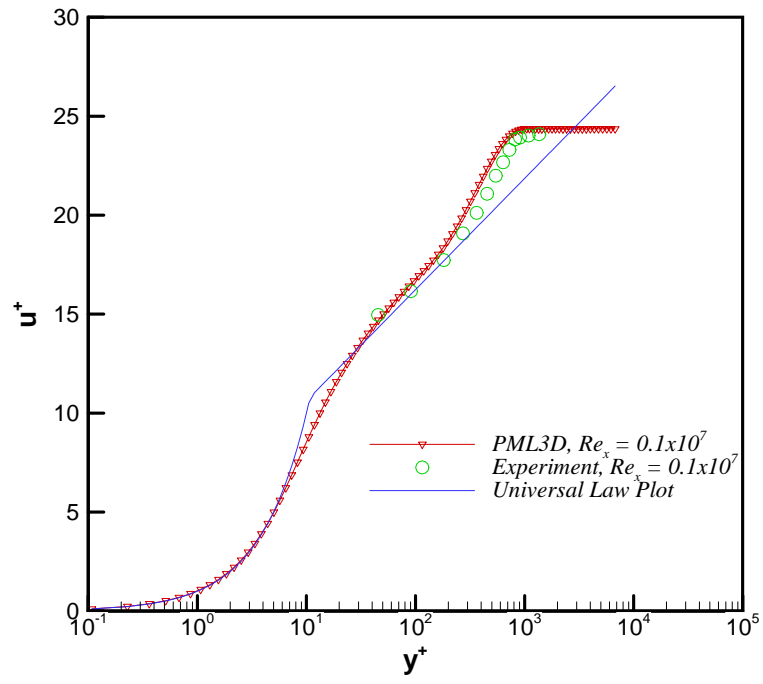


Figure 6.22. Velocity profile at $x/c = 0.1$

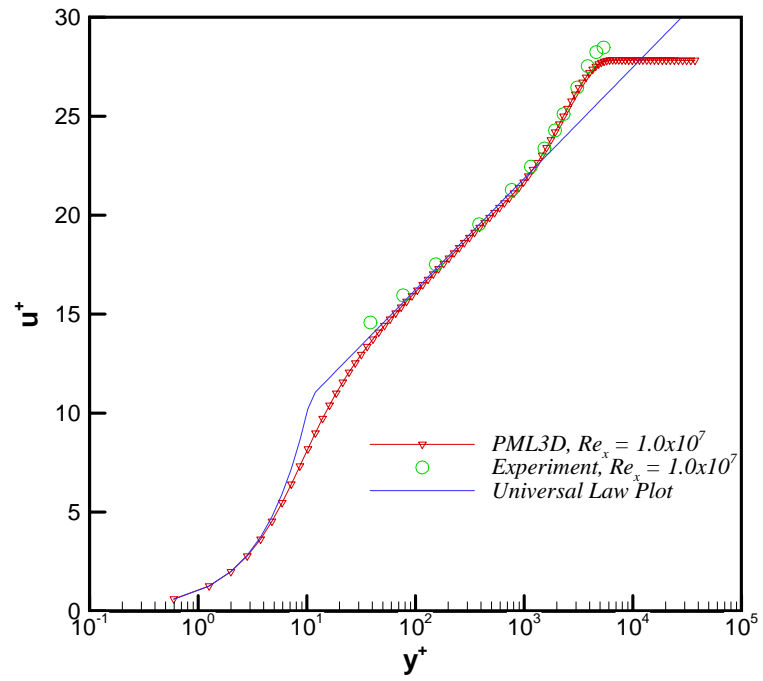


Figure 6.23. Velocity profile at $x/c = 1.0$

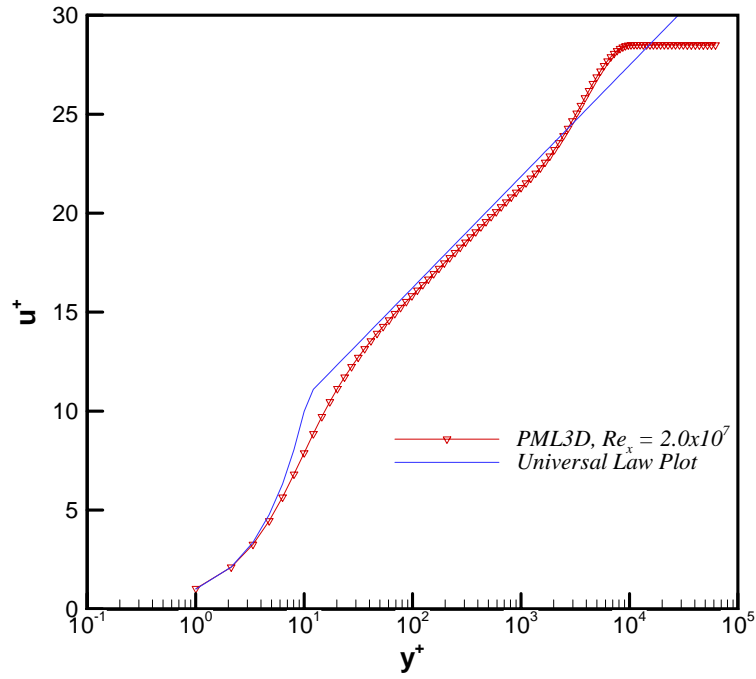


Figure 6.24. Velocity profile at $x/c = 2.0$

ii. Thickness Parameters

In Figure 6.25 through Figure 6.28, computed values of boundary layer thickness δ , momentum thickness θ , displacement thickness δ^* , and shape factor H , respectively are compared with the correlation values based on simple power-law analyses [77], [81].

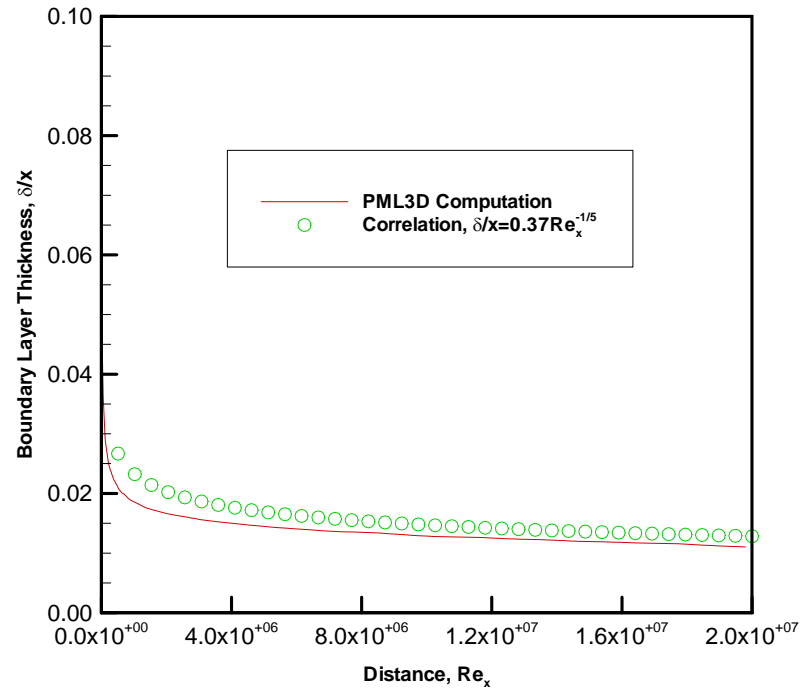


Figure 6.25. Boundary layer thickness

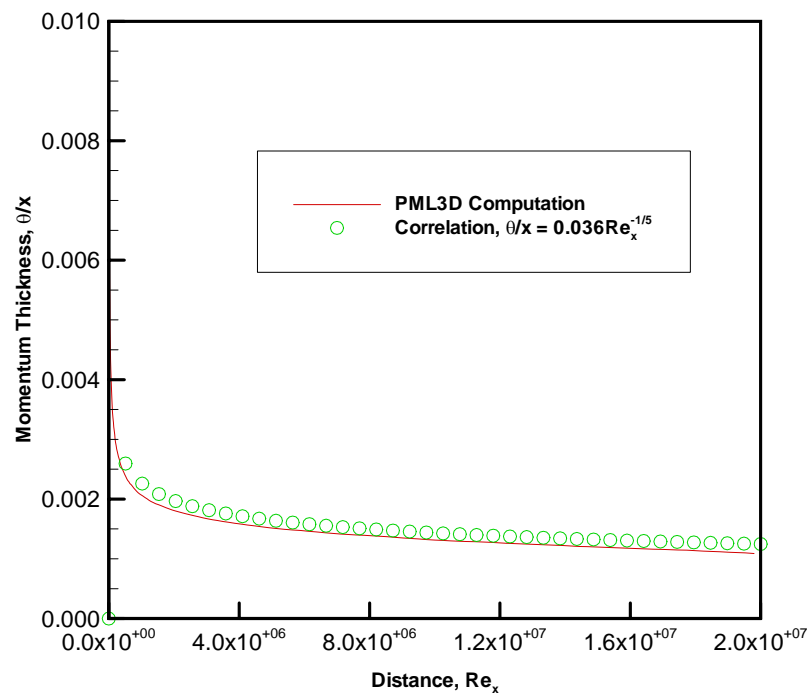


Figure 6.26. Momentum thickness

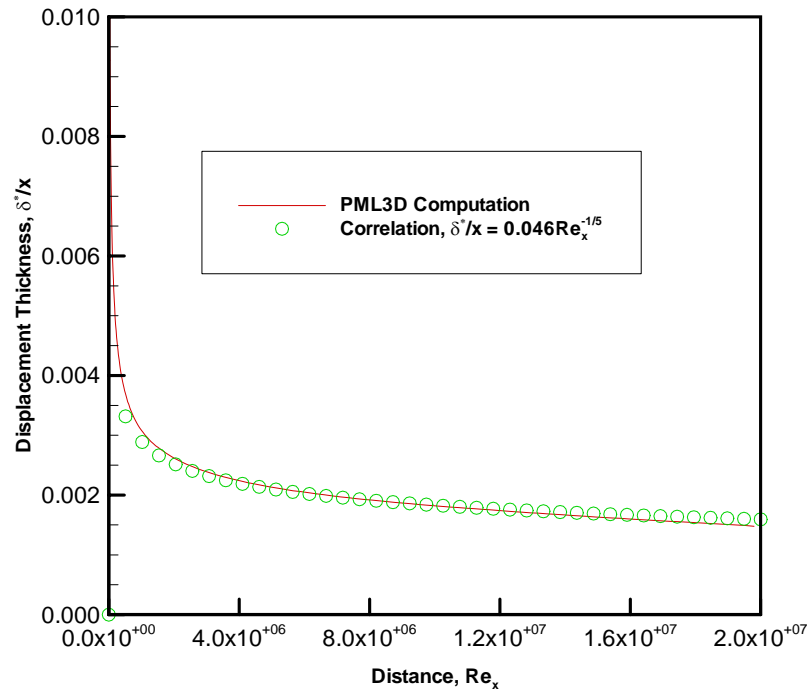


Figure 6.27. Displacement thickness

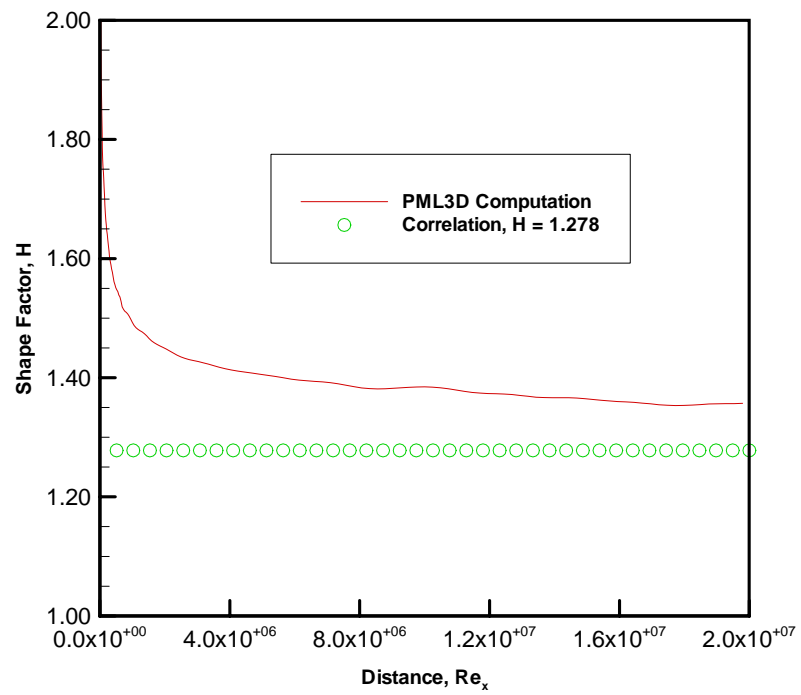


Figure 6.28. Shape factor

iii. Skin Friction

The computed skin friction coefficient is compared with values from two different correlation formulas [77], [81] in Figure 6.29.

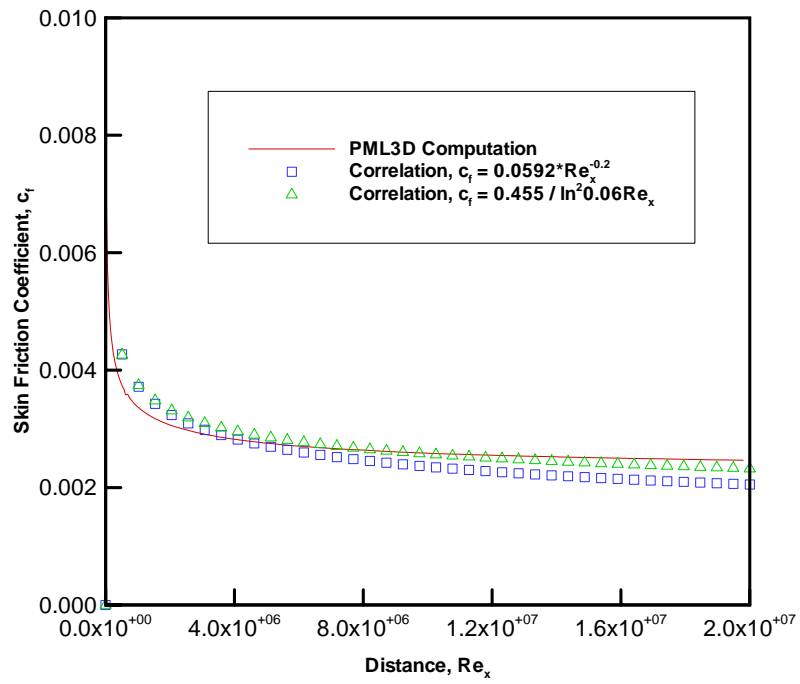


Figure 6.29. Skin friction coefficient

6.2. Three Dimensional Flat Plate

6.2.1. Problem Description

For the present computational study, an aspect ratio 1.0 flat plate with small thickness and sharp edges is considered as the test model. The computational test matrix given in Table 6.6 is constructed according to the experiment data [39]. The cases P1-P4 are intended for pressure comparisons and the cases S1, S2 are intended for surface streamline comparisons with experiments.

Table 6.6 Computational test matrix

CASE	M_{∞}	Re_{∞}	α (deg)
P1	0.54	$3.0 \cdot 10^5$	7.5
P2	0.55	$3.0 \cdot 10^5$	13.5
P3	0.87	$3.0 \cdot 10^5$	7.5
P4	0.85	$3.0 \cdot 10^5$	13.5
S1	0.42	$1.65 \cdot 10^5$	5.0
S2	0.42	$1.65 \cdot 10^5$	15.0

The flow domain is composed of two zones namely Block-1 and Block-2 as seen on Figure 6.31. According to the researchers in high angle of attack aerodynamics [2], [3], vortex asymmetry begins when the angle of attack is about twice the nose angle. As a rough estimate, it is may be

guaranteed that vortex asymmetry does not exist until the angle of attack is about 23 degree. In our test cases, the nose angle is 15 degree and the angle of attack varies from 5° to 15° . Moreover, the experiments [39] about our test cases report that the flow is symmetric. Hence, we can consider that the flow field is symmetric with respect to the xz plane, and then apply the computation over only the half of the flat plate.

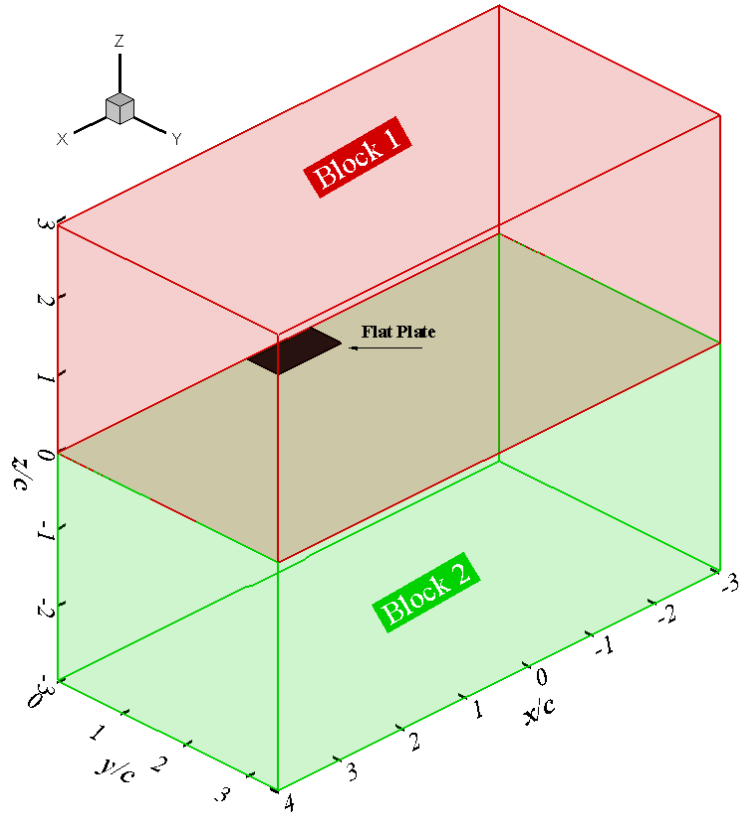


Figure 6.30 Computational flow domain

The first zone is above the flat plate and extends in the range of $-3.0 \leq x/c \leq 4.0$, $0.0 \leq y/c \leq 3.5$ and $0.0 \leq z/c \leq 3.0$. The second zone is below the flat plate and extends in the range of $-3.0 \leq x/c \leq 4.0$, $0.0 \leq y/c \leq 3.5$ and $-3.0 \leq z/c \leq 0.0$. The flat plate lies in the $z = 0.0$ plane

and it extends in the range of $0.0 \leq x/c \leq 1.0$ and $0.0 \leq y/c \leq 0.5$. The flat plate has a three dimensional geometry, which has four sharp edges as shown in Figure 6.31.

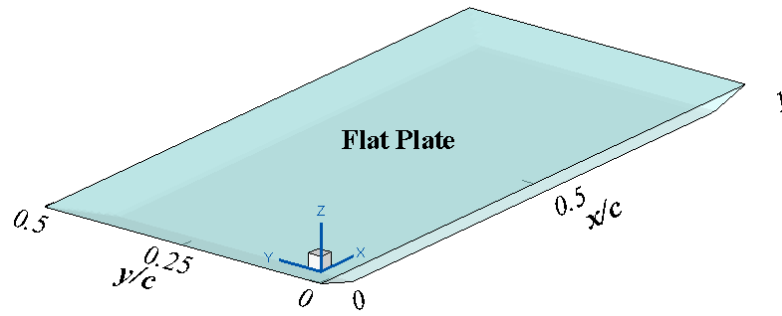


Figure 6.31 Computational flat plate geometry

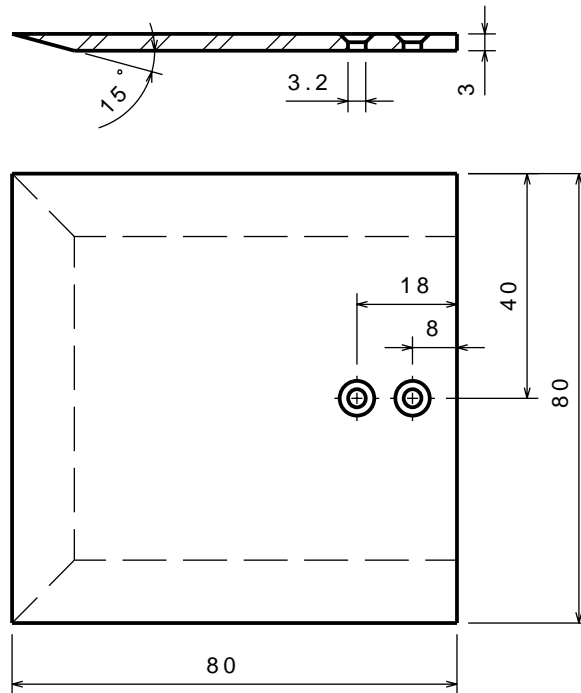


Figure 6.32 Model used for compressible oil flow tests [10].

6.2.2. Experimental Data For Comparison

The test cases are selected from the experimental data acquired at the von Karman Institute (VKI) [38], [39]. Test models are low aspect ratio, rectangular flat plates with small thickness and sharp edges. Model aspect ratios (AR) are 0.5, 0.67, 1.0 and 1.5. For AR=1.0, the low speed model dimensions are 100mm*100mm*5mm. This model was used for low speed oil flow visualization tests. The high-speed force model dimensions are 80mm*80mm*2mm. The high-speed pressure model dimensions are 100mm*100mm. Front and side edges of the models are sharp. The top surfaces of the models are not deflected at the edges and connected to the lower surfaces with 15° angle. In Figure 6.32, the top and side view drawings of the model used for high-speed oil flow measurements are shown.

The experiments include surface oil flow measurements, force and moment measurements and surface pressure distribution measurements. Low speed tests were carried out in the VKI low speed, open circuit wind tunnel of the suction type, designated L-2A. This tunnel has a 0.3 m diameter circular test section. Maximum tunnel velocity is 40 m/sec and the Reynolds number based on the model chord length is about 2×10^5 . At low speeds, oil flow visualizations were performed at different angles of attack varying from 0° to 40°. High-speed subsonic tests were carried out in the VKI S-1 wind tunnel. This is a closed circuit transonic / supersonic wind tunnel with 0.4 m * 0.4 m test section. Subsonic tests are performed in the transonic test section with slotted horizontal walls. High-speed tests include surface pressure distribution measurements, force and moment measurements and a few oil flow measurements. Mach number range was 0.4-0.9. Reynolds numbers varied between 1.63×10^5 and 2.62×10^5 .

6.2.3. Computational Grid

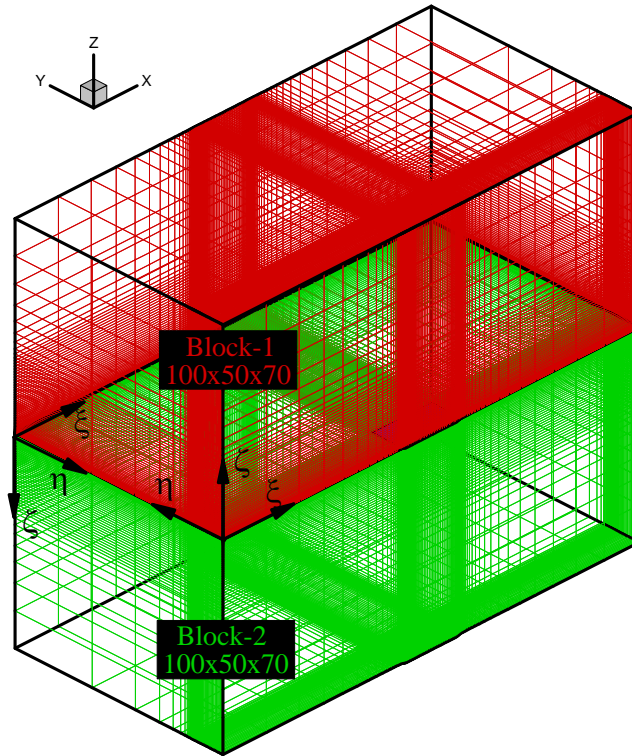


Figure 6.33 Overall view of the grid blocks, Block-1 and Block-2

Two-block, three-dimensional, structured grids shown in Figure 6.33 were generated for the computational flow domain mentioned above. In order to speed up the convergence of the solutions, two different grid configurations are adapted namely, the coarse and the fine grids. The coarse grid is obtained by halving the number of grid points of the fine grid in each coordinate direction. A three dimensional hyperbolic grid generation code [76] is employed to generate the grids. The grid parameters are shown in Table 6.7.

Table 6.7 The grids used in the computations

	<i>Initial Grid Spacing</i>	<i>Density</i>	<i>Total Number of Points</i>	<i>Maximum Marching Distance</i>
Fine Grid	1.0 E-4	100 x 50 x 70	700000	3.0
Coarse Grid	1.0 E-4	51 x 26 x 35	92820	3.0

In ζ direction, four different stretching ratios are used in four different regions to obtain desired grid densities. These regions are $0.0 \leq z/c \leq 0.1$, $0.1 \leq z/c \leq 0.5$, $0.5 \leq z/c \leq 1.0$, and $z/c > 3.0$.

For the coarse grid case, the grid dimensions for each block are $JMAX * KMAX * LMAX = 51 * 26 * 35$ points in ξ, η, ζ directions, respectively. On the flat plate surface, there are 31 points in ξ direction and 18 points in η direction. The first grid distance in ζ direction from the flat plate surface is $\Delta z/c = 0.0001$. The total number of points up to $z/c = 1.0$ is 30. Thus in two blocks total of 92820 grid points were produced.

For the fine grid case however, the grid dimensions for each block are $JMAX * KMAX * LMAX = 100 * 50 * 70$ points in ξ, η, ζ directions, respectively. On the flat plate surface, there are 61 points in ξ direction and 35 points in η direction. The first grid distance in ζ direction from the flat plate surface is the same. The total number of points up to $z/c = 1.0$ is 60. Thus in two blocks total of 700,000 grid points were produced.

In Figure 6.34, the grid details around the flat plate at the symmetry plane ($y/c=0.0$) are shown. In Figure 6.36, the top view of the grid at $z/c=0.0$ plane is shown. Notice that those figures are belonging to the fine grid case.

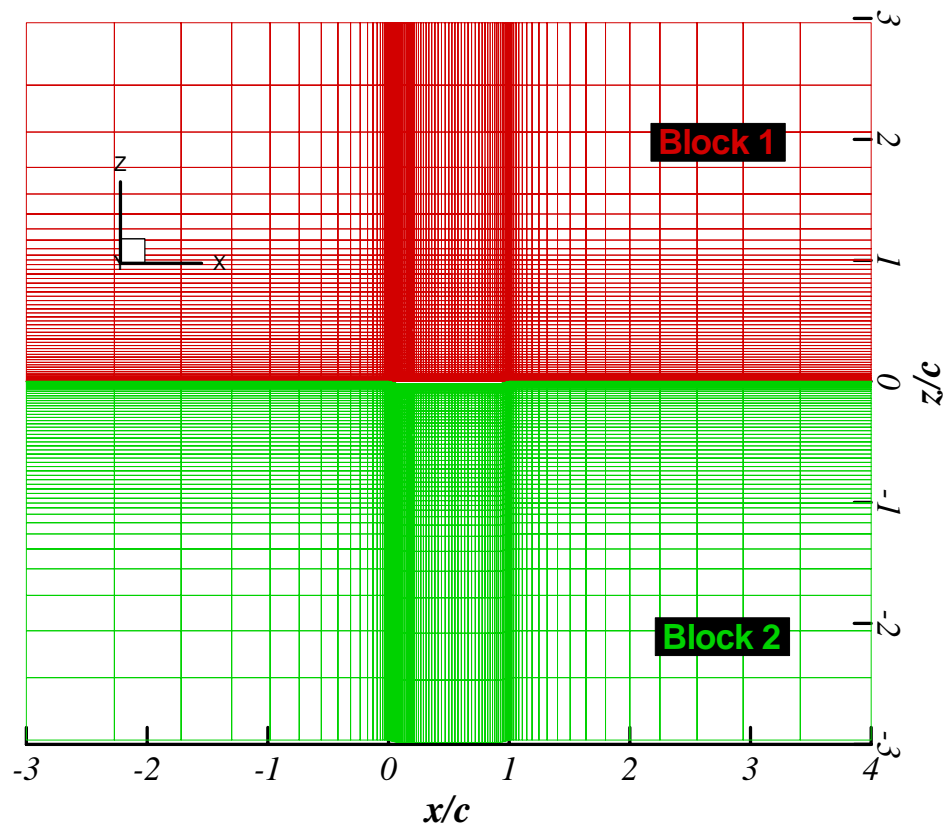


Figure 6.34 Symmetry plane ($y/c=0$) view of the grid around the flat plate.

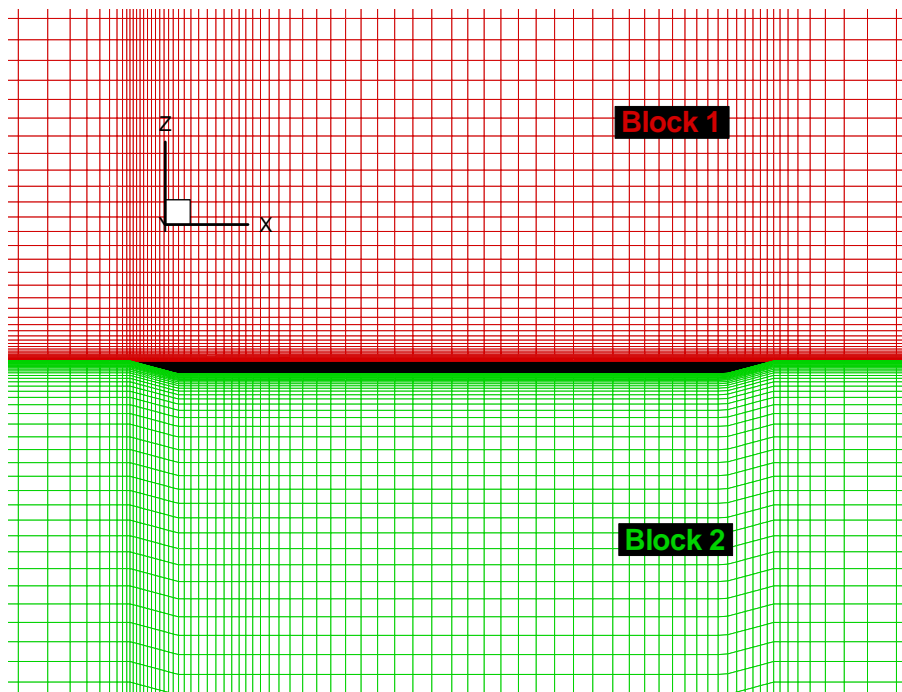


Figure 6.35 Zoomed view of Symmetry plane ($y/c=0$) of the fine grid around the flat plate.

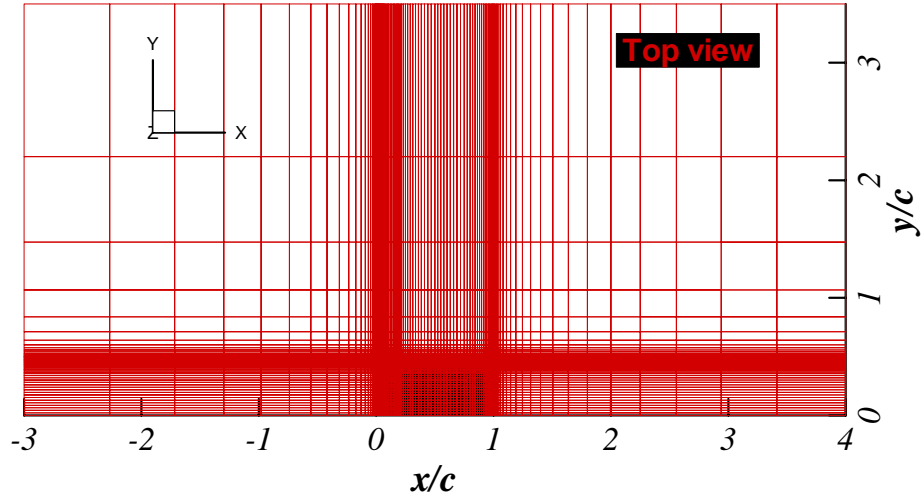


Figure 6.36 Top view of the grid at $z/c=0.0$ plane.

6.2.4. Boundary Conditions

Five different types of boundary conditions are used in each block as shown in Figure 6.37: (1) the upstream inflow boundaries; (2) the downstream outflow boundaries; (3) the symmetry boundary at the symmetry plane ($y/c=0$); (4) the flat plate itself and (5) the matched surface boundary.

The upstream inflow boundary condition or inflow bc is fixed by the freestream values. The downstream outflow boundary conditions, or extrapolation bc are just extrapolated from the interior values. The no-slip condition, or surface bc is applied on the flat plate surface. In the matched surface boundary, the values are interchanged instantly between two blocks by means of parallel processing. The boundary conditions used in Fine Grid solution of each block are summarized in the following table.

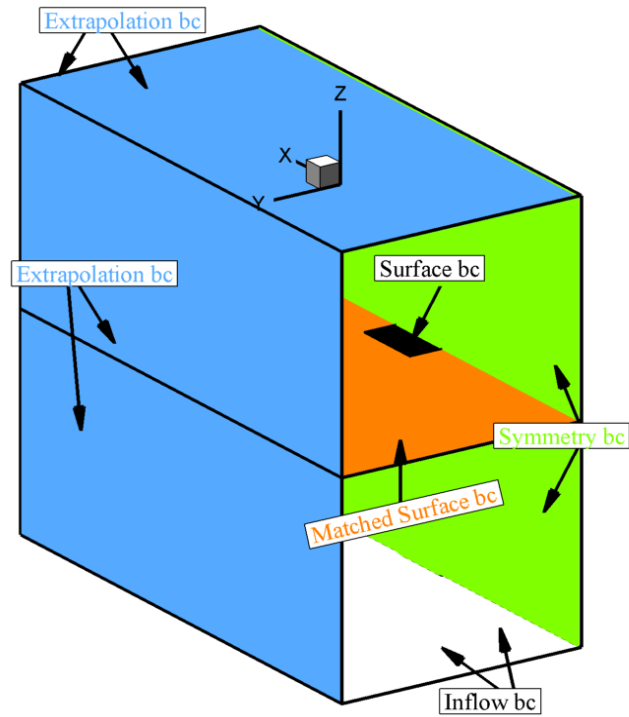


Figure 6.37 Boundary conditions

Table 6.8. Boundary conditions

	Boundary type	<i>J</i>	<i>K</i>	<i>L</i>	<i>Applied Condition</i>
Block-1	Upstream Inflow	1	1-50	1-70	<i>Fixed conditions</i>
	Downstream Outflow	100	1-50	1-70	<i>Extrapolation</i>
	Downstream Outflow	2-100	50	1-70	<i>Extrapolation</i>
	Downstream Outflow	2-100	2-50	70	<i>Extrapolation</i>
	Symmetry Plane	2-100	1	1-70	<i>Symmetry</i>
	Matched Surface	2-100	1-50	1	<i>Matched Surface</i>
	Flat Plate Surface	20-80	1-35	1	<i>No-slip</i>
Block-2	Upstream Inflow	1	1-50	1-70	<i>Fixed conditions</i>
	Upstream Inflow	1-100	1-50	70	<i>Fixed conditions</i>
	Downstream Outflow	2-100	1	1-69	<i>Extrapolation</i>
	Downstream Outflow	100	2-50	1-69	<i>Extrapolation</i>
	Symmetry Plane	2-100	50	1-69	<i>Symmetry</i>
	Matched Surface	2-100	1-50	1	<i>Matched Surface</i>
	Flat Plate Surface	20-80	16-50	1	<i>No-slip</i>

6.2.5. Solution Procedure

As mentioned above, two different, the coarse and the fine grid configurations are utilized in order to get fast convergence of the solution.

All cases (P1, P2, P3, P4, S1 and S2) were solved over the coarse grid by using a local time step (i.e., varying in space) with a CFL number of 20. For each Case, coarse grid solution procedures decided by the convergence criteria of the flow variables are as follows;

P1 Case was obtained for 40000 iterations using the Baldwin-Lomax turbulence model applied over the region: $x/c > 0.30$ of the flat plate.

P2 Case was obtained for 41000 iterations using the Baldwin-Lomax turbulence model applied over the complete flat plate surface.

P3 Case was obtained by applying the Baldwin-Lomax turbulence model;

→ for the first 35000 iterations over the region; $x/c > 0.30$

→ for the next 5000 iterations over the complete flat plate surface.

P4 Case was obtained for 66000 iterations using the Baldwin-Lomax turbulence model applied over the complete flat plate surface.

S1 Case was obtained for 45000 iterations using the Baldwin-Lomax turbulence model applied over the region: $x/c > 0.30$ of the flat plate.

S2 Case was obtained for 40000 iterations using the Baldwin-Lomax turbulence model applied over the complete flat plate surface.

The fine grid solutions were initialized by the interpolation of those coarse grid results. P1 and S1 Cases were obtained by applying the Baldwin-Lomax turbulence model over the region; $x/c > 0.3$ of the flat plate surface and the rest were all over of the complete flat plate surface. The iteration summary is given in Table 6.9

Table 6.9 Iteration summary

	P1	P2	P3	P4	S1	S2
Course Grid iterations	40000	41000	40000	66000	44750	40000
Fine Grid iterations	29300	21500	20750	74000	21800	82500
<i>total</i>	<i>69300</i>	<i>62500</i>	<i>60750</i>	<i>140000</i>	<i>66550</i>	<i>122500</i>

In the fine grid solutions, however, the time step was shifted to the global time step (i.e., constant in space) since the results showed that unsteady phenomena's were taking place such as oscillating of Normal Force and Pitching Moment, etc. The flow code computes the corresponding time step at every point in the grid, finds the minimum of those time steps, and resets the time step at every point to that minimum value. This allows the time step to be set for an unsteady flow problem by specifying a CFL number. Hence, approximately 20000-30000 more iterations for all cases were required for the convergence of the flow variables. This was achieved by tracing back the behavior of the flow variables until reaching a periodic oscillation for each case study. 20 samples of each solution over one cycle were saved in order to determine the time-mean average of each flow variable and visualize the flow oscillations and instabilities.

6.2.6. Computational Details

Computations are performed on Pentium IV 1500 MHz single processor workstation, which has 512 MB of memory. For coarse grid, a two-block parallel solution with 2×46410 grid points requires 2×16 MB of RAM. Approximately 240 minutes of CPU-time is needed per 10000 iterations. On the other hand, for fine grid, a two-block parallel solution with 2×350000 grid points requires 2×82 MB of RAM and approximately 1600 minutes of CPU-time is needed per 10000 iterations. The computational details are given in Table 6.10.

Table 6.10 Computational details

	<i>CPU time (minute/10000 iterations)</i>	<i>Memory Requirement (Mb)</i>	<i>Number of Points</i>
Course Grid	240	32000	92820
Fine Grid	1600	164000	700000

6.2.7. Results and Comparison

6.2.7.1. Convergence Histories

Convergence histories are computed by means of L2 Norm of Residue and the Force-Moment coefficients. In Figure 6.38, the convergence Histories of the L2 norm of the residual is shown for each case including the solutions of the coarse and fine grid for each block. Notice that number of iterations for the convergence of S2 is highly greater than the other case's since it was the first case worked on to decide on the applied time step ; local or global. As seen on that figure, it was solved by using the local time step until 93000 iterations then continued by the global time step. The other cases were solved by using the global time step in the fine grid part of their solutions. Notice that in the L2 residue variations, small jump at the just ending of the coarse grid solutions of P2 Case for example, is the result of the change in the application region of the turbulence models. The Figure 6.39 shows only the fine grid part of the convergence history for each block.

In addition, the convergence histories in terms of the Normal Force Coefficient and Pitching Moment Coefficient are illustrated in Figure 6.40 and Figure 6.41. Those figures represent only the fine grid part of the solution and include the information from both blocks since the normal force and pitching moment are obtained by integration of the surface pressures from top and the bottom surfaces. Notice that the maximum and minimum values are arranged to make clear the oscillatory behavior of each case.

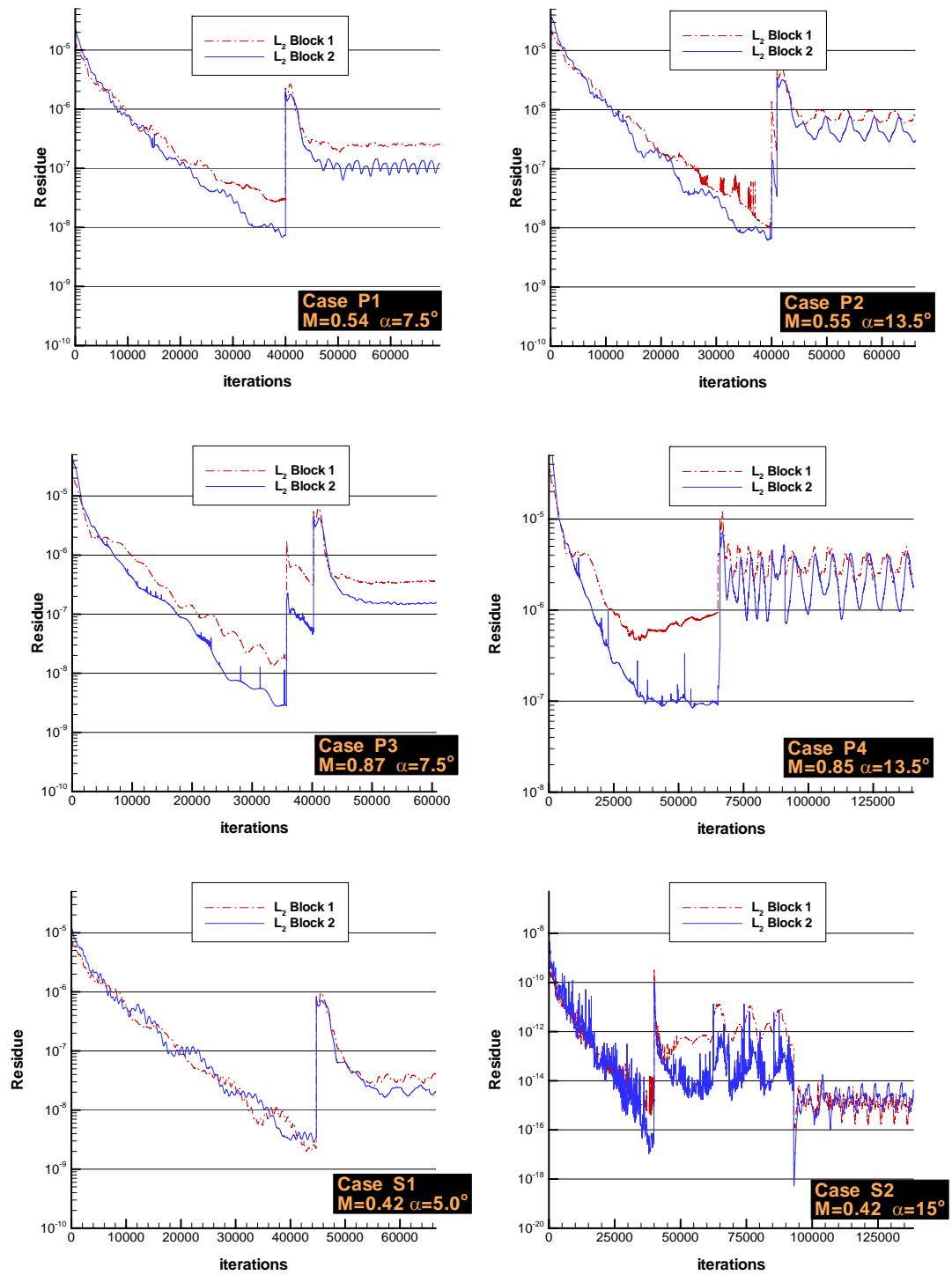


Figure 6.38 Convergence histories for the coarse and fine grid for each Case

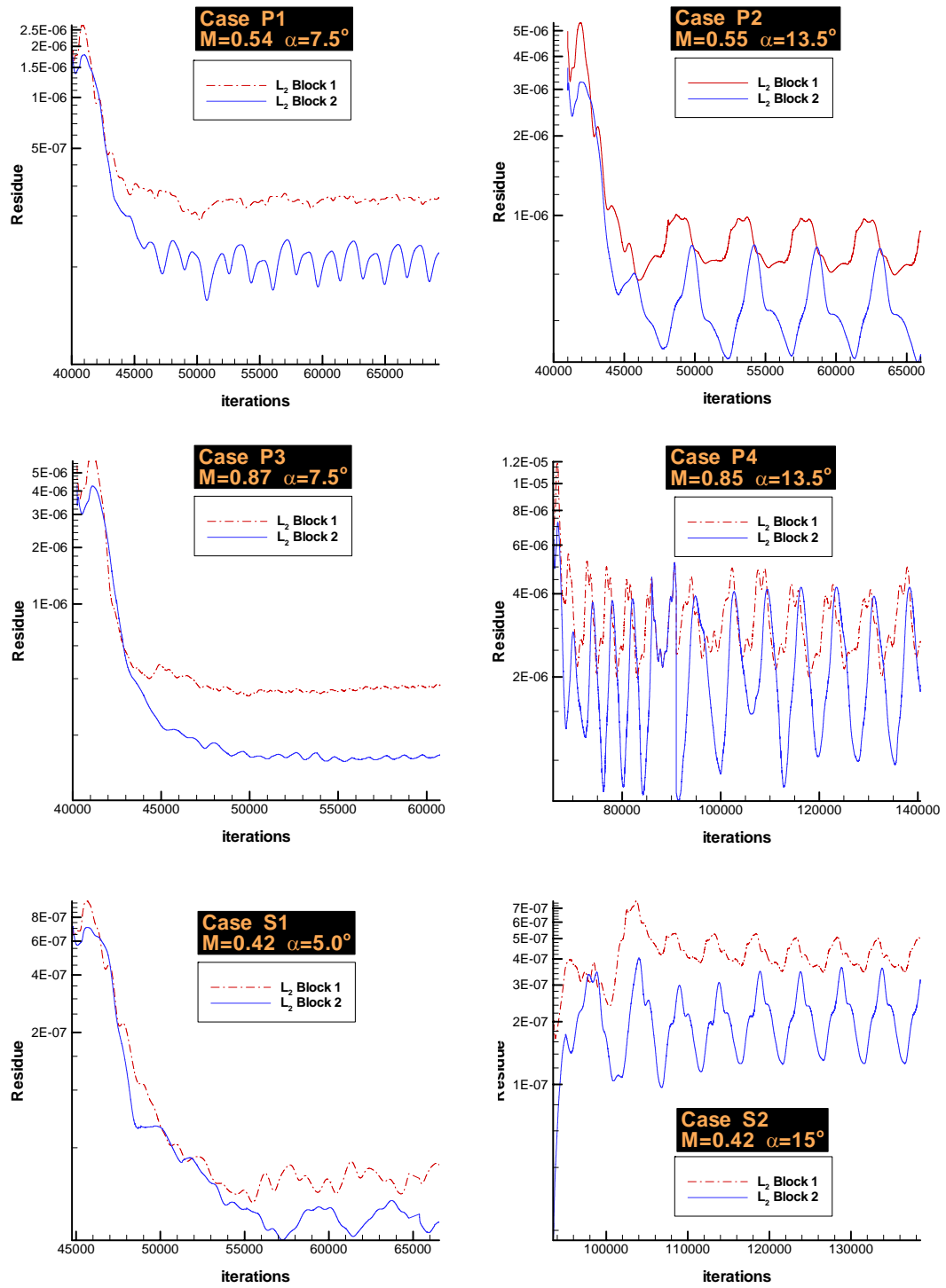


Figure 6.39 Convergence histories for only the fine grid for each Case

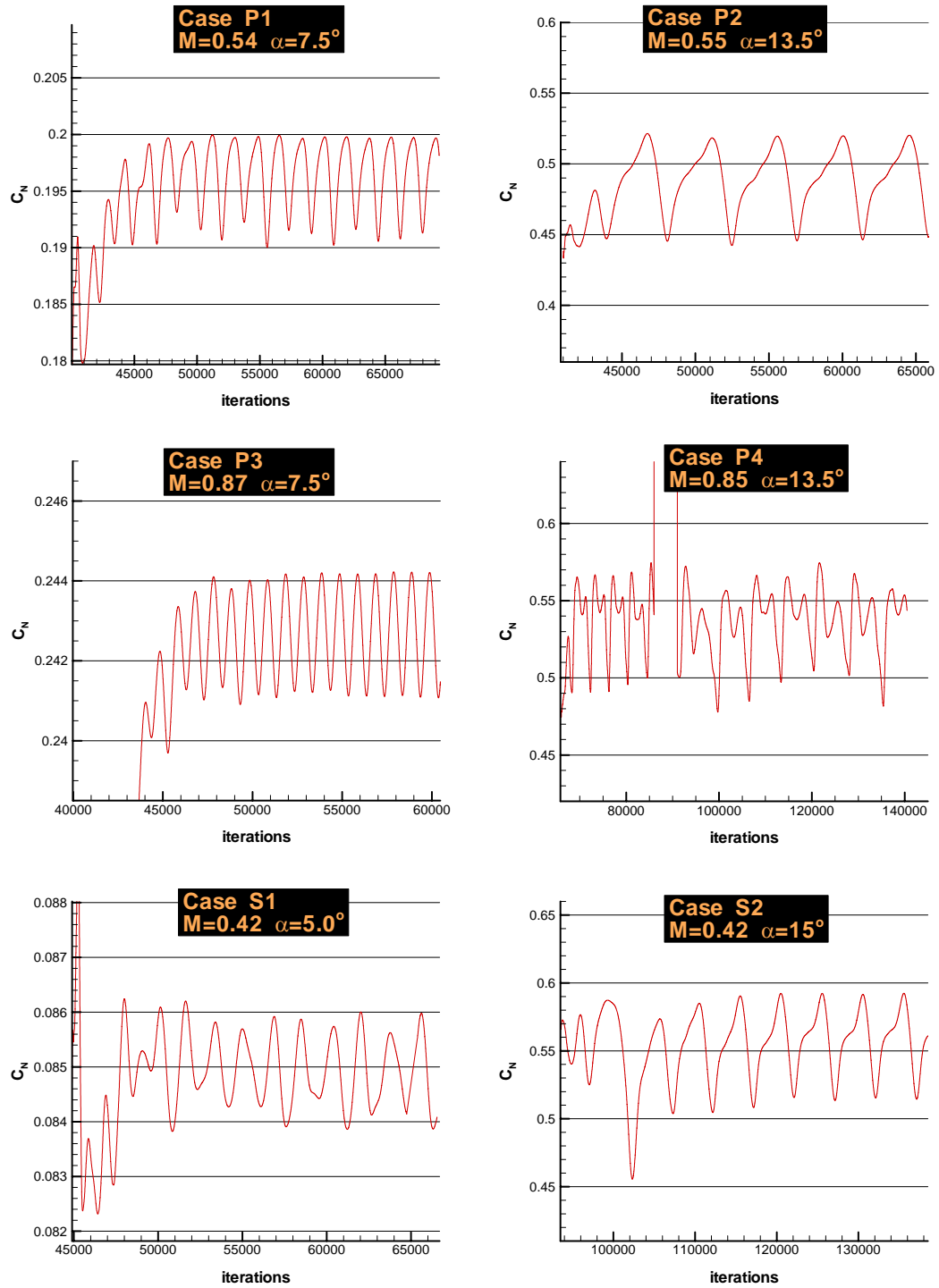


Figure 6.40 Convergence histories in terms of Normal Force

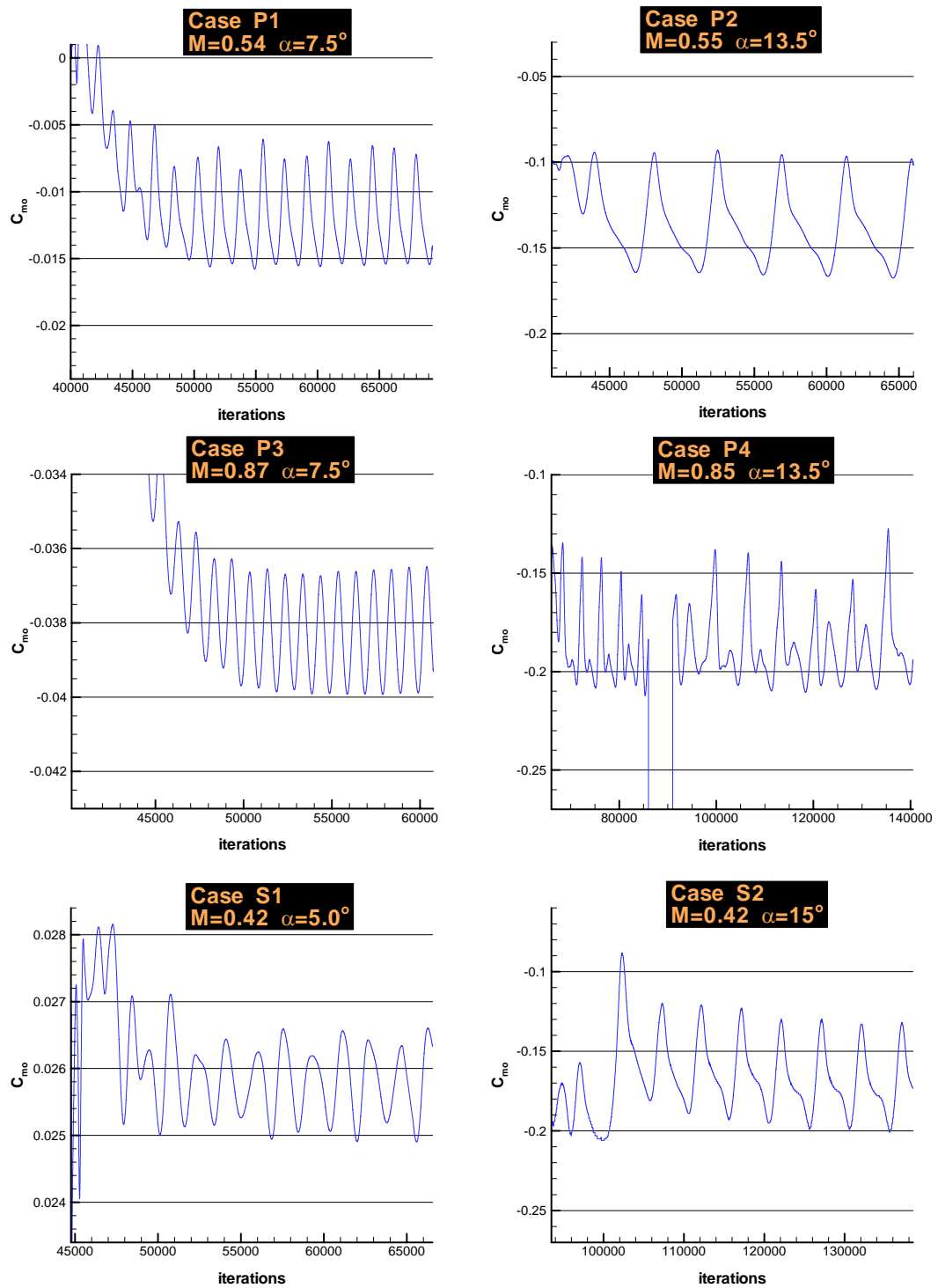


Figure 6.41 Convergence histories in terms of Pitching Moment

Table 6.11 Solution summary

		P1	P2	P3	P4	S1	S2
Computation	Mach number, M_∞	0.54	0.55	0.87	0.85	0.42	0.42
	angle of attack, α	7.5	13.5	7.5	13.5	5	15
	iteration number in one cycle	1800	5000	1000	7000	1800	5000
	iteration step for data output	90	250	50	350	90	250
	code time step for one iteration, dt	0.0018	0.0018	0.0018	0.0010	0.0018	0.0018
	dimensional time step, dt (s)	7.92E-07	7.77E-07	4.91E-07	2.79E-07	1.02E-06	1.02E-06
	non-dimensional period, T	3.2	9.0	1.8	7.0	3.2	9.0
	dimensional period, T (s)	0.00142	0.00389	0.00049	0.00196	0.00183	0.00509
	non-dimensional frequency, f	0.309	0.111	0.556	0.143	0.309	0.111
	dimensional frequency, f (1/s)	702	257	2035	511	546	196
Conditions for Dimensional Data	Free Stream temperature, T_∞ (K)	282.4	282.4	282.4	282.4	282.4	282.4
	Free stream velocity, U_∞ (m/s)	181.90	185.27	293.06	286.32	141.48	141.48
	Chord length of the flat plate, c (m)	0.08	0.08	0.08	0.08	0.08	0.08

Table 6.11 summarizes the frequencies and the periods for each case. In order to get a feeling of the situation, dimensional data is also obtained based on the conditions described at this table. One complete cycle for each case occurs approximately over the iteration range from 1800 to 7000 and represents actually the oscillation generated by the separation bubble since there are other sources with minor oscillations.

The freestream velocity “ U_∞ ” is calculated by using the following relation,

$$U_\infty = M_\infty \sqrt{\gamma R T_\infty} \quad (6.6)$$

The code time, “ \tilde{t} ” refers to the non-dimensional time used in the computer code, determined by

$$\text{code time, } \tilde{t} = t \left(\frac{U_\infty}{c} \right) \quad (6.7)$$

where “ c ” is the chord length of the plate and “ t ” is the dimensional time.

Figure 6.42 and Figure 6.43 show the dimensional and non-dimensional frequency variation with the angle of attack, respectively. They inform that the frequency increases with decreasing angle of attack and, its variation is more rapid for higher Mach numbers.

One periodic cycle of the Normal Force Coefficient and Pitching Moment Coefficient variation with “the code time” and “the real time” can be seen in Figure 6.44. where the real time refers to the dimensional time.

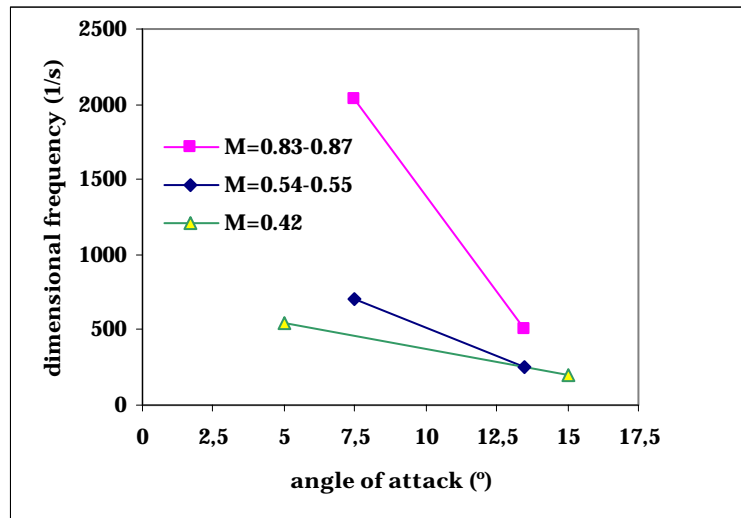


Figure 6.42 Dimensional frequency variation with the angle of attack

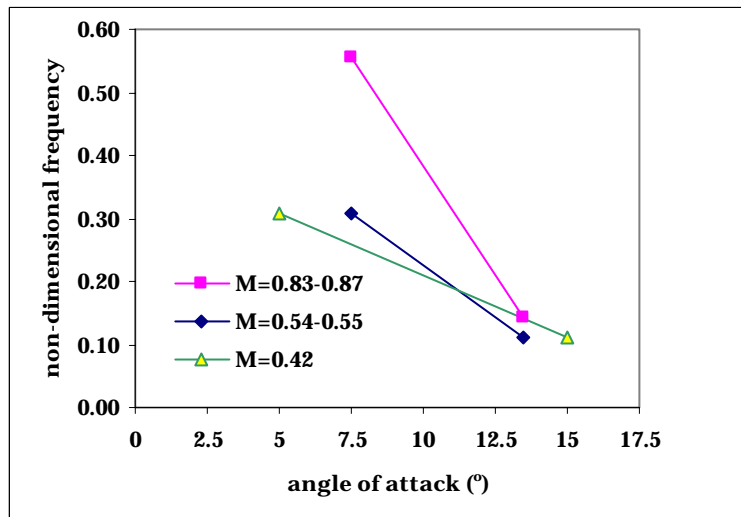


Figure 6.43 Non-dimensional frequency variation with the angle of attack

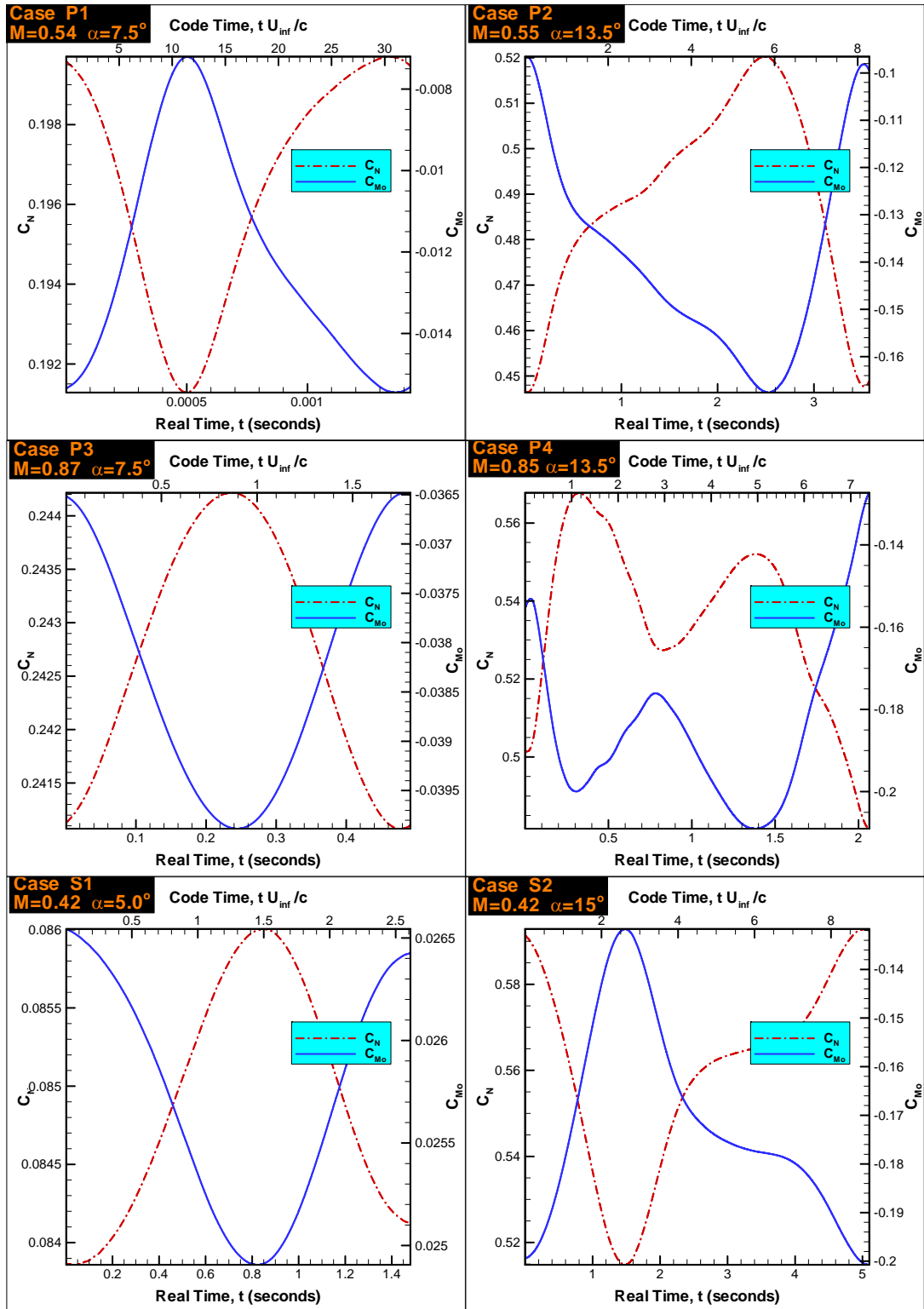


Figure 6.44 Variation of the force-moment coefficients over one periodic cycle

6.2.7.2. Comparison with the Experiment

i. Pressure Comparisons

Experimentally obtained surface pressures that contains totally 36 pressure locations in one-half of the plate were drawn in three-dimensional form and arranged for comparison of each case. The computational pressures are obtained as the time-mean average of the each corresponding case. Each graph is colored with the same pressure contour as illustrated in Figure 6.45 through Figure 6.48. Also as a closer comparison, each surface strips along x/c and y/c are made comparable with the experiment as shown in Figure 6.49 through Figure 6.56.

As seen on comparisons, pressure suction levels at stations nearest to the leading edge region in the neighborhood of wing centerline, show small deflections from the experiment due to the high complexity of the flow structure here. It may require a more capable turbulence model that can predict the flow features around those regions. However, the other regions are in agreement with the experiment. It must also be noticed that those computational results are belonging to the time-mean averaged data. Time-resolved simulations show results that are more accurate in terms of peak suction levels. Time-resolved simulations of three dimensional pressure contours can be seen on the Simulation CD Package included with the thesis.

P1

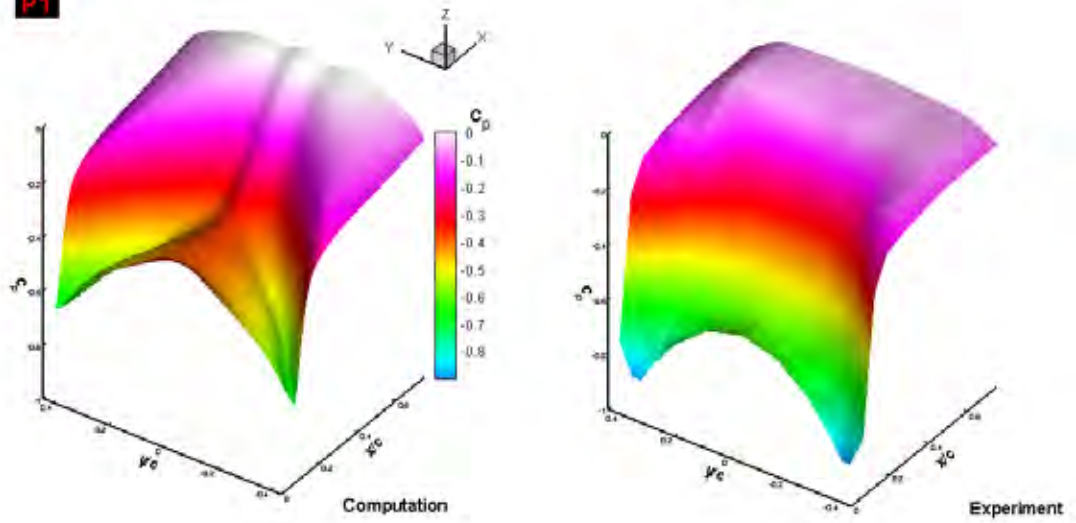


Figure 6.45 The computed time-mean averaged and experimentally obtained surface pressures in comparison. Mach=0.54, $\alpha=7.5^\circ$

P2

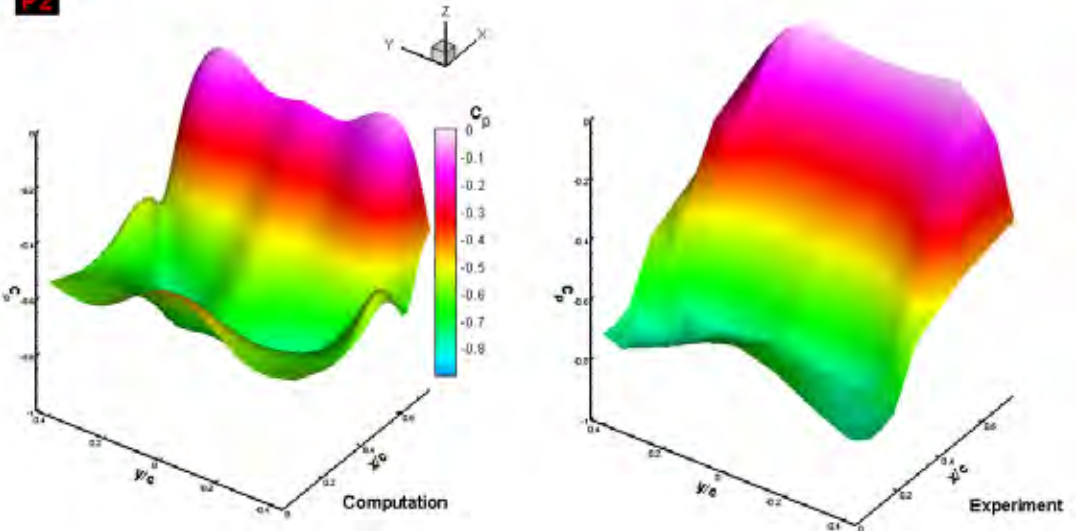


Figure 6.46 The computed time-mean averaged and experimentally obtained surface pressures in comparison. Mach=0.55, $\alpha=13.5^\circ$

P3

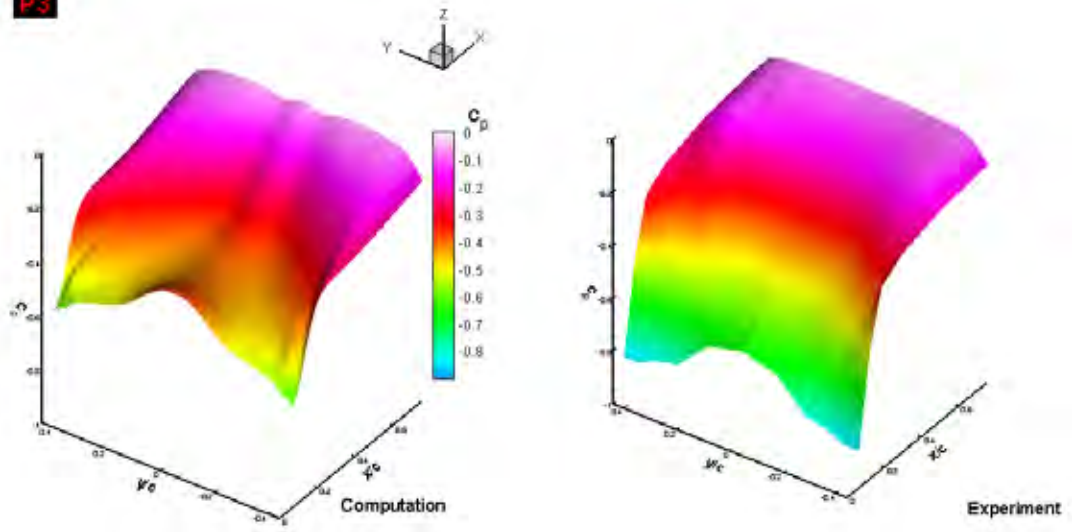


Figure 6.47 The computed time-mean averaged and experimentally obtained surface pressures in comparison. Mach=0.87, $\alpha=7.5^\circ$

P4

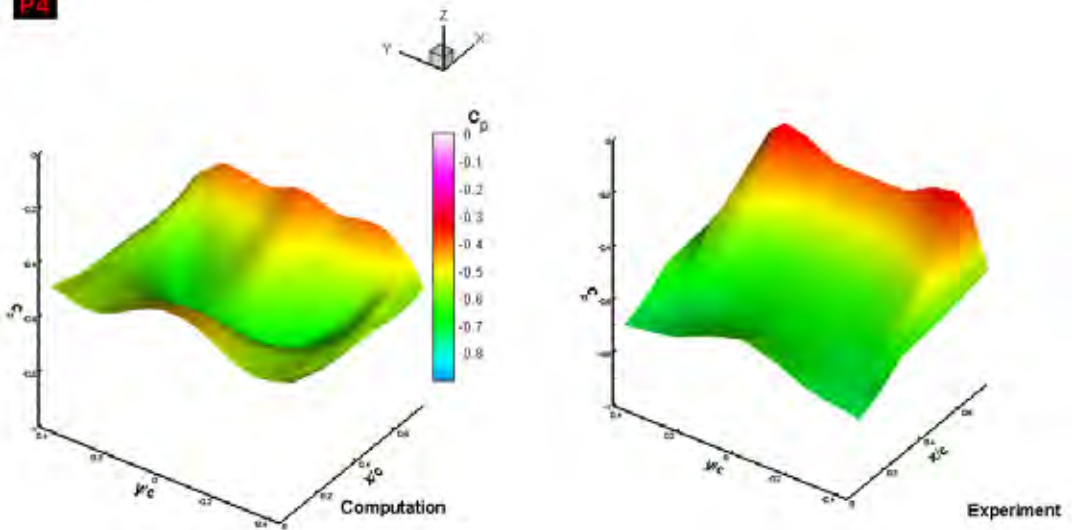


Figure 6.48 The computed time-mean averaged and experimentally obtained surface pressures in comparison. Mach=0.85, $\alpha=13.5^\circ$

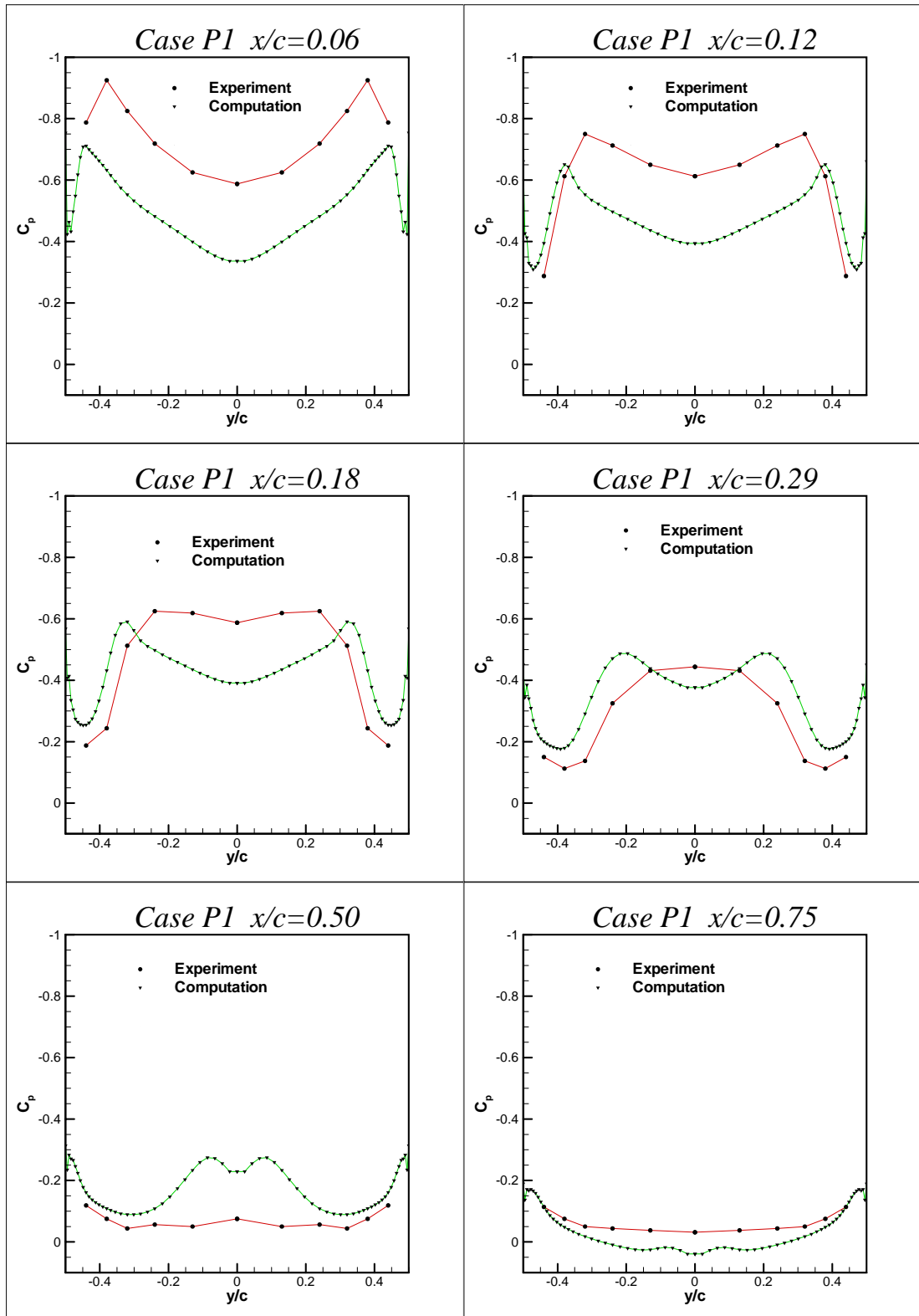


Figure 6.49 Comparison of computational and experimental [36] surface pressures along y strips. Case: P1 Mach=0.54, $\alpha=7.5^\circ$

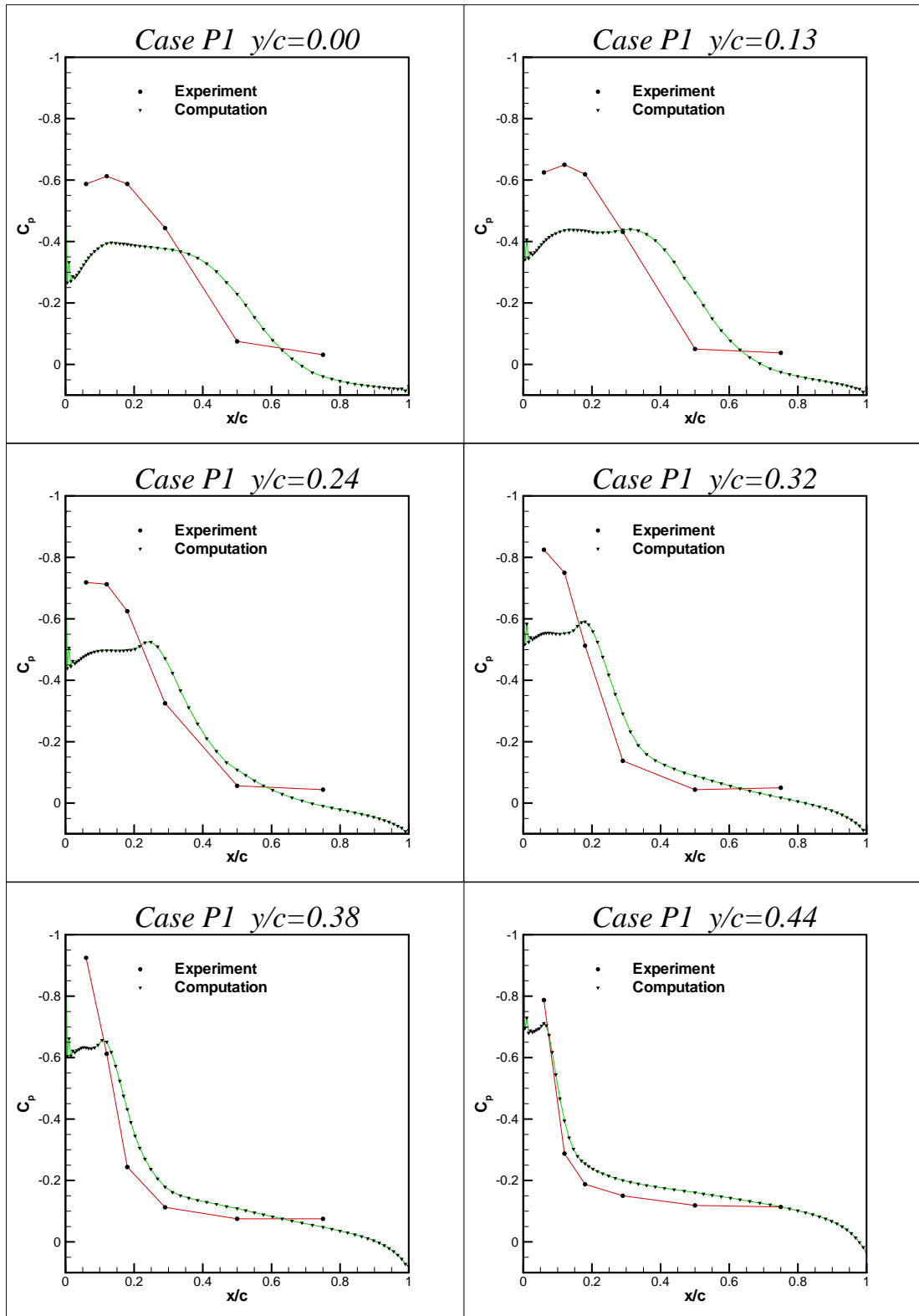


Figure 6.50 Comparison of computational and experimental [36] surface pressures along x strips. Case: P1 Mach=0.54, $\alpha=7.5^\circ$

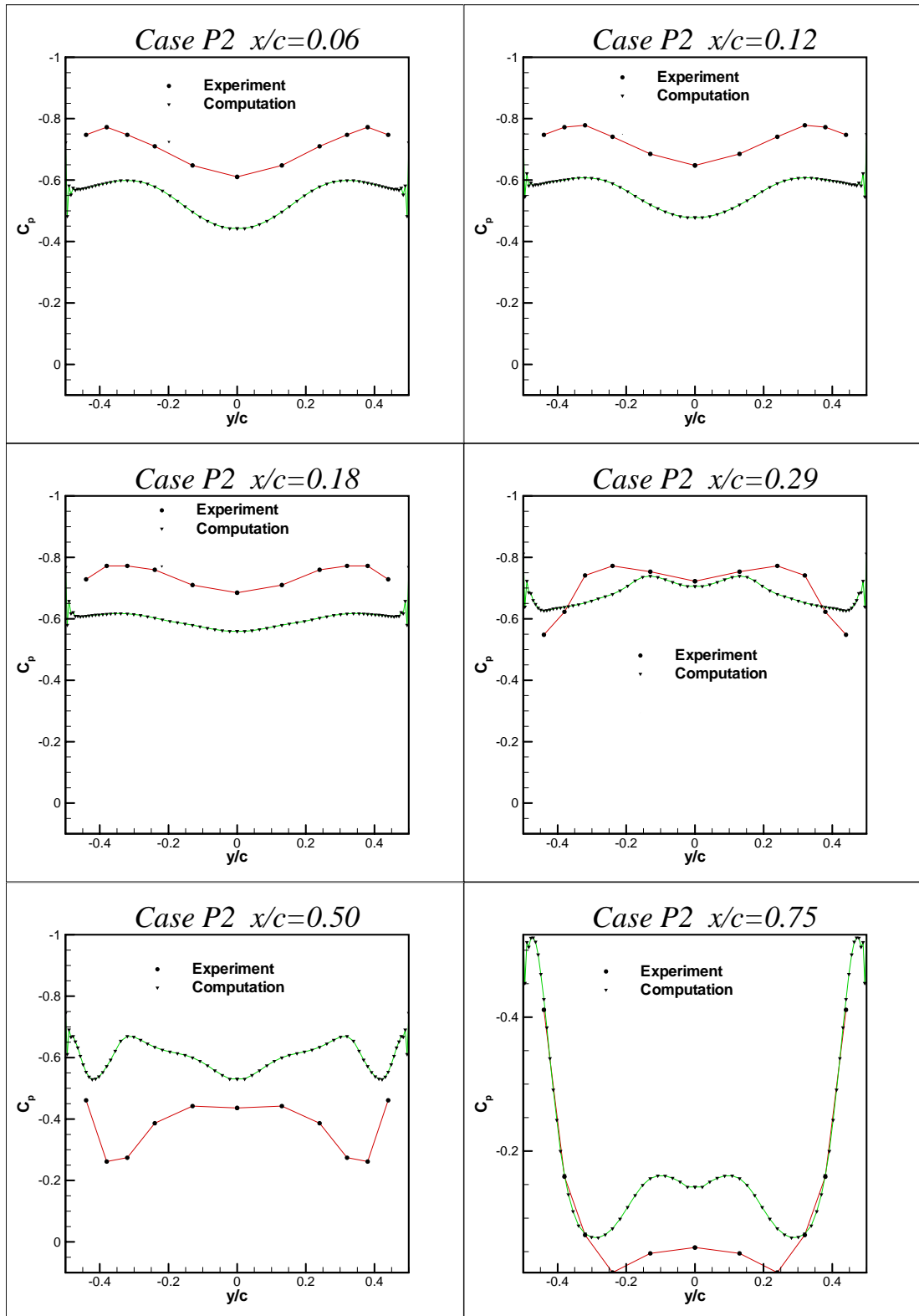


Figure 6.51 Comparison of computational and experimental [36] surface pressures along y strips. Case: P2 $Mach=0.55$, $\alpha=13.5^\circ$

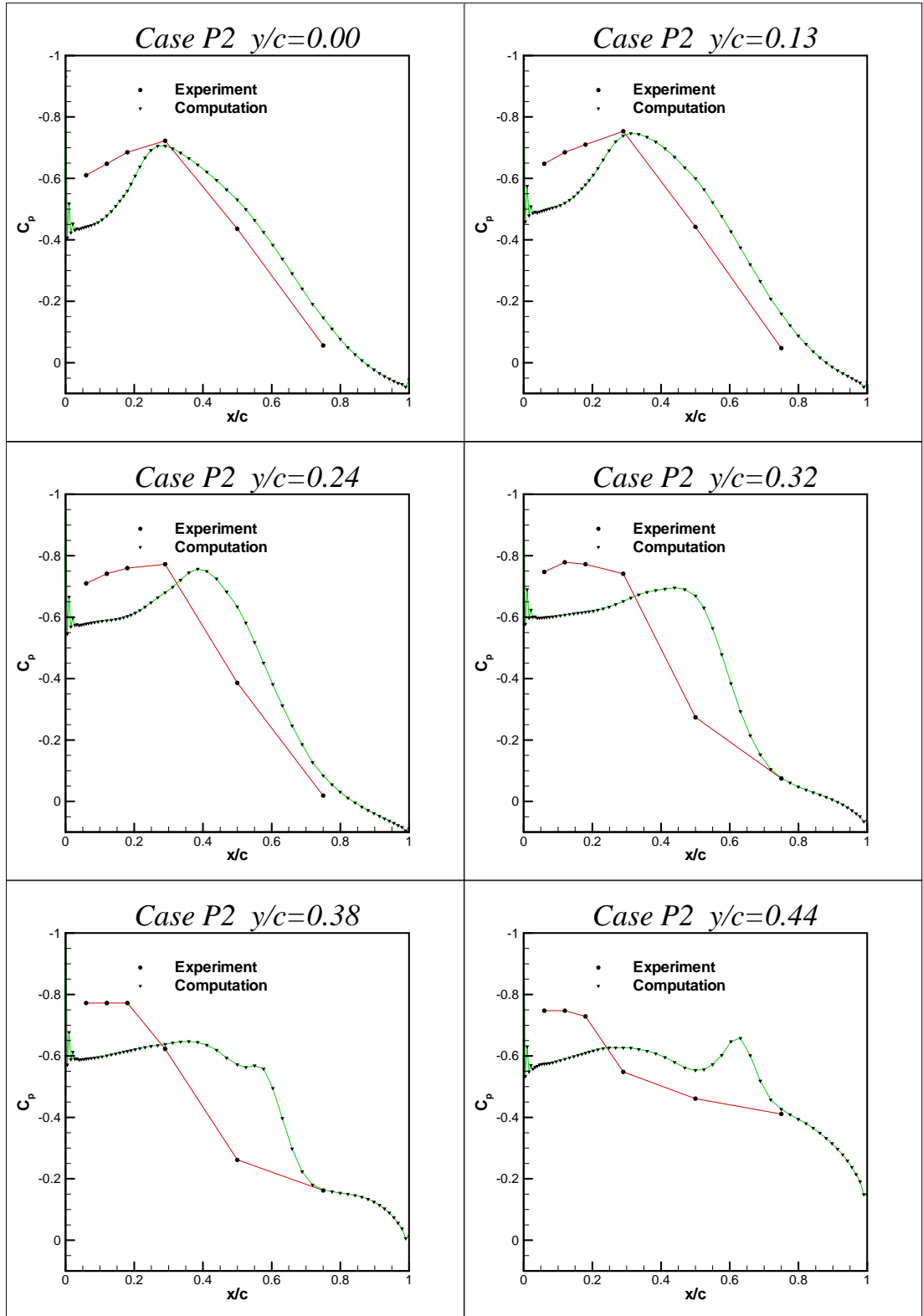


Figure 6.52 Comparison of computational and experimental [36] surface pressures along x strips. Case: P2 $Mach=0.55$, $\alpha=13.5^\circ$

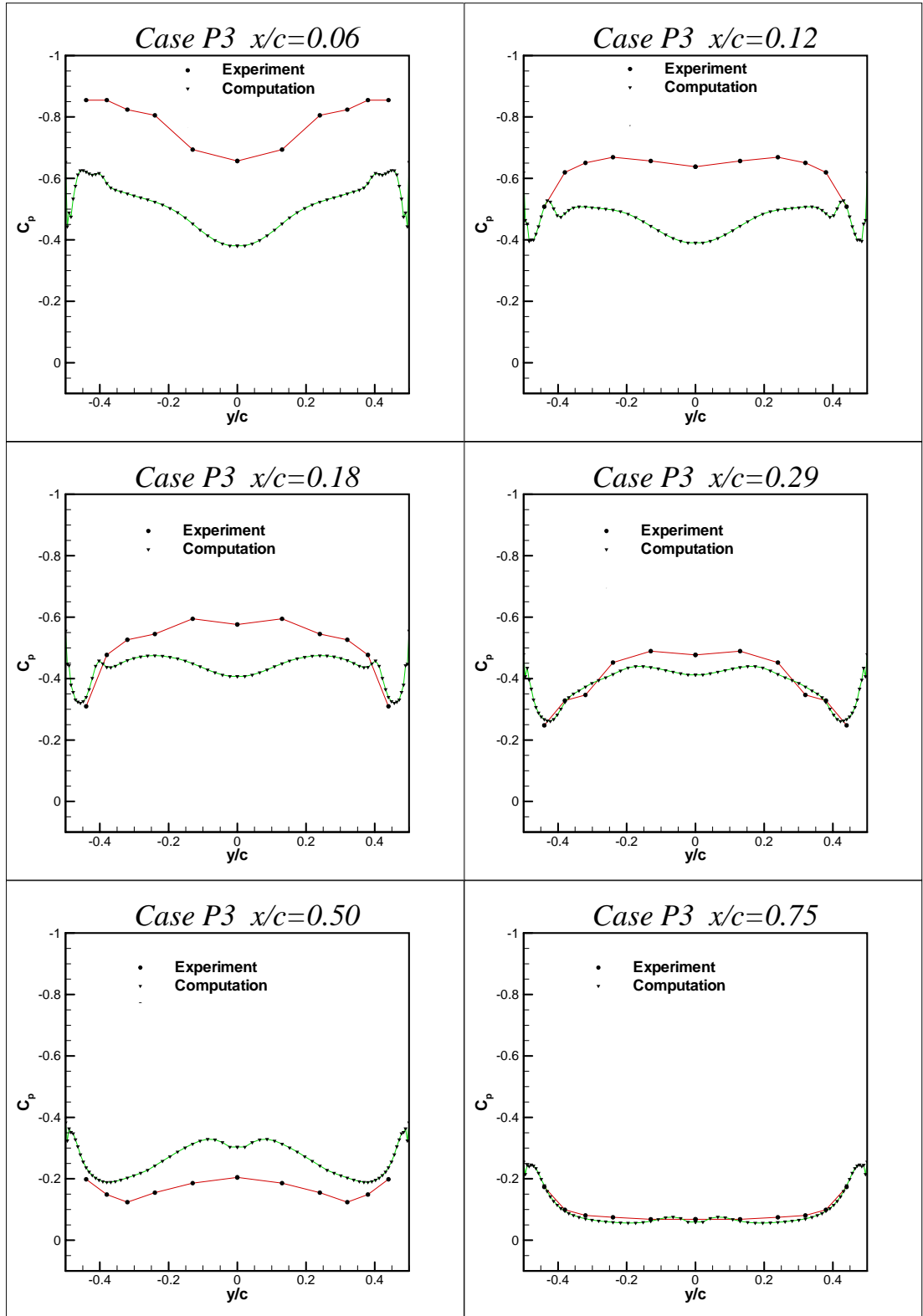


Figure 6.53 Comparison of computational and experimental [36] surface pressures along y strips. Case: P3 Mach=0.87, $\alpha=7.5^\circ$

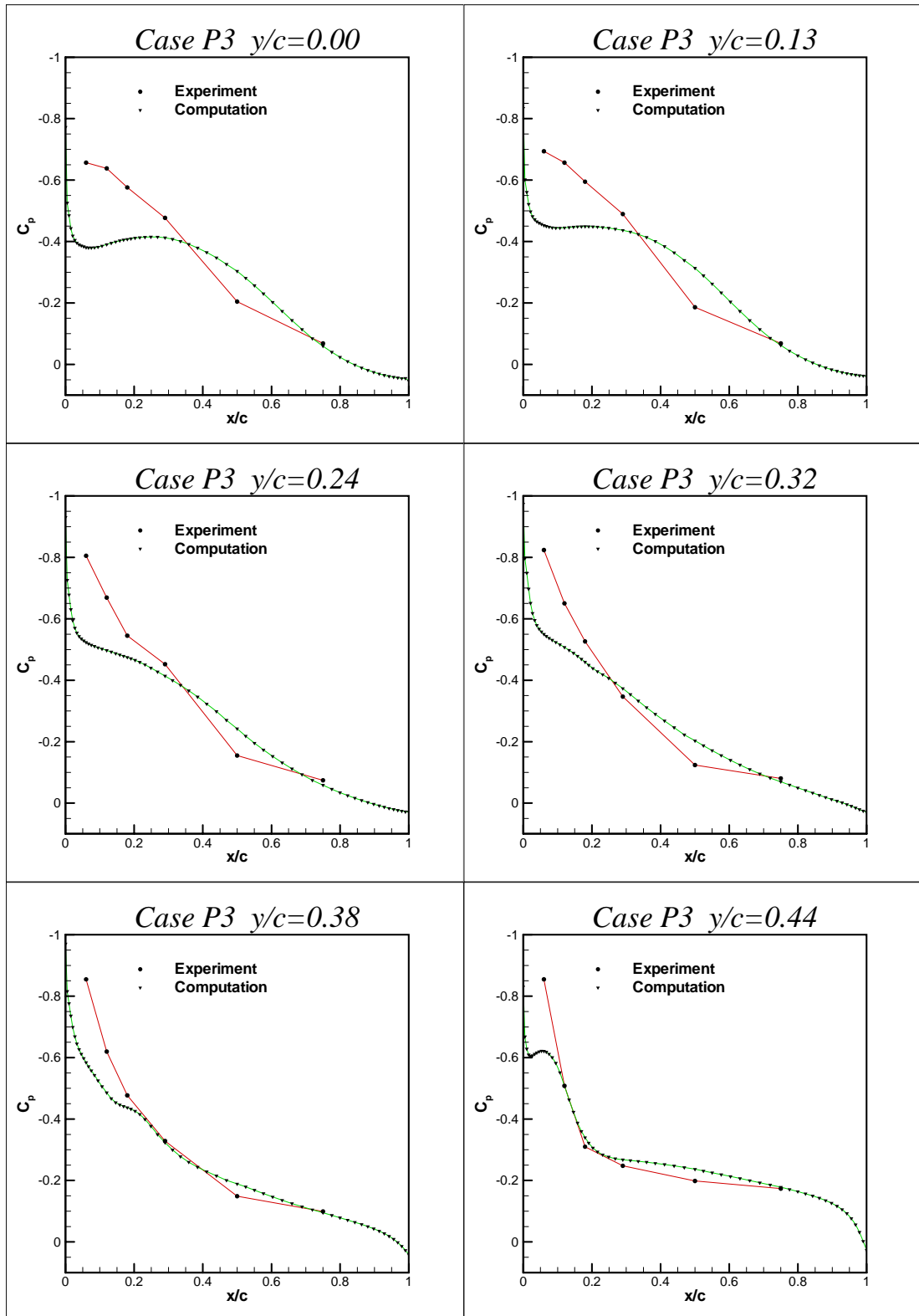


Figure 6.54 Comparison of computational and experimental [36] surface pressures along x strips. Case: P3 Mach=0.87, $\alpha=7.5^\circ$

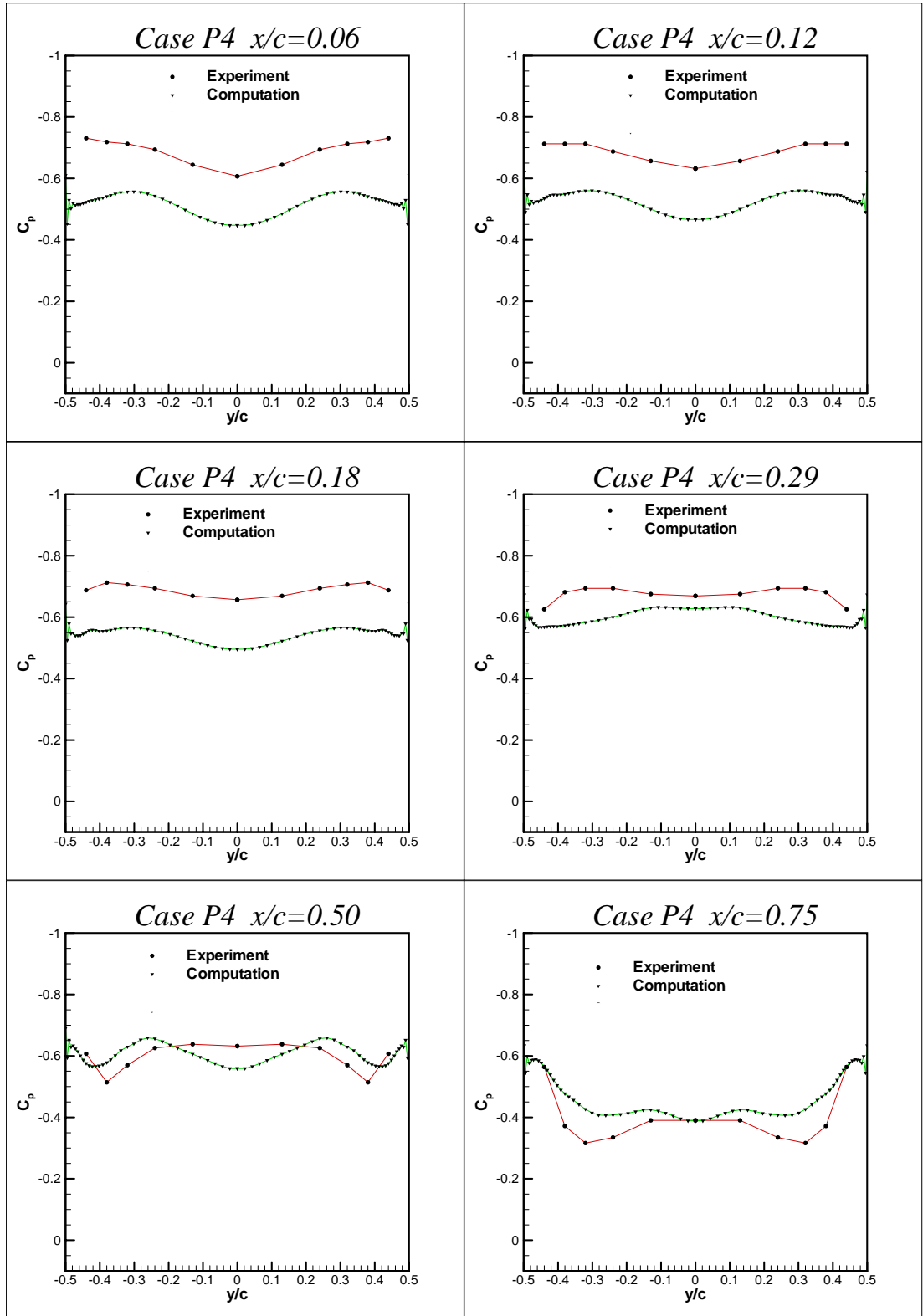


Figure 6.55 Comparison of computational and experimental [36] surface pressures along y strips. Case: P4 Mach=0.85, $\alpha=13.5^\circ$

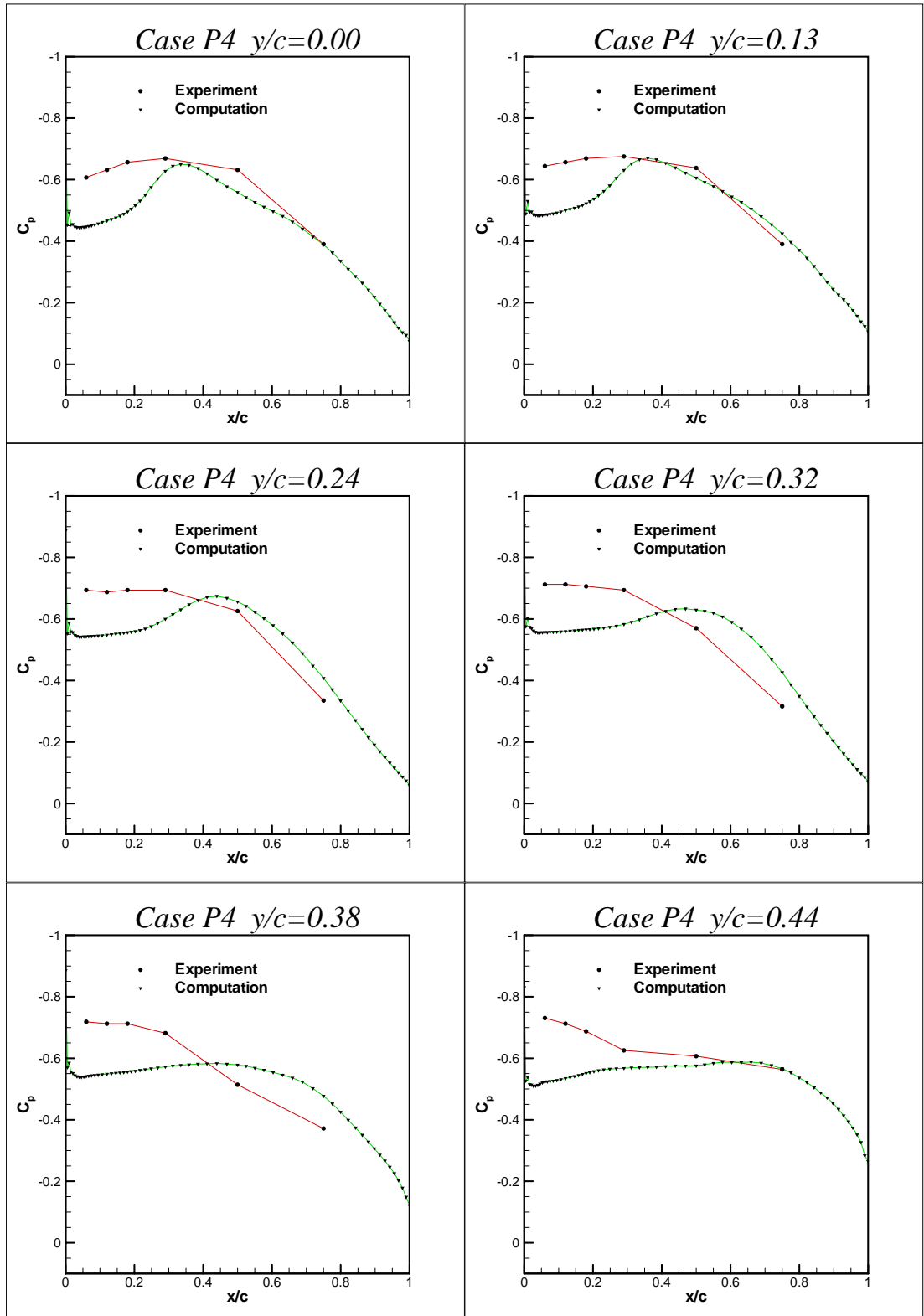


Figure 6.56 Comparison of computational and experimental [36] surface pressures along x strips. Case: P4 Mach=0.85, $\alpha=13.5^\circ$

ii. Surface Skin-friction Comparisons

The experimentally obtained surface streamlines on the leeward surface as shown in Figure 6.57 and Figure 6.58 were obtained by using the oil-flow method in the low speed tunnel at angle of attack of 5° and angle of attack of 15° , respectively [39]. In Figure 6.59 and Figure 6.60, the computationally obtained streamlines are shown for Mach=0.42 at angle of attack of 5° and angle of attack of 15° , respectively. They are drawn from the time-mean averaged data obtained by means of averaging the solution data, stored at the equal time intervals by the computer, over the one corresponding cycle of computation.

The comparison between computationally and experimentally obtained streamlines was given in Figure 6.61 and Figure 6.62. The formation and the size of the leading edge vortices are predicted well. In addition, the leading edge bubble formation is in good agreement with the experiment.

Figure 6.63 and Figure 6.64 are deductions from Figure 6.59 and Figure 6.60 of the corresponding pattern of skin-friction lines, respectively. The surface streamlines actually represents the traces of the skin friction lines that describes the structure of the flow separation around the body. The streamline pattern depicts the various interconnections between the node, saddle points and the paths of the separated flow around the leading edge. The streamlines emanating from the saddle points, called as separatrices, represents the regions of the flow that separate from one another [26]. It is seen in Figure 6.63 four spiral nodes, one nodal point of attachment and four saddle points on the leeward surface. Each of the four saddle points separates the flow from adjacent pairs of nodes. In Figure 6.64 there are two major and four minor spiral nodes, four nodal point of attachment and ten saddle points on the leeward surface. For both patterns, two saddle points situated on the wing centerline shows the primary and secondary bubbles.



Figure 6.57 Experimentally obtained top surface streamlines $\alpha=5^\circ$, $\text{Mach}\cong 0.1$, $\text{Re}=2.0\cdot 10^5$ [39]. The flow is from bottom to top.

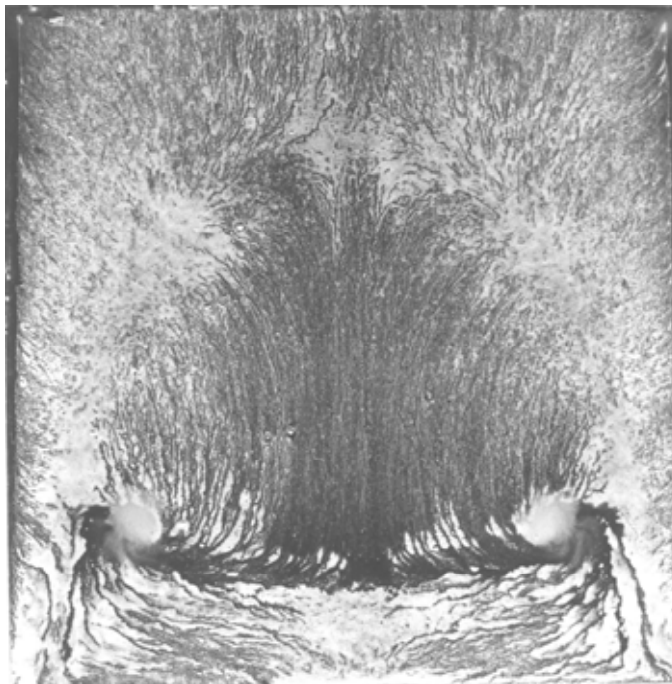


Figure 6.58 Experimentally obtained top surface streamlines $\alpha=15^\circ$, $\text{Mach}\cong 0.1$, $\text{Re}=2.0\cdot 10^5$ [39]. The flow is from bottom to top.

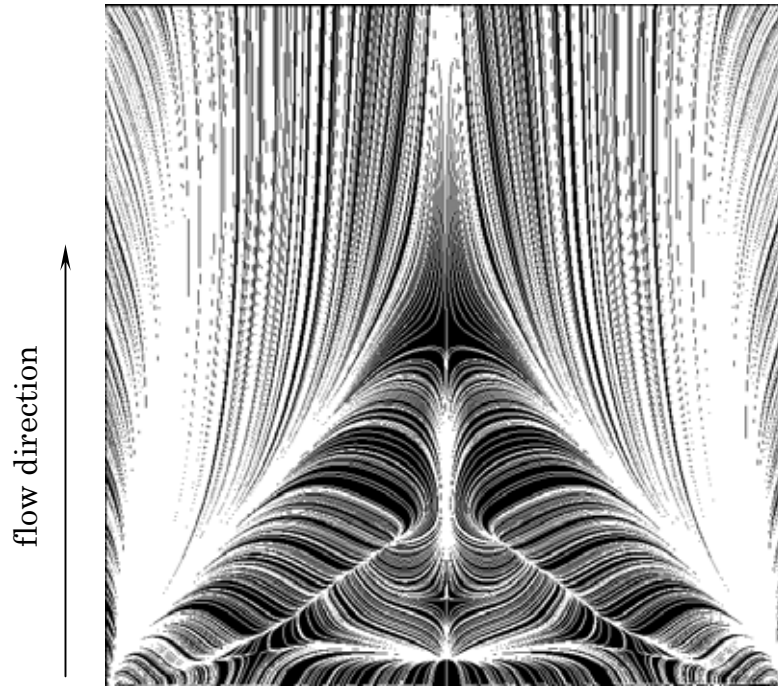


Figure 6.59 Computationally obtained top surface streamlines (time-mean averaged). Case: S1 $\alpha=5^\circ$, Mach = 0.42.

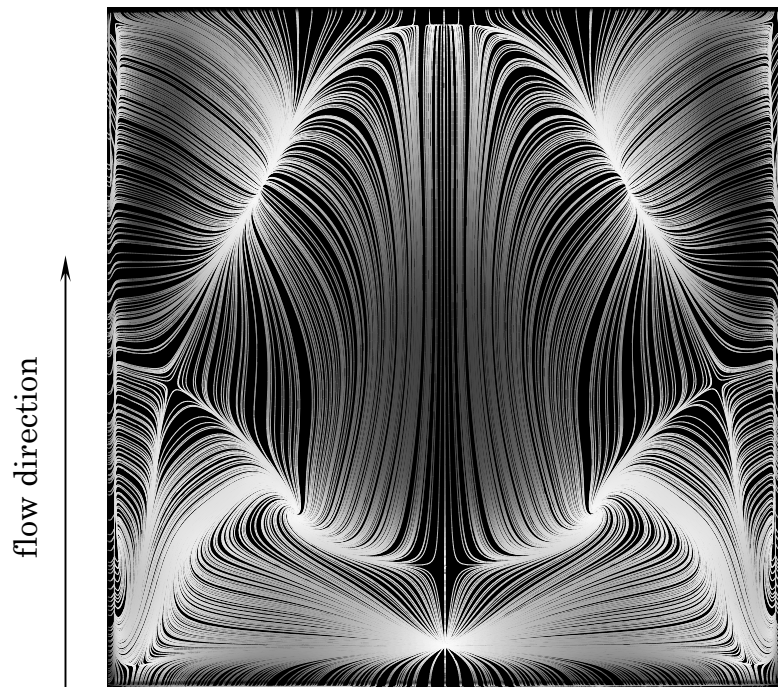


Figure 6.60 Computationally obtained top surface streamlines (time-mean averaged). Case: S2 $\alpha=15^\circ$, Mach = 0.42.

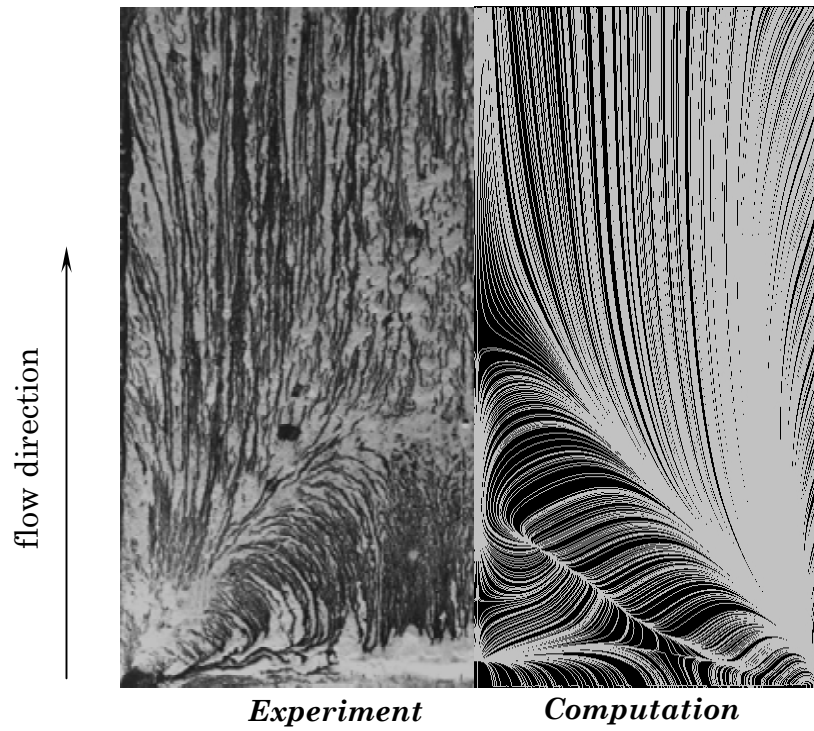


Figure 6.61 Comparison of computational (time-mean averaged) and experimental [39] top surface streamlines. Case S1 $\alpha=5^\circ$, Mach = 0.42.

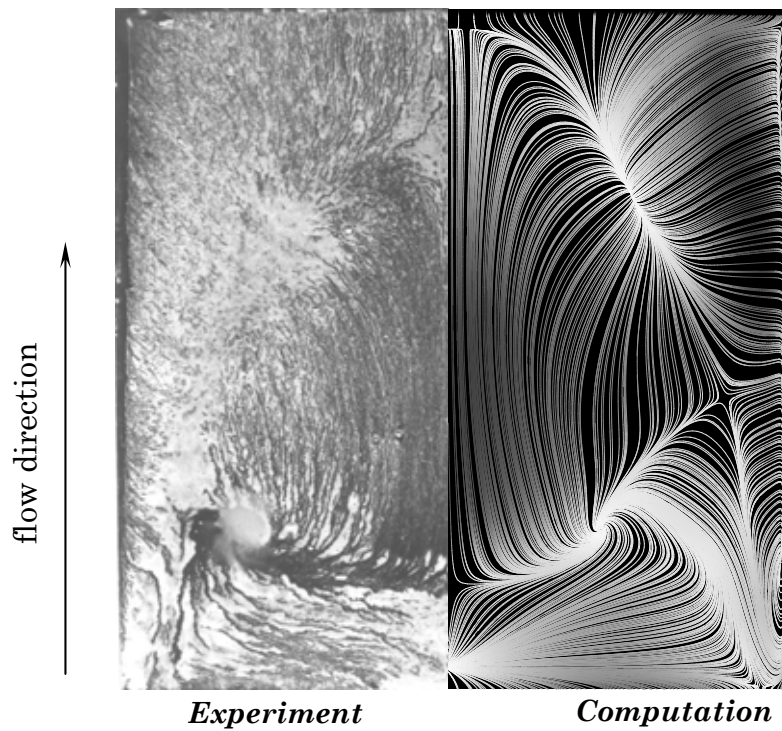


Figure 6.62 Comparison of computational (time-mean averaged) and experimental [39] top surface streamlines. Case S2 $\alpha=15^\circ$, Mach = 0.42.

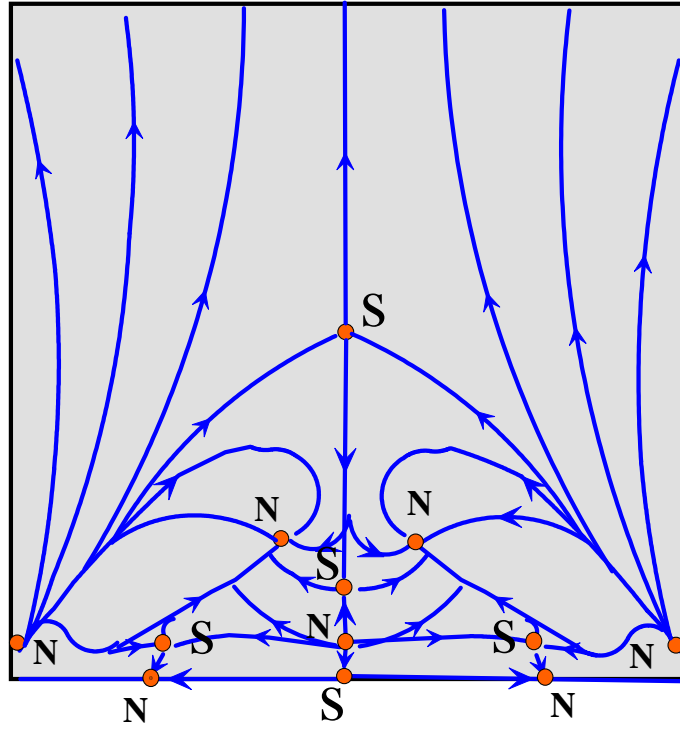


Figure 6.63 Definition of topology of the surface streamlines pattern (time-mean averaged), Case S1 $\alpha=5^\circ$, Mach = 0.42.

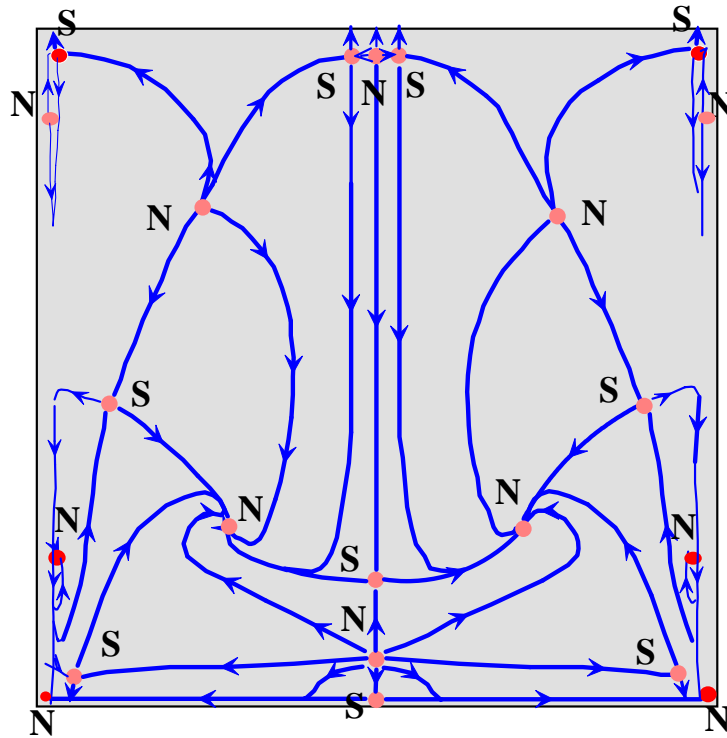


Figure 6.64 Definitions of topology of the surface streamlines pattern (time-mean averaged), Case S2 $\alpha=15^\circ$, Mach = 0.42.

iii. Force-Moment Comparisons

In Figure 6.65 through Figure 6.70, Normal Force and Pitching Moment comparisons with the experiment [39] are illustrated. Normal Force and Pitching Moment values are obtained by the integration of the surface pressures from the top and the bottom surfaces for each case. Since the results have the oscillatory behavior, the variables were again averaged over the corresponding cycle to each case. Hence, each figure shows the averaged, the maximum and the minimum values of the Normal Force and the Pitching Moment components over a period of cycle at the particular angle of attack. It is seen that the differences between computational and experimental values are the result of differences between pressure peak suction levels.

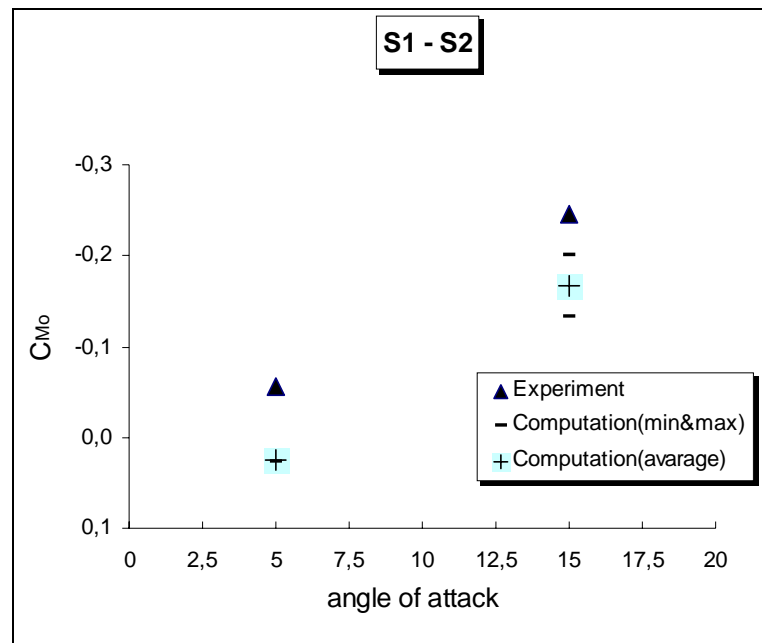


Figure 6.65 Comparison of computational and experimental [39] pitching-moment coefficients, Mach = 0.42, Re = 2.0×10^5 . Computational data from Case's: S1 and S2.

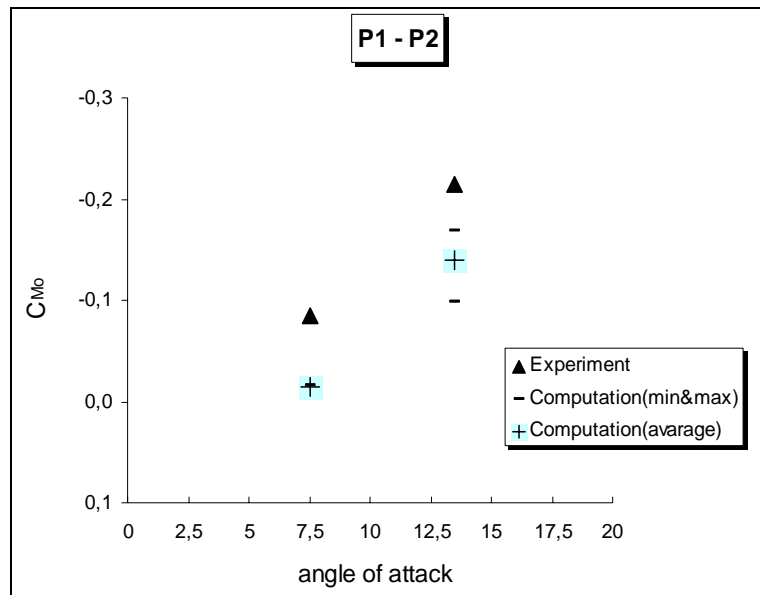


Figure 6.66 Comparison of computational and experimental [39] pitching-moment coefficients, Mach = 0.54-0.55, Re = $2.0 \cdot 10^5$. Computational data from Case's: P1 and P2.

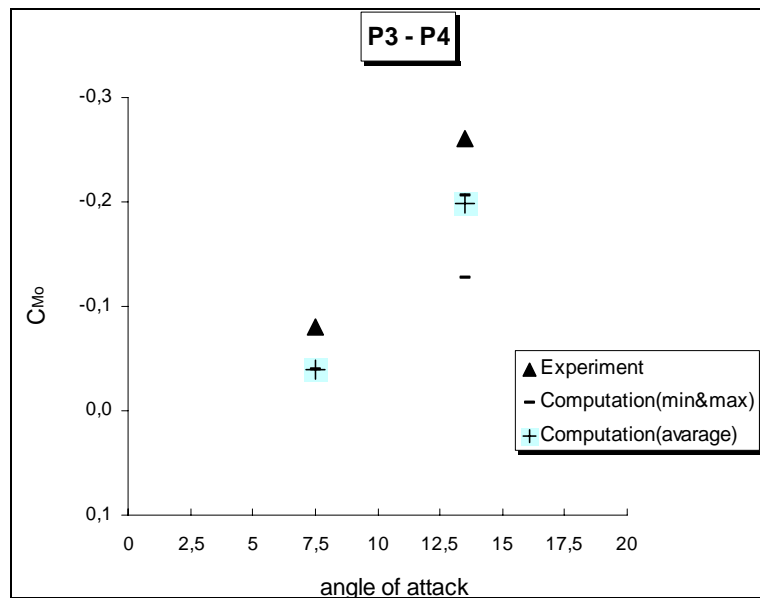


Figure 6.67 Comparison of computational and experimental [39] pitching-moment coefficients, Mach = 0.85-0.87, Re = $2.0 \cdot 10^5$. Computational data from Case's: P3 and P4.

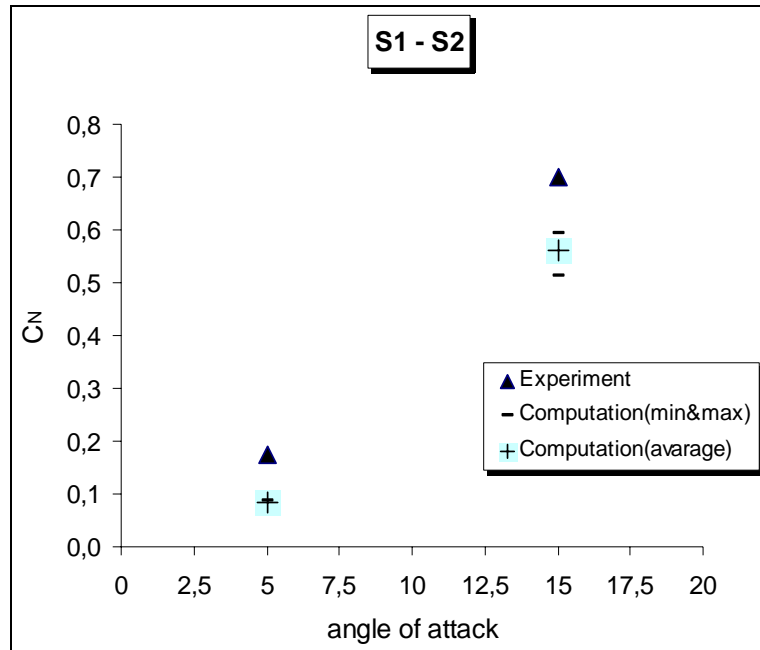


Figure 6.68 Comparison of computational and experimental [39] normal force coefficients, Mach = 0.42, Re = $2.0 \cdot 10^5$. Computational data from Case's: S1 and S2.

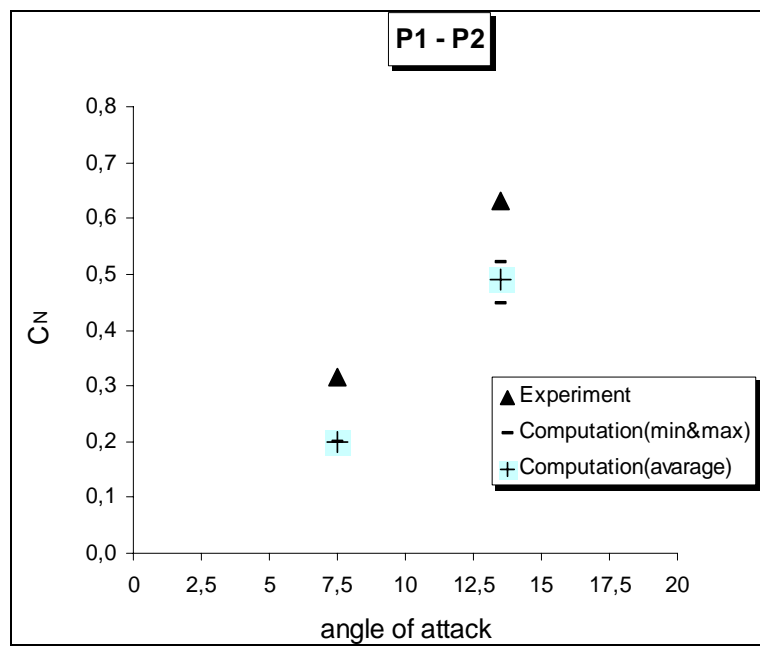


Figure 6.69 Comparison of computational and experimental [39] normal force coefficients, Mach = 0.54-0.55, Re = $2.0 \cdot 10^5$. Computational data from Case's: P1 and P2.

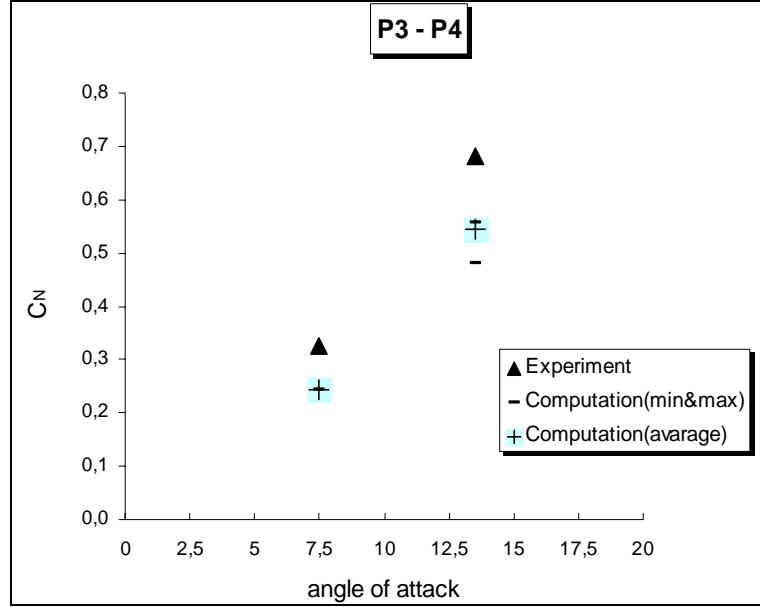


Figure 6.70 Comparison of computational and experimental [39] normal force coefficients, Mach = 0.85-0.87, Re = 2.0*10⁵. Computational data from Case's: P3 and P4

6.2.7.3. Computational Flow Field Visualizations

In this section, three-dimensional structure of the flow was investigated in order to get a deep understanding about the physics of the flow. It was observed that the size of the bubble and shedding vortex increased by increasing of the angle of attack and the Mach number. All Cases has a typical oscillation which consists of two distinct phases as stated in reference [23]; (i) gradual growth of large-scale structures in the separated shear layer, accompanied by a progressive growth of the separation bubble, (ii) shedding of a large-scale structure followed by a "collapse" of the bubble and abrupt shortening of the reattachment length. Flapping motion of the separated shear layer within the periodic vortex shedding from the separation bubble can be clearly seen. The frequency of the flapping motion was found to be the nearly same with

the vortex shedding frequency as mentioned in Kiya M. et al [6]. In Figure 6.71, the transient feature of the flow through timeline of S2 Case is presented in terms of velocity field at the symmetry plane. Time-resolved simulations obtained by velocity field at the symmetry plane for each case can be viewed in the Simulation CD Package.

The vortical structure of the flow field around the plate was illustrated in the Figure 6.72. This figure was extracted from just end of the timeline of Case S2 in order to show the flow structure clearly. The predominant structures over the separation bubble are clearly identified as hairpin (horseshoe) vortices in the reattachment region [23]. The legs of the horseshoe vortices are inclined with respect to the streamwise direction. A typical vortex grows in every direction as it is advected downstream of the reattachment region. Due to the interaction between the vortical motion of the large-scale structure and the wall, it also tends to lift away from the wall. This in turn, brings the top end of the horseshoe vortex into contact with the outer (higher velocity) region, resulting in further stretching and inclination of the vortex along the flow direction. Eventually, the central portion breaks down, and only the two inclined legs remain. In the case of separation bubble formation, there exist both primary and secondary separation bubbles in that picture. It verifies the skin-friction topology on the previous chapter that depicts the secondary separation bubble formation characterized by the saddle point near the leading edge. Reversed flow sourced by separation vortex occurs at mid-part and aft part of the side edge of the flat plate.

In that figure, primary vortex actually represents the spanwise vortices, which are produced by rolling up of the shear layer to form rectilinear vortex tubes whose axis is aligned with the side edge of the flat plate. Secondary vortices are also formed under the primary vortex as seen also on Figure 6.73 which is colored by the total pressure contours. It shows the transitional streamline plot of the Case S2; $\alpha=15^\circ$, Mach = 0.42

at the spanwise section of the plate, $x/c=0.5$. For the same Case, a similar picture that shows the primary and secondary bubble formation at the symmetry plane, $y/c=0.0$ is also demonstrated in Figure 6.74. Notice that, secondary bubble is shown in zoomed view in that figure. Time-resolved simulations that shows three dimensional flow structures for S1 and S2 Cases were also put in the Simulation CD Package.

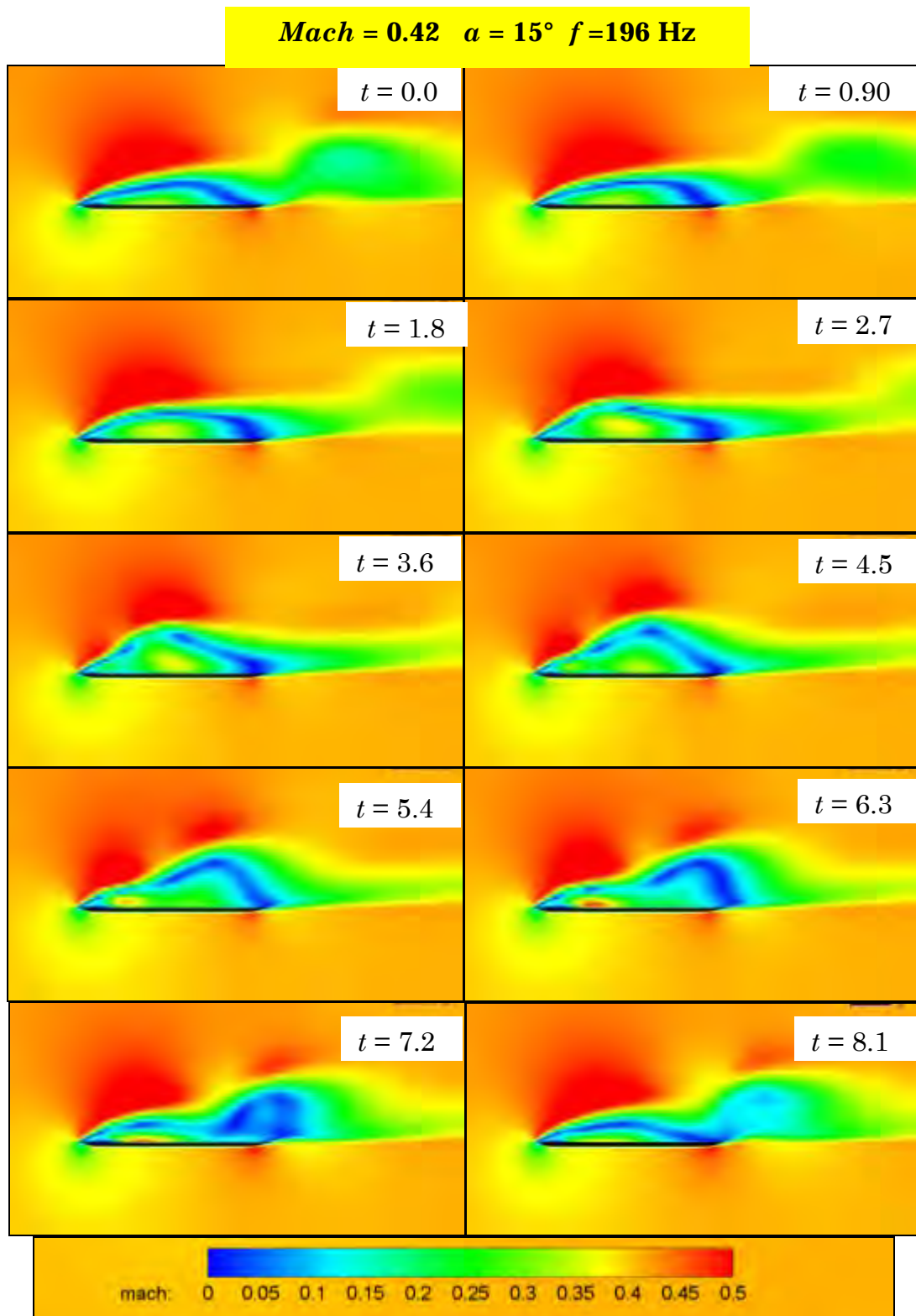


Figure 6.71 Flow timeline of Case S2 $\alpha=15^\circ$, $Mach = 0.42$

Mach=0.42 $\alpha=15^\circ$

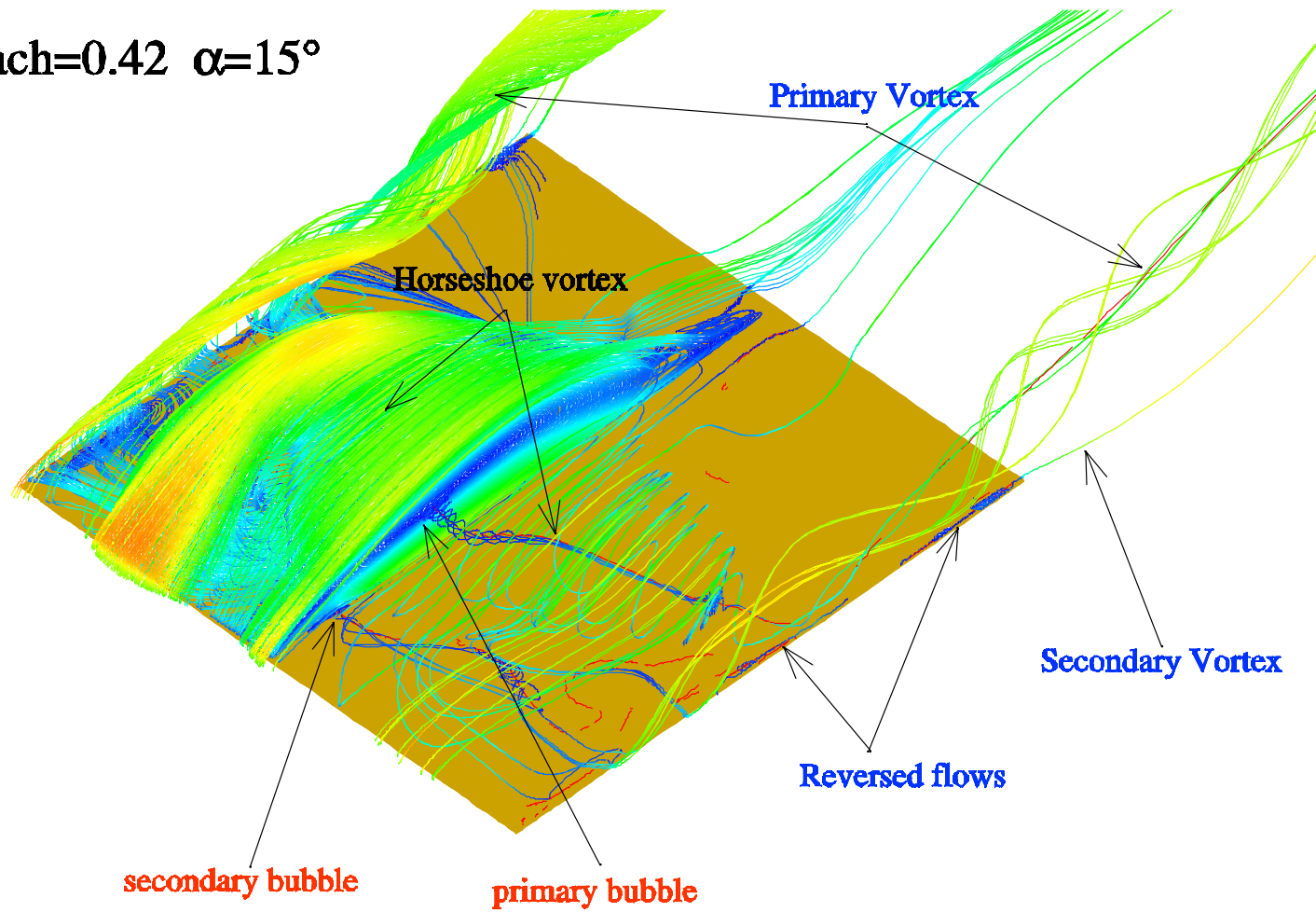


Figure 6.72 Three-dimensional flow structure of Case S2; $\alpha=15^\circ$, Mach = 0.42.

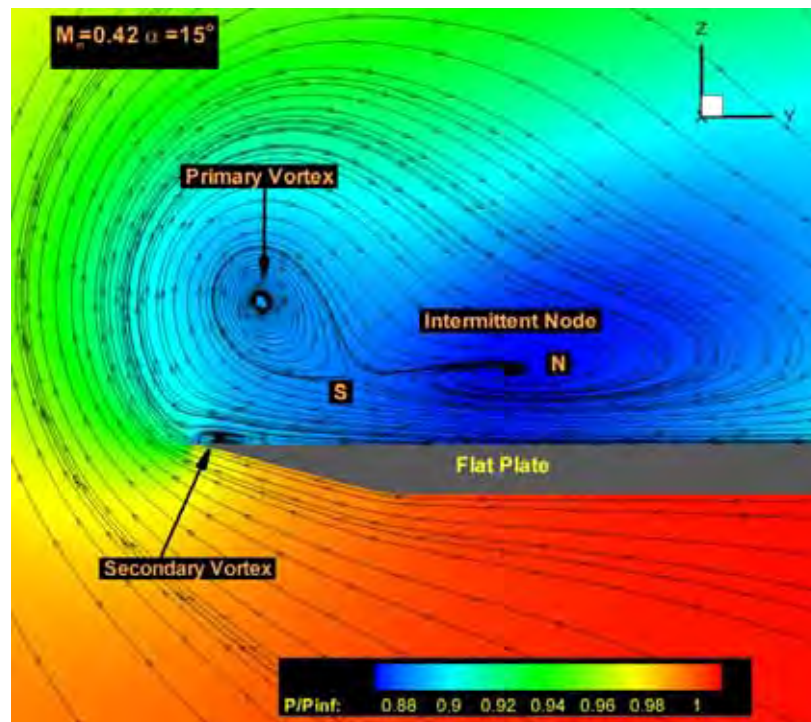


Figure 6.73 Primary and secondary vortices at the span wise plane, $x/c=0.5$.

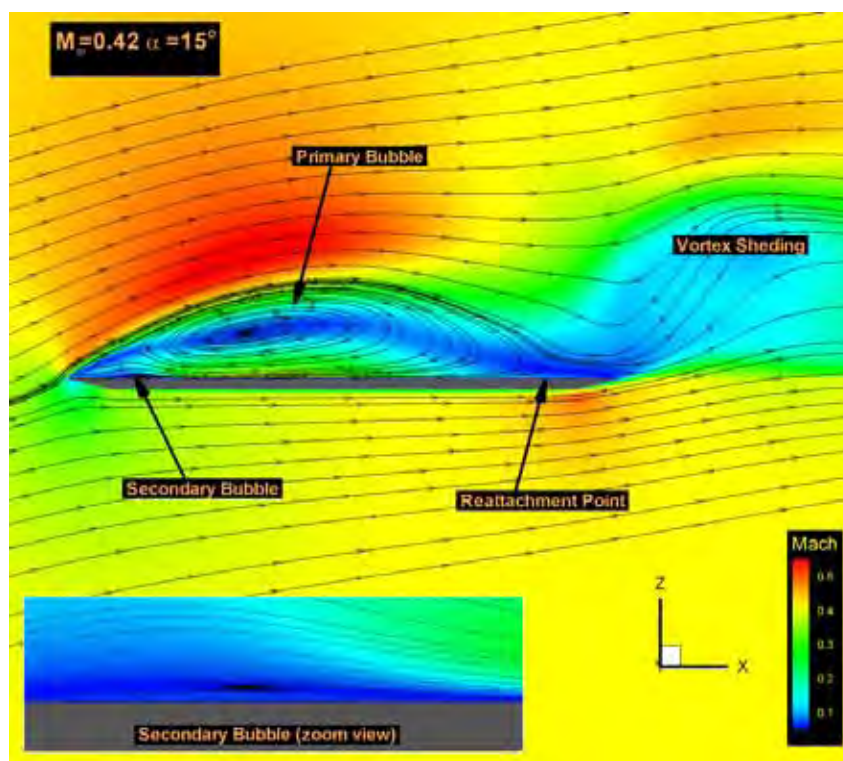


Figure 6.74 Primary and secondary bubbles at the symmetry plane, $y/c=0.0$

CHAPTER 7

CONCLUSION

Parallel Navier Stokes solutions of an aspect ratio 1.0 rectangular flat plate have been performed at different Mach numbers and angles of attack to test the validity of the Navier-Stokes code on the prediction of separated flows, in particular, the ones around the low aspect ratio wings. The flow separates at the leading edge and forms the separation bubble. It is dominated by the spanwise vortices and the rolling-up vortices within the separation bubble. Reynolds number was of the order of 2.0×10^5 - 3.0×10^5 . Two different grid configurations were adapted namely, the coarse and the fine grids in order to speed up the convergence of the solutions. For the fine grid part of the solution, two grid blocks with total of 700,000 points were used. The initial grid spacing from the surface in the normal direction was $\Delta z/c = 0.0001$.

There was a strong interference between the separation bubble and the side edge vortices making the flowfield quite complicated. Moreover, it was detected that the flow was unsteady and it has oscillating structure. However, the Baldwin-Lomax turbulence model modified around the vortical and the wake regions showed acceptable results. The prediction of the surface streamlines was found to be accurate to capture the flowfield structure in terms of size and formation of the primary and the secondary separation bubbles. The spanwise vortices at the side edges of the flat plate were in good

agreement with the experiment, showing both the primary and the secondary vortices.

It was found that the frequency of the flow, sourced by the separation bubble, increased with decreasing angle of attack and, its variation was more rapid for higher Mach numbers. It was also verified that with the increasing angle of attack, the size and the intensity of the separation bubble increased and the flow complexity increased showing more singular points; saddles and nodes on the surface. In addition, the periodic vortex shedding and the intermittent nature of the flow field were captured in three-dimensional time-resolved simulations.

The averaged top surface pressure predictions were in good agreement except the leading edge region of the wing. This may be improved by using a more sensitive turbulence model such as Spalart-Allmaras turbulence model, and by increasing the grid quality in future.

REFERENCES

- [1] Russell M. Cummings, James R. Forsytheb, Scott A. Mortonb, Kyle D. Squiresc, “Computational Challenges in High Angle of Attack Flow Prediction”, *Progress in Aerospace Sciences*, 39;369-384, 2003.
- [2] Keener ER, Chapman GT., “Similarity in Vortex Asymmetries over Slender Bodies and Wings”, *AIAA*, 15;370–2, 1977.
- [3] Rom J., “High Angle of Attack Aerodynamics”, New York, Springer, 1992.
- [4] Ericsson LE, Reding JP., “Asymmetric Vortex Shedding from Bodies of Revolution”, *Tactical Missile Aerodynamics*, New York, American Institute of Aeronautics and Astronautics, 1986.
- [5] Bertin JJ., “Aerodynamics for Engineers”, Upper Saddle River, NJ: Prentice-Hall, 2002.
- [6] Kiya M., Mochizuki O. and Ishikawa H., “Challenging Issues in Separated and Complex Turbulent Flows”, *Proceedings of the 10th International Conference on Laser Techniques*, 1-13, 2000.
- [7] Reece E. Neel, “Advances in Computational Fluid Dynamics: Turbulent Separated Flows and Transonic Potential Flows”, PhD Thesis, Virginia Polytechnic Institute and State University.
- [8] Alving, A. E., Fernholz, H. H., “Turbulence Measurements around a Mild Separation Bubble and Downstream of Reattachment”, *J. Fluid Mech.* 322, 297– 328, 1996.

- [9] Kazuhisa Chiba, Shigeru Obayashi, “CFD Visualization of Second Primary Vortex Structure on a 65-Degree Delta Wing”, 42nd AIAA Aerospace Sciences Meeting and Exhibit January 5–8, Reno, NV, AIAA 2004–1231, 2004.
- [10] Cherry NJ, Hillier R, “Unsteady Measurements in a Separated and Reattaching Flow”, *J Fluid Mech* 144:13–46, 1984.
- [11] Kiya M., Sasaki K., “Structure of a Turbulent Separation Bubble”, *J. Fluid Mech* 137:83–113, 1983.
- [12] Kiya M., Sasaki K., “Structure of Large-Scale Vortices and Unsteady Reverse Flow in the Reattaching Zone of a Turbulent Separation Bubble”, *J. Fluid Mech* 154:463–491, 1985.
- [13] Chun S., Sung H.J., “Influence of Unsteady Wake on a Turbulent Separation Bubble”, *Exp. Fluids* 32:269–279, 2002.
- [14] Hwang K.S., Sung H.J., Hyun J.M., “An Experimental Study of Large-scale Vortices over a Blunt-faced Flat Plate in Pulsating Flow”, *Exp. Fluids* 30: 202–213, 2001.
- [15] S. Chun, H.J. Sung, “Large-Scale Vortical Structure of Turbulent Separation Bubble Affected by Unsteady Wake”, *Experiments in Fluids* 34, 572–584, 2003.
- [16] Carl Haggmark, “Investigations of Disturbances Developing in a Laminar Separation Bubble Flow”, Technical Reports from Royal Institute of Technology Department of Mechanics S-100 44 Stockholm, Sweden, March 2000.
- [17] Kiya M., Ishikawa H., “Coherent Structures and Large Low-Frequency Irregularity in Free Turbulent Shear Flows Educated by Wavelet Transform and Proper Orthogonal Decomposition”,

Proceedings of 2nd China-Japan Workshop on Turbulent Flows (Ed. Qing-Ding Wei), 8-22, State Key Laboratory for Turbulence Research, Peking University, Peking, 1997.

- [18] Hourigan K., Thompson M. C. and Tan B. T., “Self-Sustained Oscillations in Flows around Long Blunt Plates”, *Journal of Fluids and Structures*, 15;387-398, 2001.
- [19] Sigurdson L.W., “The Structure and Control of Turbulent Reattaching Flow”, *Journal of Fluid Mechanics*, 248;267-296, 1995.
- [20] Nakamura Y., Nakashima M., “Vortex Excitation of Prisms with Elongated Rectangular H and Cross Sections”, *Journal of Fluid Mechanics*, 163;149-169, 1986.
- [21] Djilali N., Gartshore I.S., “Turbulent Flow around a Bluff Rectangular Plate”, Part I: Experimental investigation, *ASME J. Fluids Eng.*, 113;51-59. 1991
- [22] Saathoff P.J., Melbourne W.H., “Effects of Free Stream Turbulence on Surface Pressure Fluctuations in a Separation Bubble”, *J. Fluid Mech.*, 337;1-24, 1997.
- [23] Suksangpanomrung N., Djilali and Moinat P., “Large-Eddy Simulation of Separated Flow over a Bluff Rectangular Plate”, *France International Journal of Heat and Fluid Flow*, 21;655-63, 2000.
- [24] Yates L. A., Chapman G. T., “Streamlines, Vorticity Lines and Vortices around Three Dimensional Bodies”, *AIAA Journal*, 30(7);1819-1826, July 1992.
- [25] Simpson R. L., “Aspects of Turbulent Boundary-Layer Separation”, *Progress in Aerospace Sciences*, 32;457-521, 1996.

- [26] Tobak M., Peake D.J, "Topology of Three-Dimensional Separated Flows ", Annual Review of Fluid Mechanics, Vol. 14, pp. 61-85, 1982
- [27] Lighthill, M.J., "Attachment and Separation in Three-Dimensional Flow," Laminar Boundary Layers, Vol. 26, pp. 72-82, 1963.
- [28] Wickens R.H., "The Vortex Wake and Aerodynamic Load Distribution of Slender Rectangular Plates(The Effects of a 20° Bend at Mid-Chord)", National Research Council of Canada Aero Report LR-458, July 1966.
- [29] Fink M.P., Lastinger J.L., "Aerodynamic Characteristics of Low-Aspect Ratio Wings in Close Proximity to the Ground", NACA TN D-926, 1961.
- [30] Peake D.J., Tobak M., "Three Dimensional Flows about Simple Components at Angle of Attack", AGARD LS-121, 1982.
- [31] AGARD LS-98, Missile Aerodynamics, 1979.
- [32] AGARD LS-121, High Angle of Attack Aerodynamics, 1982.
- [33] AGARD CP-494, Vortex Flow Aerodynamics, 1991.
- [34] AGARD CP-497, Maneuvering Aerodynamics, 1991.
- [35] AGARD R-776, Special Coarse on Aircraft Dynamics at High Angles of Attack: Experiments and Modelling, 1992.
- [36] Stahl W. H., "Aerodynamics of Low Aspect Ratio Wings", AGARD LS-98, Missile Aerodynamics, 1979.
- [37] Winter H., "Strömungsvorgänge an Platten und profilierten Körpern bei kleinen Spannweiten", Forsch. Ing. -Wes., Vol. 6, , pp. 40-50, 1937.

- [38] Van Westerhoven P., Wedemeyer E., Wendt J. F., “Low Aspect Ratio Rectangular Wings at High Incidences”, Paper presented at the AGARD Symposium on Missile Aerodynamics, Trondheim, Norway, September 20-22, 1982.
- [39] Kavsaoğlu M. Ş, “Flow Around Low Aspect Ratio Rectangular Flat Plates Including Compressibility”, von Karman Institute For Fluid Dynamics, VKI-PR 1982-15, June 1982.
- [40] Reece E. Neel, “Advances in Computational Fluid Dynamics: Turbulent Separated Flows and Transonic Potential Flows”, PhD Thesis, Virginia Polytechnic Institute And State University.
- [41] Simpson R. L., “Two-Dimensional Turbulent Separated Flow”, AGARDograph 287, vol. 1, 1985.
- [42] Simpson R. L., “Turbulent Boundary-Layer Separation”, Annual Review of Fluid Mechanics, vol. 21, pp. 205-234, 1989.
- [43] Rockwell, D, “Active Control of Globally-Unstable Separated Flows”, In proceedings of the ASME Symposium on Unsteady Flows, 3-9 June, Toronto, Canada 1990.
- [44] Hijikata K., Suzuki Y. and Iwana K., “Flow Visualization by Velocity–Pressure Cross Correlation”, J. Fluid Eng., 118;486–493, 1996.
- [45] Johansson A.V., Her J.Y. and Haritonidis J.H., “On the Generation of High-Amplitude Wall-Pressure Peaks in Turbulent Separation Bubble”, J. Fluid Mech., 175:119–142, 1987.
- [46] Chun S., Sung H.J., “Influence of Unsteady Wake on a Turbulent Separation Bubble”, Exp. Fluids 32:269–279, 2002.

- [47] Ekaterinaris J. A., Schiff L. B., “Numerical Prediction of Vortical Flow over Slender Delta Wings”, *Journal of Aircraft*, Vol. 30, No. 6, , pp. 935–942, 1993.
- [48] Murayama M., Nakahashi K., Obayashi S., and Kato T., “Numerical Simulation of Vortical Flows Using Vorticity Confinement Coupled with Unstructured Adaptive Grid Refinement”, *Computational Fluid Dynamics Journal*, Vol. 10, No. 1, pp. 28–36, 2001.
- [49] Luckring J.M., “Reynolds Number and Leading-Edge Bluntness Effects on a 65° Delta Wing”, *AIAA Paper 2002-0419*, 2002.
- [50] Chu J., Luckring J.M., “Experimental Surface Pressure Data Obtained on 65° Delta Wing across Reynolds Number and Mach Number Ranges”, *NASA TM-4645*, Feb 1996.
- [51] Djilali N., Gartshore I.S., “Turbulent Flow around a Bluff Rectangular Plate”, Part II: Numerical Predictions, *ASME J. Fluids Eng.*, 113;60-67, 1991.
- [52] Nakamura Y., Ohya Y. and Tsuruta H., “Experiments on Vortex Shedding at Plates with Square Leading and Trailing Edges”, *Journal of Fluid Mechanics*, 222;437-447, 1991.
- [53] Naudascher E., Wang Y., “Flow-Induced Vibration of Prismatic Bodies and Grids of Prisms”, *Journal of Fluids and Structures*, 7 ;341-373, 1993.
- [54] Hourigan K., Mills R., Thompson M.C., Sheridan J., Dilin P. and Welsh M.C., “Base Pressure Coefficients for Flows around Rectangular Plates”, *Journal of Wind Engineering and Industrial Aerodynamics*, 49;311-318, 1993.

- [55] Mills R., Sheridan J., Hourigan K. and Welsh M.C., "The Mechanism Controlling Vortex Shedding from Rectangular Bluff Bodies", In Proceedings of the 12th Australasian Fluid Mechanics Conference (Ed. R. W. Bilger), 227-230, 10-15 December, Sydney, Australia 1995.
- [56] Mills R.H., "Vortex Interaction in Flows over Blunt Bodies", Ph.D. Dissertation, Department of Mechanical Engineering, Monash University, Melbourne, Australia 1998.
- [57] Tan B.T., Thompson M.C. and Hourigan K., "Flow around Long Rectangular Plates under Cross-Flow Perturbations", International Journal Of Fluid, Article 1, 1998.
- [58] Sadatoshi Taneda, "Instability Waves in the Shear Layer over a Separation Bubble", Fluid Dynamics Research, 27;335-351, 2000.
- [59] Alving A.E., Fernholz H.H., "Turbulence Measurements around a Mild Separation Bubble and Downstream of Reattachment", J. Fluid Mech, 322;297-328, 1996.
- [60] Thomas James L., Krist Sherrie T. and Anderson W.Kyle, "Navier-Stokes Computations of Vortical Flows over Low_Aspect-Ratio Wings", AIAA Journal, VOL.28, No.2, February 1990.
- [61] Kevin Waclawicz, "The Relationship between Crossflow Velocity and Off-the-Surface Streamtrace Topology for a Moderately Swept Wing at Transonic Mach Numbers", MSc Thesis, Virginia Polytechnic Institute and State University.
- [62] Delery Jean M., "Robert Legendre and Henri Werle, "Toward the Elucidation of Three- Dimensional Separation", Annual Review of Fluid Mechanics, Vol. 33;129-154, 2001.

- [63] Legendre R., "Separation de L'écoulement Laminaire Tridimensionnel", La Recherche Aeronautique, 54;3-8, 1956.
- [64] Chapman Gary T., "Topological Classification of Flow Separation", AIAA Paper 86-0485, 1986.
- [65] Wang K.C., "Separation of Three-Dimensional Flow", Reviews in Viscous Flow, 341-414, 22 June 1976
- [66] Cipolla K.M., Rockwell D., "Instantaneous Crossflow Topology on a Delta Wing in Presence of Vortex Breakdown", Journal of Aircraft, Vol.35, 218-222, March 1998.
- [67] Hunt J.C., Abell C.J, Peterka J.A. and Woo H., "Kinematical Studies of the Flows Around Free or Surface-Mounted Obstacles; Applying Topology to Flow Visualization", Journal of Fluid Mechanics, 179-200, 1986
- [68] Chan W.M., Steger J.L., "Enhancements of a Three Dimensional Hyperbolic Grid Generation Scheme", Applied Mathematics and Computation, Vol. 51, No.1, , 181-205, 431-438, 1992.
- [69] Steger J.L., Rizk Y.M., "Generation of Three-Dimensional Body-Fitted Coordinates using Hyperbolic Partial Differential Equations", NASA TM 86753, NASA-Ames Research Center, Mottet Field, California, 1985.
- [70] Tai C.H., Chiang D.C and Su Y. P., "Three Dimensional Hyperbolic Grid Generation with Inherent Dissipation and Laplacian Smoothing", AIAA Journal, Vol. 34, No. 9, Sept. 1996.
- [71] Zwan R.J., "Lann Wing, Pitching Oscillation", AGARD Report No: 702, Compendium of Unsteady Aerodynamics , Addendum No:1, 1985.

- [72] Baldwin B.S., Lomax H., “Thin Layer Approximation and Algebraic Model for Separated Turbulent Flows”, AIAA 16th Aerospace Meeting, Huntsville, Alabama, January, 1978.
- [73] Degani D., Schiff L., “Computation of Turbulent Supersonic Flows Bodies having Crossflow Separation”, Journal of Computational Physics, Vol 66, 173-196, 1986.
- [74] User’s Guide, NPARC Flow Simulator Version 3.0.
- [75] Karlsruhe Parallel Program for Aerodynamics (KAPPA) Dokumentation Magagnato, The Institute for Fluid Mechanics, University of Karlsruhe, 1996.
- [76] Durmuş G., “Three Dimensional Hyperbolic Grid Generation”, MS Thesis, Middle East Technical University, Department of Aeronautical Engineering, September 1998.
- [77] Schetz J. A., “Boundary Layer Analysis”, Prentice Hall, 1993.
- [78] Roberts G.O., “Computational Meshes for Boundary Layer Problems”, Proceedings of the Second International Conference on Numerical Methods in Fluid Dynamics, Lecture Notes in Physics, Vol. 8, Springer-Verlag, New York, 171-177, 1971.
- [79] Coles D.E., Hirst E.A. eds., “Computation of Turbulent Boundary Layers -1968”, Proceedings of the AFOSR-IFP-Stanford Conference, Vol. II, Stanford University, 1968.
- [80] Daily J.W., Harleman D.R.F., “Fluid Dynamics”, Addison-Wesley, Reading, Massachusetts 1966.
- [81] White F.M., “Viscous Fluid Flow”, McGraw-Hill Book Company, New York 1974.

- [82] Şen T. S., “Development of a Three Dimensional Multiblock Parallel Navier Stokes Solver”, PhD Thesis, Middle East Technical University, Department of Aeronautical Engineering, November 2001.
- [83] Beam R.W., Warming R.F., “An Implicit Finite Difference Algorithm for Hypersonic Systems in Conservation Form”, Journal of Computational Physics, Vol. 23, 87-110, 1976
- [84] Fujii K., “Practical Applications of New LU-ADI Scheme for the Three Dimensional Navier-Stokes Computation of Transonic Viscous Flows”, AIAA 24th Aerospace Sciences Meeting, Reno, Nevada, January 1986.

CURRICULUM VITAE

PERSONAL INFORMATION

Surname, Name : Durmuş, Gökhan
Nationality : Turkish (TC)
Date of Birth : 13 October 1972
Place of Birth : Ankara
Marital Status : Single
Phone : +90 312 344 48 83
Email : gdurmus@anadolu.edu.tr

EDUCATION

Degree	Institution	Year of Graduation
PhD	METU Aerospace Engineering	2004
MS	METU Aerospace Engineering	1998
BS	METU Aerospace Engineering	1995

WORK EXPERIENCE

Year	Place	Enrollment
1996- Present	Anadolu University Civil Aviation School, Eskişehir	Research Assistant

FOREIGN LANGUAGES

Advanced English, Beginner German

PUBLICATIONS

1. Durmuş G., Kavsaoğlu M. Ş., “Control of Hyperbolic Grids”, Aiaa `98 – Proceedings of the 2nd Ankara International Aerospace Conference, 9-11 September 1998, Middle East Technical University, Ankara, Turkey, pp. 120-124.
2. Durmuş G., Kavsaoğlu M. Ş., “Marching Distance Functions for Smooth Control of Hyperbolic Grids”, Aiaa Journal, Vol 38, No: 10, October 2000.

3. Durmuş G., Kavsaoglu M. Ş., “Multi Block Navier Stokes Solutions of Low Aspect Ratio Rectangular Flat Wings in Compressible Flow”, In Proceedings of The 23rd International Congress of Aeronautical Sciences, Toronto, Canada, 8-13 September, 2002.
4. Durmuş G., Kavsaoglu M. Ş., “Düz Levha Üzerindeki Laminer Sınır Tabaka Akımının Navier Stokes Analizinde Çözüm Ağı Etkileri” Kayseri 5. Havacılık Sempozyumu, Erciyes University, Civil Aviation School, 13-14 May 2004, Kayseri, Turkey.
5. Durmuş G., Kavsaoglu M. Ş., Kaynak Ü., “Parallel Solution of Low Aspect Ratio Rectangular Flat Wings in Compressible Flow”, 43rd AIAA Aerospace Sciences Meeting and Exhibit, 10 - 13 Jan 2005, Reno, Nevada.(to be published)